University of Alberta

Monte Carlo modeling of Helical Tomotherapy and evaluation of its treatment planning system

by

Ying-Li Zhao

A thesis submitted to the Faculty of Graduate Studies and Research
in partial fulfillment of the requirements for the degree of

Master of Science
in
Medical Physics

Department of Physics

Edmonton, Alberta
Fall, 2008

Library and
Archives Canada

Published Heritage
Branch

395 Wellington Street
Ottawa ON K1A 0N4
Canada

Bibliothèque et
Archives Canada

Direction du
Patrimoine de l'édition

395, rue Wellington
Ottawa ON K1A 0N4
Canada

Your file Votre référence
ISBN: 978-0-494-47456-3
Our file Notre référence
ISBN: 978-0-494-47456-3

Abstract:

Helical tomotherapy is an advanced Intensity Modulated Radiation Therapy (IMRT) technique for cancer treatment. Dose calculation in the treatment planning system (TPS) plays an important role in this multi field IMRT to achieve the maximum tumor control and the minimum normal tissue complication. The Monte Carlo (MC) method, which is considered the most accurate dose calculation algorithm in radiotherapy, was used to model the helical tomotherapy system and evaluate its dose calculation accuracy. The MC calculations were verified against experiment measurements. The helical tomotherapy TPS was evaluated for homogenous and heterogeneous phantom irradiations as well as clinical patient datasets. The TPS calculation in the homogeneous water equivalent Cheese Phantom gives results that are comparable in accuracy with the MC calculation. The TPS failed a 5%/3mm criterion in some of the low dose regions and high dose gradient regions in a heterogeneous CIRS phantom and patient datasets.

Acknowledgements

I am grateful to my supervisors, Dr. Marc MacKenzie and Dr. Gino Fallone, for the opportunity to work on this unique project. I thank Dr. MacKenzie for his guidance, patience and kindness throughout this work. I thank Dr. Fallone for his strict guidance to make this project fruitful.

I am grateful to many researchers in the Department of Medical Physics who have provided me help regarding my research projects. In particular, I would like to thank Dr. Charlie Kirkby for sharing his expertise on Monte Carlo simulation, Dr. Steven Thomas for his advice in the tomotherapy studies, Dr. Ron Sloboda for his rigorous scholarship. I should also thank Mr. Praful Shrestha for supporting the MC clusters and Mr. Len Johnson for maintaining the tomotherapy machines.

I also want to acknowledge all the members of the medical physics for their useful suggestions and stimulating discussions during the course of my research. Special thank to Dr. Tara Monajemi, Dr. Brad Warkentin, Dr, Hans Jans, Dr. Alasdair Syme, Lesley Baldwin and Amr Heikal for their support and friendship.

I wish to express my appreciation to my parents, Zhao, Junxiang and Liu, Yuzhi. Without their unselfish love, endless support and belief in me, this thesis would have been impossible. To my brother, Zhao, Yingming, thank you for being my great brother and friend.

And for Wen, Qing, thank you for making everyday so special to me. Thank you so much for your help, love and support.

Table of Contents

List of Tables

List of Figures

List of Abbreviations

3D-CRT	Three Dimensional Conformal Radiotherapy
CPE	Charge Particle Equilibrium
CT	Computed Tomography
CTV	Clinical Target Volume
DQA	Delivery Quality Assurance
DTA	Distance to Agreement
FOV	Field of View
GTV	Gross Tumor Volume
HT	Helical tomotherapy
ICRU	International Commission on Radiation Units and Measurements
IGAR	Image Guided Adaptive Radiotherapy
IMRT	Intensity Modulated Radiation Therapy
Linac	Linear accelerator
LASG	Locally Adaptive Savitzky–Golay curve-fitting
MC	Monte Carlo
MLC	Multi Leaf Collimator
NTCP	Normal Tissue Complication Probability
OAR	Organ at Risk
PTV	Planning Tumor Volume
TCP	Tumor Control Probability
TPS	Treatment Planning System

Chapter 1 : Introduction

Helical tomotherapy represents a highly integrated and advanced Intensity Modulated Radiotherapy (IMRT) delivery technique, as well performing Image Guided Adaptive Radiotherapy (IGAR) (Mackie et al., 1993; 2003). The idea of helical tomotherapy is to use an intensity modulated, narrow photon fan beam that moves in a helical pattern to deliver a conformal radiation dose distribution to a planning target volume (PTV) while avoiding nearby organs at risk (OAR). Its unique design makes helical tomotherapy capable of delivering more complex modulated coplanar beam arrangements from more angles than typically found in conventional linac IMRT. Helical tomotherapy has clear advantages in homogeneity of the dose distribution within a PTV and the same or better normal tissue sparing compared to conventional three dimensional conformal radiotherapy (3D CRT) and linac IMRT (Han et al., 2007; Kron et al., 2004)

Like other IMRT systems, helical tomotherapy delivers 'sculpted' radiation fields to the PTV and this makes higher conformal dose to tumors in the complex environment of a patient's critical structures possible. IMRT, with its steep dose gradients, requires the treatment planning system (TPS) to give an accurate dose calculation to predict the dose delivery, which is necessary for an effective patient treatment. A criterion of $\pm 5\%$ percent difference to maximum dose (D_m) or 3mm distance-to-agreement (DTA) was suggested (Winkler et al., 2005). More stringent criteria with 2%/2mm were suggested by the ICRU 42 report (ICRU-42-report, 1987; ICRU-42, 1987).

Although helical tomotherapy TPS uses a relatively accurate kernel-based collapsed-cone convolution/superposition algorithm for dose calculation (McNutt et al., 1997) , as

with other non-Monte Carlo (MC) algorithms, charge particle equilibrium (CPE) is assumed in the dose calculation. We can reasonably expect the TPS will have difficulties in predicting the dose in certain situations, such as in regions with significant tissue inhomogeneities where this assumption is not satisfied. These situations are encountered in the build-up regions behind air cavities and low density tissues such as those found in head-and-neck and lung treatments (Davidson et al., 2007; Jones and Das, 2005; Vanderstraeten et al., 2006). The MC approach, which provides an accurate dose calculation method and does not require the assumption of CPE, can be used as a benchmark to validate the TPS predicted dose in such cases. In routine delivery quality assurance (DQA), the TPS predicted dose is verified against measurement in a solid water phantom called the 'Cheese Phantom' (Thomas et al., 2005) which, because of its homogeneous construction, does not necessarily validate the patient dose, but rather the ability of the system to deliver and calculate the plan dose in a simplified medium. Moreover, the verification is generally only performed at one point with an ion chamber and one plane with film measurement, rather than the whole irradiated volume as is done with the MC approach.

In general, a method for performing MC dose calculations in a helical tomotherapy patient geometry is desirable for several reasons: 1) it would provide, in addition to film and ion chamber dosimetry, further validation for the complex treatments delivered by the helical tomotherapy unit; 2) it would allow the validation of the performance of the helical tomotherapy treatment planning software on a 3D, point-by-point basis; and 3) it would allow for the simulation and investigation of the dosimetric consequences of new delivery techniques with helical tomotherapy before they are enabled (e.g. running start

with the jaws). The calculation of MC doses for the helical tomotherapy system is made far more complicated than for 3D CRT or even 'conventional' multi field IMRT by the potentially very large number of beam directions and leaf opening configurations for the complex modulated fields employed in the delivery; the number of 'beamlets' , which are the basic units of a beam, may be well into the tens of thousands. This thesis presents the development of a method for performing explicit MC simulation of helical tomotherapy deliveries. The project has developed significant innovations in the accurate simulation of complex modulated fields, without the need to resort to approximations for the tongue and groove effect or the need to render the net leaf openings into an approximate effective single field. This work has developed a reliable tool that can be used to investigate patient dosimetry in problematic situations where the accuracy of the conventional TPS may be questionable, as well as a means of TPS validation. It also provides a foundation for further work into MC-based treatment planning for a tomotherapy system, although several hurdles have yet to be overcome before such a system becomes a reality.

The result of our research is reported to the journal of Medical Physics in two separate papers. One is published (Zhao et al., 2008a) and the other is accepted for publication (Zhao et al., 2008b).

Bibliography:

Davidson, S. E., Ibbott, G. S., Prado, K. l. L., Dong, L., Liao, Z., and Followill, D. S. (2007): Accuracy of two heterogeneity dose calculation algorithms for IMRT in treatment plans designed using an anthropomorphic thorax phantom. *Med. Phys.* **34**, 1850-57.

Han, C., Chen, Y. J., Liu, A., Schultheiss, T. E., and Wong, J. Y. (2007): Dosimetric study and in-vivo dose verification for conformal avoidance treatment of anal adenocarcinoma using helical tomotherapy. *Med. Dosim.* **32**, 33-37.

ICRU-42 (1987): Use of Computers in External Beam Radiotherapy Procedures with High-Energy Photons and Electrons. *Journal of the ICRU.*

Jones, A. O., and Das, I. J. (2005): Comparison of inhomogeneity correction algorithms in small photon fields. *Med. Phys.* **32**, 766-76

Kron, T., Grigorov, G., Yu, E., Yartsev, S., Chen, J. Z., Wong, E., Rodrigues, G., Trenka, K., Coad, T., Bauman, G., and Van Dyk , J. (2004): Planning evaluation of radiotherapy for complex lung cancer cases using helical tomotherapy. *Phys. Med. Biol.* **49**, 3675-90.

Mackie, T. R., Holmes, T., Swerdloff, S., Reckwerdt, P., Deasy, J. O., J.Yang, Paliwal, B., and T. Kinsella (1993): Tomotherapy: a new concept for the delivery of dynamic conformal radiotherapy. *Med. Phys.* **20**, 1709-19.

Mackie, T. R., Kapatoes, J., Ruchala, K., Lu, W., Wu, C., Olivera, G., Forrest, L., Tome, W., Welsh, J., Jeraj, R., Harari, P., Reckwerdt, P., Paliwal, B., Ritter, M., Keller, H., Fowler, J., and Mehta, M. (2003): Image guidance for precise conformal radiotherapy. *Int. J. Radiation Oncology Biol. Phys.* **56**, 89–105.

McNutt, T. R., Mackie, T. R., and Paliwal, B. R. (1997): Analysis and convergence of the iterative convolution/superposition dose reconstruction technique for multiple treatment beams and tomotherapy. *Med. Phys.* **24**, 1465–76

Thomas, S. D., Mackenzie, M., Field, G. C., Syme, A. M., and Fallone, B. G. (2005): Patient specific treatment verifications for helical tomotherapy treatment plans. *Med. Phys.* **32**, 3793-3800.

Vanderstraeten, B., Reynaert, N., Paelinck, L., Madani, I., Wagter, C. D., Gersem, W. D., Neve, W. D., and Thierens, H. (2006): Accuracy of patient dose calculation for lung IMRT: A comparison of Monte Carlo, convolution/superposition, and pencil beam computations. *Med. Phys.* **33**, 3149–3158.

Winkler, P., Guss, B. Z. H., Kindl, P., and Stuecklschweiger, G. (2005): Performance analysis of a film dosimetric quality assurance procedure for IMRT with regard to the employment of quantitative evaluation methods. *Phys. Med. Biol.* **50**, 643-54

Zhao, Y. L., Mackenzie, M., Kirkby, C., and Fallone, B. G. (2008a): Monte Carlo calculation of helical tomotherapy dose delivery. *Med Phys* **35**, 3491-3500.

Zhao, Y. L., Mackenzie, M., Kirkby, C., and Fallone, B. G. (2008b): Monte Carlo evaluation of a treatment planning system for helical tomotherapy in an anthropomorphic heterogeneous phantom and for clinical treatment plans. *Med Phys* **submitted**.

Chapter 2 : Helical tomotherapy

2.1 Cancer and cancer treatments

Cancer is a term for a group of over 100 chronic diseases, which can affect any part of the body. A defining feature of cancer is the rapid proliferation of abnormal cells, which grow beyond their usual boundary and can invade adjoining parts of the body. (WHO, 2007)

Cancer is currently the most significant health care problem in the western world surpassing heart disease as the leading cause of potential years of life lost (WHO, 2007). In the United States, about 1,373,000 people are diagnosed with cancer each year (American Cancer Society, 2006). The main forms of cancer treatment are surgery for the bulk removal of tumor which is abnormal proliferation of tissues, drugs both to kill and to prevent proliferation of cancer cells (chemotherapy), harnessing of the body's own defense systems (immunotherapy) and the use of ionizing radiation to kill the cancer cells (radiotherapy) (Khan, 2003; WHO, 2007). Advances in technology and a better understanding of the effects on the body of radiation therapy have made it an important part of cancer treatment. About half of all cancer patients will receive radiotherapy used by itself or along with other therapies (Khan, 2003).

Radiotherapy uses beams of charged particles or beams of indirectly ionizing radiation (e.g. x-ray) to attack cancer cells. Modern research indicates the ionizing radiation interacting with the genetic material in cells could be the major cause of cell killing (Hall, 2006). Absorbed dose, defined as energy absorbed by a unit mass of matter, is a physical quantity measuring the radiation effect (Johns and Cunningham, 1983). Radiotherapy can locally affect the cells in and around the cancer. It can cure or shrink

early stage cancer, stop cancer from recurring in another area and treat symptoms for advanced cancer (Khan, 2003).

While killing the cancer cells, ionizing radiation can also affect cells of normal tissues. The damage to normal cells in radiotherapy is what causes undesired side effects. Radiation can affect the skin, the central nervous system, critical organs, blood cells and other parts of the human body involved in the irradiation fields. The killing of normal tissue cells in these organs causes early effects of radiation. They may be seen a few days or weeks after treatments have started and may continue for several weeks after treatments are completed. Another important side effect is the stochastic inducement of secondary cancer, which may arise from the damage of the genetic materials after exposure to radiation. Surviving cells from radiation have a high probability of mutation and some mutated cells have the potential to become cancerous. Secondary cancers could be developed within 5 to 9 years after radiation exposure in some patients (Hall and Giaccia, 2006).

Although the side effects are much less critical than the cancer and the risk of secondary cancers is generally low, especially when they are balanced against the mostly dramatic benefits gained with radiation treatments, they are still important factors to be considered in radiation therapy treatment planning. Modern radiotherapy technique developments are mainly focused on delivering accurate and precise dose distributions, which uniformly cover the tumor volume in order to maximize tumor control probability (TCP), while at the same time, minimizing the dose to normal tissues and thereby minimizing the normal tissue complication probability (NTCP).

2.2 Hi-Art II, helical tomotherapy system

Helical tomotherapy is a relatively new and presently expanding form of external beam radiation therapy. It combines both Intensity Modulated Radiation Therapy (IMRT) and Image Guided Adaptive Radiotherapy (IGAR) (Mackie et al., 1993; 2003) and thereby may provide significant improvements in the outcomes of radiation therapy.

2.2.1 Modern radiotherapy with IMRT and IGRT

The goal of delivering large doses to the tumor and sparing the surrounding normal tissues requires accurately calculated and optimized dose delivery plans and the precise control of the radiation delivery. To carry out these tasks, several challenges occur in practice. The first challenge is to accurately define the tumor volume. Current imaging modalities such as Computed Tomography (CT) and Magnetic Resonance Imaging (MRI) allow for the construction of 3D patient models down to millimeter range resolution. Some cancer can invade surrounding normal tissues and CT sometime doesn't provide enough information for the microscopic spread of the cancer. Hence, Gross Tumor Volume (GTV), Clinical Target Volume (CTV) and Planning Target Volume (PTV) are used in radiation therapy to define the region to be treated in radiation therapy (ICRU-50, 1993; ICRU-62, 1999). GTV is defined as gross tumor extent and its location is either palpable or visible/demonstrable by imaging techniques; CTV contains a demonstrable GTV and/or sub-clinical microscopic malignant disease (ICRU-50, 1993); PTV is a geometrical concept defined to select appropriate beam sizes and beam arrangements, taking into consideration the net effect of all the possible geometrical variations (ICRU-62, 1999). Magnetic Resonance Spectroscopic Imaging (MRSI), Positron Emission Tomography (PET) or other imaging modalities are used to provide chemical, biological,

functional or even metabolic information to help define these volumes. Another challenge is to reduce the positioning differences between the planned treatment and the real delivery. These differences can be caused by physical setup errors as well as organ motion and deformation during delivery or between treatment fractions. Yet another challenge is the accurate calculation of the 3D dose distribution within the patient. This task can be difficult in the presence of tissue heterogeneities, for example, and naturally becomes a more complex task as the complexity of the radiation therapy treatment increases. This will be explained in the later chapters and this is also the major focus of this thesis.

Patients are not static over the course of a radiotherapy treatment. An emerging trend in the advancement of radiotherapy is to consider the treatment process as dynamic. A patient's anatomy can change significantly over a period of several weeks (the typical duration of a radiotherapy treatment course). Further, during irradiation (which can take several minutes) the patient's organs can move. Consider for example those structures in the thorax affected by breathing. These factors add time as a fourth dimension in addition to the spatial dimensions that should be incorporated into advanced radiotherapy.

2.2.1.1 Intensity modulated radiation therapy (IMRT)

Bortfeld (2006) generally defined IMRT as "a radiation treatment technique with multiple beams in which at least some of the beams are intensity-modulated and intentionally deliver a non-uniform intensity to the target. The desired dose distribution in the target is achieved after superimposing such beams from different directions. The additional degrees of freedom are utilized to achieve a better target dose conformity and/or better sparing of critical structures." In Figure 2-1, the principle of IMRT is

illustrated. To achieve the spatial conformity of the radiation dose distribution in targets and conformal avoidance of that dose in normal tissues, non-uniform intensities (net energy fluences) are needed in the radiation beams (Brahme, 1988; 1982).

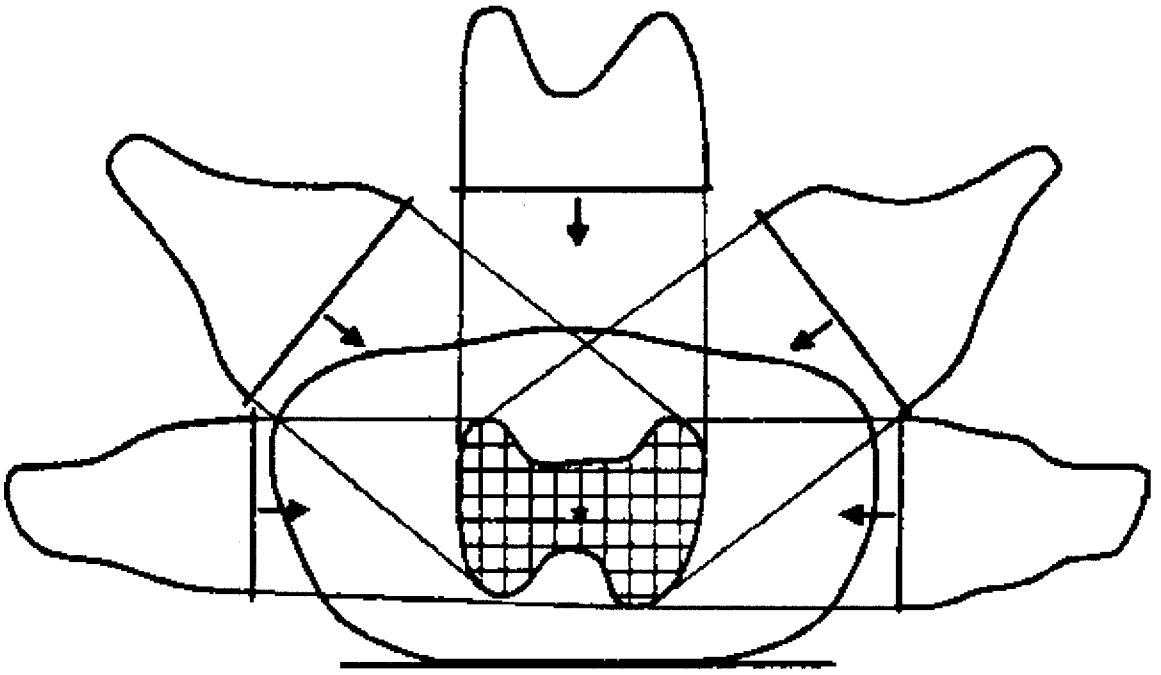

Figure 2-1. *Illustration of IMRT. A number of intensity modulated beams (5 in this case) with their intensity profiles are shown. The schematic shows an axial cut through the patient's body where the hatched area symbolizes the target volume. The intensities are typically reduced in those regions where the rays pass through critical structures and increased where the rays 'see' primarily the target volume. (Brahme, 1988)*

IMRT could not be practically realized in a clinical setting until a multileaf collimator (MLC) was added to an external beam radiation therapy unit. The MLC was first commercially developed as a field shaper for three dimensional conformal radiotherapy (3D-CRT). The MLC consists of a large number of highly absorbing tungsten 'leaves', each of which is driven by computer controlled motors (about 20–80

on each side of the treatment field). The gap between MLC leaves can be adjusted, while the beam is on, and thereby create a large variety of field openings, which can be shaped to conform to the projection of the tumour target volume. In IMRT delivery, the MLC not only shapes the field geometrically, but also modulates the field intensity leaf-by-leaf within the shaped field. Typically, an MLC leaf projects a lateral width of about 0.5 to 1 cm at the isocentre of a treatment unit. The opening of the beam as a basic unit of the intensity modulation is called a beamlet. The use of step-and-shoot and dynamic MLC patterns are the two MLC leaf sequencing algorithms widely used which allow for IMRT delivery.

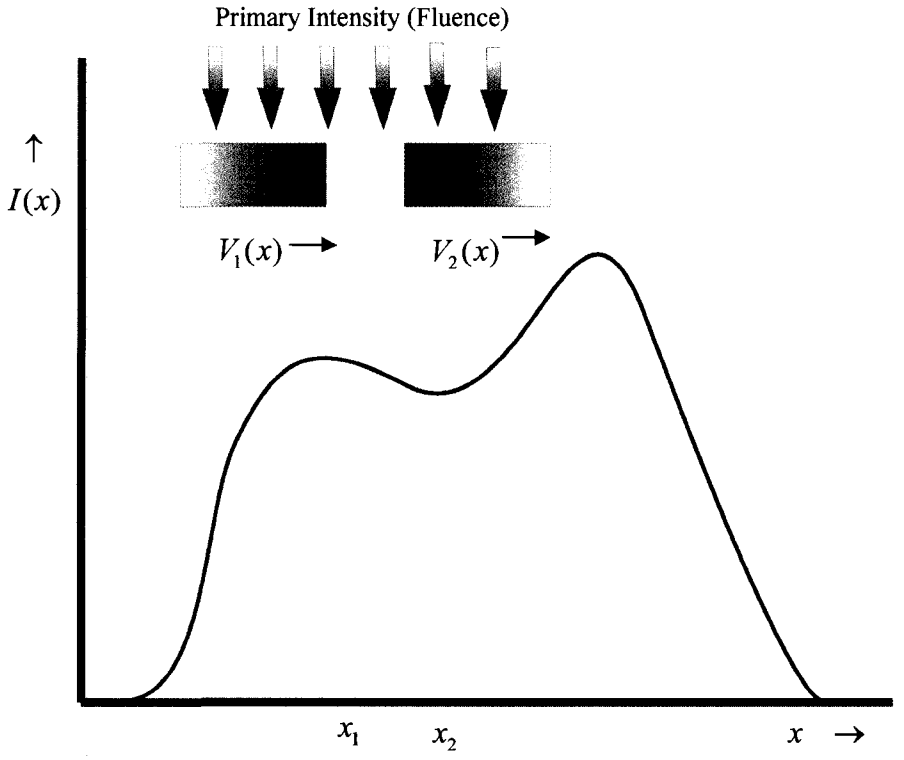

Figure 2-2. *Illustration of dynamic multileaf collimator motion to generate a one-dimensional intensity-modulation profile with one leaf pair (one row of the MLC from Figure 2-2). (Adapted from Khan 2003)*

The intensity modulation of one IMRT field in one beam direction is formed as a succession of discrete field settings ('segments') with a small uniform fluence (i.e., small number of monitor units, MU) delivered to each segment and these subfields are superimposed to generate stratified intensity distributions with a discrete number of intensity levels (Boyer et al., 1991). This discrete mode of IMRT delivery, in which the beam is off while the MLC leaves move to their next position, has been termed the 'step-and-shoot' mode. The step-and-shoot mode is easy to realize and control from the engineering and safety points of view. However, to attain more modulation, more segments are needed. Hence, more total MLC travelling occurs, more monitor units (MU, which is a measure of machine output of a linear accelerator) are needed, and a longer treatment time results. Consequently, the treatment time is a factor to be considered in step-and-shoot IMRT delivery.

In the dynamic MLC mode of IMRT delivery, the opposing leaves sweep simultaneously and unidirectionally across the field, each with a different velocity as a function of time. The period that the aperture between leaves remains open allows the delivery of variable intensity to different points in the field. The method is also called "sliding window." The basic principle of dynamic intensity modulation is illustrated in Figure 2-2. A pair of leaves defines an aperture with the leading leaf 2 moving with velocity $V_2(x)$ and the trailing leaf 1 with velocity $V_1(x)$. Ignoring the transmission through the leaves, penumbra or scattering, the profile intensity $I(x)$ as a function of position x is given by the cumulative beam-on times, $t_1(x)$ and $t_2(x)$. These track the cumulative MUs delivered while point x lies exposed between the inside edges of leaves 1 and 2, respectively, that is:

$$I(x) = t_1(x) - t_2(x) \qquad [2\text{-}1]$$

Differentiating Equation 1 with respect to x gives:

$$\frac{dI(x)}{dx} = \frac{dt_1(x)}{dx} - \frac{dt_2(x)}{dx} \qquad [2-2]$$

or

$$\frac{dI(x)}{dx} = \frac{1}{V_1(x)} - \frac{1}{V_2(x)} \qquad [2-3].$$

Svensson *et al (1994)* gave a simple analytical solution to this problem. To minimize the total treatment time, the optimal solution is to move the faster of the two leaves at the maximum allowed speed, $V_{max}(x)$ and modulate the intensity with the slower leaf: which leaf is the slower, modulating one depends on the intensity gradient. The solution is:

$$\left.\begin{aligned} V_2(x) &= V_{max} \\ V_1(x) &= \frac{V_{max}}{1 + V_{max}(dI(x)/dx)} \end{aligned}\right\} when \quad \frac{dI(x)}{dx} \geq 0 \qquad [2-4]$$

and

$$\left.\begin{aligned} V_1(x) &= V_{max} \\ V_2(x) &= \frac{V_{max}}{1 - V_{max}(dI(x)/dx)} \end{aligned}\right\} when \quad \frac{dI(x)}{dx} < 0 \qquad [2-5].$$

2.2.1.2 Image guided radiotherapy/adaptive radiotherapy

Imaging has always played a crucial role in almost in every step of radiation therapy, including diagnosis, assessment of the extent of the disease, the delineation of target regions to be irradiated, the delineation of the normal tissues to be protected from excessive radiation doses, the generation of treatment plans, the set up of patients, and the alignment of the target volume for treatment delivery. Imaging can also play a role in the monitoring and quality assurance of treatment delivery, follow-up and assessment of

response to treatments, and evaluation of the efficacy of treatment strategies. Without the 3-D volumetric information from CT/MRI to delineate the target regions and normal organs, 3D-CRT and IMRT would not be possible. As images provide guidance in all stages of the radiotherapy process, IGRT in the current context is defined as imaging techniques to augment both the initial treatment plan and treatment delivery in radiotherapy (Mell et al., 2008)

As discussed, the target volume delineation is critically important to IMRT. CT-based tumor delineation is commonly used in most cancer centers. MRI, MRSI, PET and single photon emission computed tomography (SPECT) images may provide additional functional and metabolic information to more precisely delineate the extent of tumor and identify surrounding normal tissues. Ongoing studies indicate that there are substantial inter-fractional and intra-fractional variations in the positions and shapes of the treatment target and normal tissues (Mackie et al., 2003). These variations between planning images and treatment can cause dose delivery errors while using the original treatment plan. The causes of the variations include such things as the setup error, non-rigidity of the body, organ motion (i.e. respiratory motion), weight loss and tumor shrinkage. Discerning these changes inter-fractionally and intra-fractionally and making adjustments to the treatment plan are the cutting-edge developments of IGRT. Image guided adaptive radiotherapy (IGAR) uses daily volumetric imaging produced just prior to or during treatment as a form of feedback to incorporate patient position, organ motion and/or changes of tumor/normal tissues into the treatment plan (Mell et al., 2008).

In-room imaging is gradually coming on line for conventional treatment machines allowing for images to be taken before, during and/or after every fraction of the

radiotherapy treatment. Linacs with some form of imaging device (kilovoltage (kV) cone beam CT, or megavoltage (MV) imagers) mounted on the gantry are widely available. External beam radiotherapy systems with online MRI devices are under development by several groups. (Fallone et al., 2007; Lagendijk et al., 2008; Viewary Inc.). The developments of IGRT/IGAR provide the possibility of imaging the patient in real time and subsequently tracking the target volume with the irradiating fields.

2.2.2 Hi-Art II, helical tomotherapy system with IMRT and IGRT abilities

2.2.2.1 The helical tomotherapy system

The helical tomotherapy concept was invented by Mackie *et al* (1993) and the currently commercially available unit, Hi-Art II, was developed and constructed at the University of Wisconsin-Madison and TomoTherapy Inc., Madison, WI. (Mackie, 2006) It was first approved for clinical use in 2004. The Cross Cancer Institute (CCI) is one of the two earliest research users in Canada and the among the first group of users world wide.

The idea of helical tomotherapy was inspired by spiral (helical) CT systems and as such, the tomotherapy system has a similar configuration to a CT scanner (shown in Figure 2-3). A linac is mounted on the CT ring gantry, which allows the radiation source to rotate around the patient or phantom. A helical pattern of dose deposition in the patient or phantom is achieved as the table continuously moves during source rotation. The target in the linac is 85.0 cm from the rotation axis and the gantry rotation speed is 1-6 rotations per minute within $\pm 2^{\circ}$ accuracy of planned position. The patient couch has position accuracy within 1 mm. The translation speed coincides with the gantry rotation as planned. The translation motion range is 170.0 cm which makes the total body irradiation

for a normal size patient possible. The bore is 85.0 cm in diameter (TomoTherapy-Inc., 2005). An arc detector array with 738 channel Xenon ion chambers with 110 cm radius of curvature is positioned 180° and 145.0 cm away from the radiation source. With the information from 540 of 738 of these detectors, the system can reconstruct a megavoltage photon beam CT (MVCT) image before a treatment, and verify dose delivery during the treatment. The MVCT images have a 40 cm field-of-view (FOV) defined by the largest field size which is limited by the MLC dimensions and 4 mm slice width defined by the jaws. MVCT has three imaging modes: coarse, normal and fine with corresponding couch pitches of 3, 2 and 1, respectively (Mackie et al., 2003; Ruchala et al., 2000; Yartsev et al., 2007). The pitch used here is defined as the ratio of the distance of couch translation in one rotation relative to the radiation field width (T_{slice}) at the isocenter (Mackie *et al.*, 2003).

The linac is operated in two-energy modes, one for treatment and another for MVCT imaging. The linac head is shown in Figure 2-4(a). A 1.5-2 mm diameter monoenergetic electron beam with a nominal energy of 5.7 MeV (treatment mode) or 3.5 MeV (MVCT imaging mode) bombards a tungsten target. The electron beam produces Bremsstrahlung x-rays having a spectrum of energies from zero MeV up to the maximum accelerating potential of the system's mode. The x-ray beam is shaped by the primary collimator after passing through the monitor chamber. The Hi-Art II as a dedicated IMRT and IGAR machine that omits the flattening filter used in traditional linacs. Hence, it has a higher dose rate than a traditional linac. A flat field can be achieved with intensity modulation (Jeraj et al., 2004).

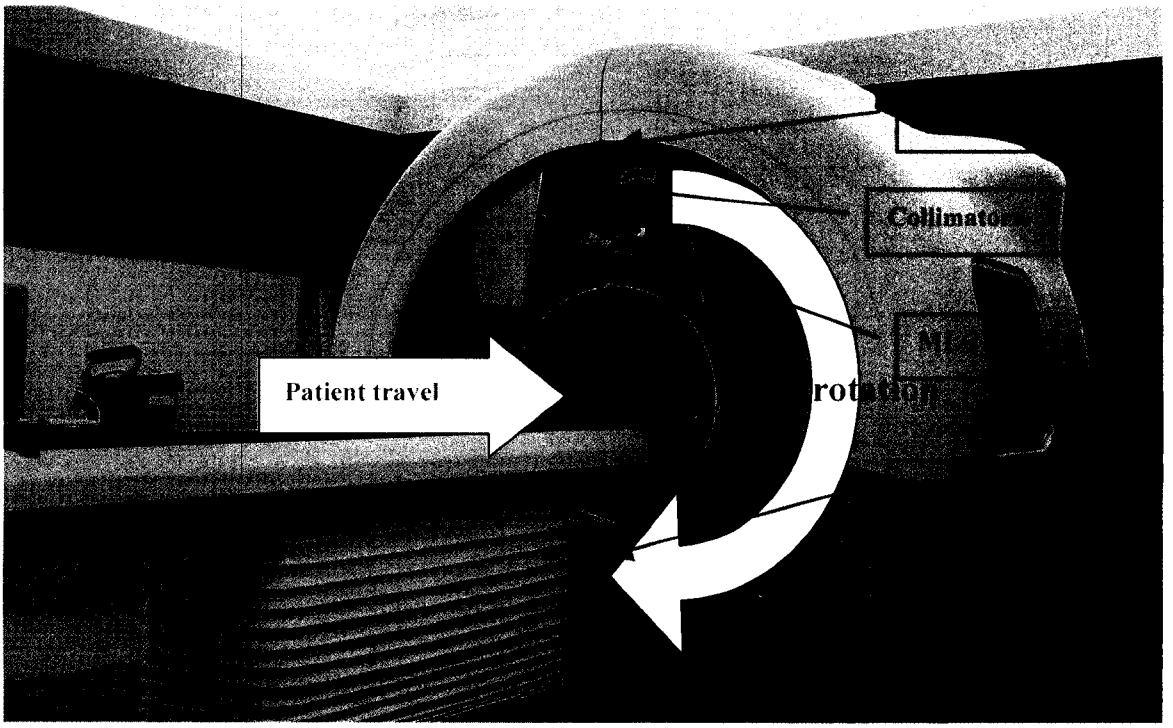

Figure 2-3. *Structures of the Hi-Art II with the front cover removed. (The picture courtesy M. Mackenzie and C. Field)*

The radiation field is further shaped by the secondary collimator (jaws) and MLC. Each of the MLC leaves is made of 10 cm thick tungsten in the beam direction and they provide shielding to make the leakage outside of the field as low as 0.05% and about 0.5% inside the field (Jeraj et al., 2004). The jaws and MLC are all adjustable in the treatment or MVCT imaging mode. They provide a fan shape with the maximum transverse dimension of 40 cm defined by the fully opened MLC, and variable lateral dimension (i.e., slice thickness) of up to 5 cm long at the isocenter, defined by the jaws. Three discrete settings of field lengths of 1.0, 2.5 or 5.0 cm are typically commissioned for the treatment mode and 0.5 cm slice thickness is used in MVCT imaging mode (Jeraj et al., 2004; Langen et al., 2005). At the CCI, the two jaw selections 2.5 and 5.0 cm are commonly used settings and 1.0 cm is used for certain treatments as well.

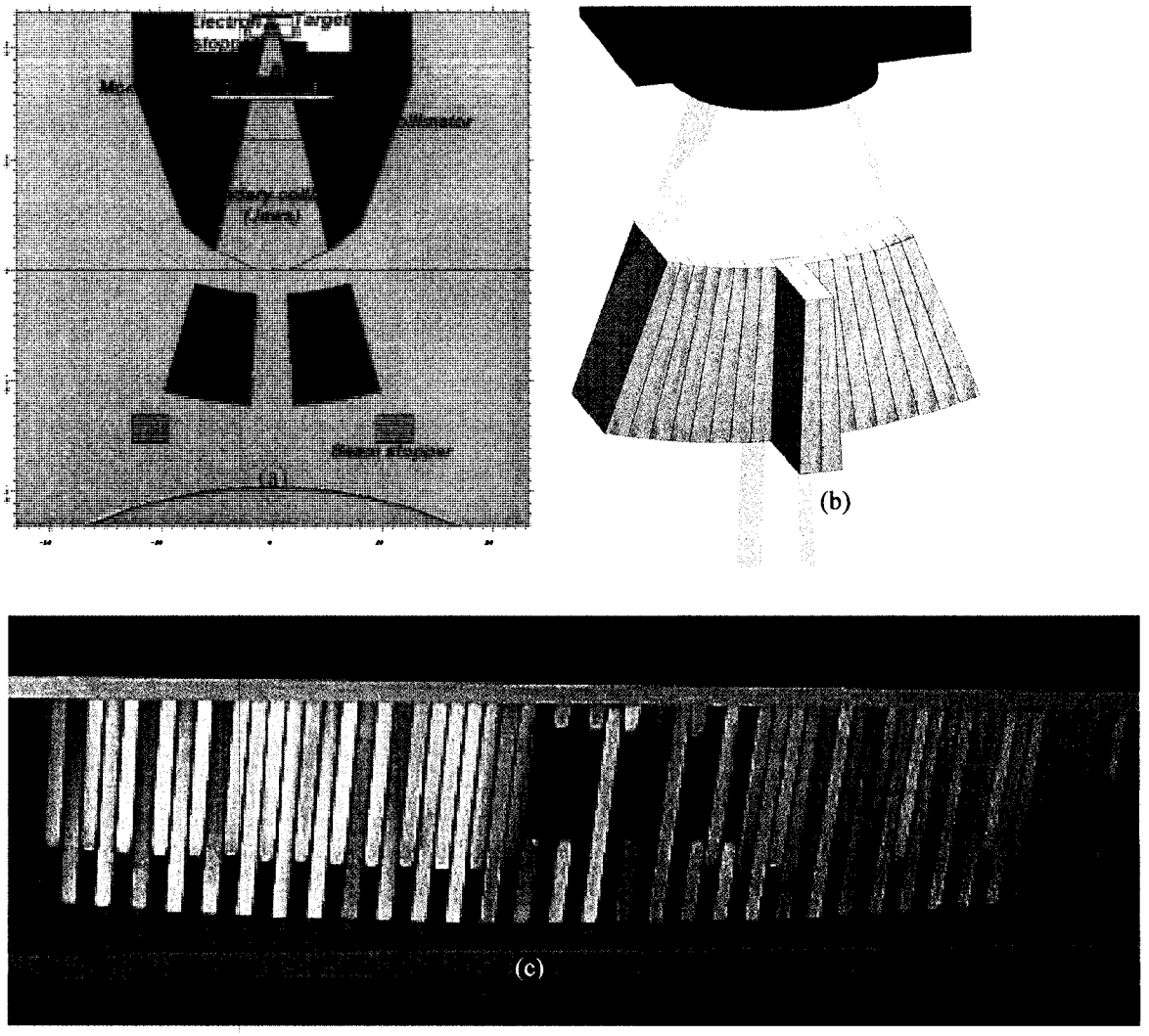

Figure 2-4. ***(a).*** *A cross-sectional diagram of the Hi-Art II head (Jeraj et al., 2004).* ***(b).*** *A conceptual illustration of the dynamic modulation of the beam using a binary MLC in open and closed states. Beamlet weights are controlled by opening times.* ***(c).*** *A picture of the Hi-Art II 64-leaf binary MLC.*

A 64-leaf binary MLC is used in Hi-Art II for intensity modulation. The binary MLC is illustrated in Figure 2-4(b). The position of each leaf is either fully outside the field or completely blocking the field which makes the leaf only have "open" or "closed" states. The 64-leaf MLC is shown in Figure 2-4(c) with leaves in both the open and closed states. Note that the leaves are interdigitated (i.e. adjacent leaves slide in and out

from opposite sides of the opening). A maximum 40 cm opening at the isocenter can be achieved when all 64 leaves are open. One leaf controls an average 0.625 cm wide ray at the isocenter and this ray is called a beamlet. The opening time of each leaf is controlled by the computer optimized treatment plan to modulate the energy fluence. Each leaf is controlled separately and is moved very quickly, by a pneumatic system, in and out of the beam with a typical transition time under 20 ms. The MLC leaves are 10 cm thick tungsten with a tongue and grove structure that keeps the interleaf leakage to about 0.43% and the intraleaf leakage to 0.05%. (Balog et al., 2005; Balog et al., 1999)

Helical tomotherapy integrates the MLC modulation of the continuous rotating slit fan beam into the IMRT delivery. All machine parameters required for treatment delivery such as MLC opening and couch positioning can be controlled relative to the gantry position during gantry rotation. In treatment planning and beam delivery control, the arc delivery is simplified as 51 discrete angles per rotation. Each of these gantry angles is called a projection, which is about 7.06° from its abutting projection. When and where an MLC is opened and how long it remains open is controlled by a file which is termed the sinogram file. This file contains a 2D array which takes projection number and MLC number as coordinates, with the array values containing the relative opening time of the MLC at that projection. This array is called a MLC control sinogram (shown in Figure 2-5).

The Hi-Art II system consists of a Planning Station, an Operator Station, an Optimization Server and a Data Server along with a delivery system.

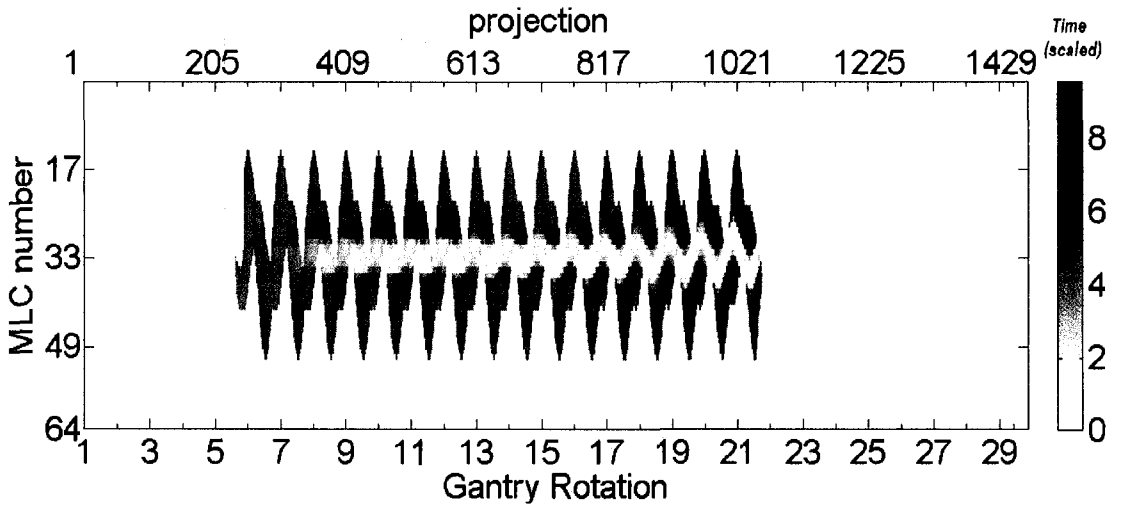

Figure 2-5. *MLC control sinogram of Hi-Art II. The gantry positions are simplified as 51 projections per rotation. The opening time of each of the 64 leaves is determined by the treatment plan.*

The Planning Station and the Operator Station are the two user interfaces that control the Hi-Art II system. The Planning Station is used to prescribe a treatment and calculate an optimized plan for treatment based on a 3D CT data set and anatomic and target data. The Operator Station (located just outside the treatment room) is used to perform MVCT scans and treatment procedures after the patient has been positioned for their treatment. The Operator Station is also used to perform image registration after an MVCT scan has been acquired.

The Optimization Server is where the dose optimization calculations are performed. This device uses a dedicated 16 CPU cluster to accelerate the optimization process. It communicates with the Planning Station in an interactive planning procedure.

The Data Server (located with the Optimization Server) is used to store data for rapid search and retrieval and is connected to the Optimization Server, Planning Station, and Operator Station. Data required to perform the beam delivery (machine data) and

deliver prescribed treatments to the patient (patient data) is stored in the Data Server. The patient data in the Data Server can be archived/restored via the Planning Station. The entire data for a patient can be archived to a folder with binary and Extensible Markup Language (XML) format files for backup. The archived patient treatment data can be accessed and analyzed using in-house custom tools for performing clinical studies.

2.2.2.2 Helical tomotherapy IMRT and IGAR procedures

The IGAR flowchart model for helical tomotherapy is shown in Figure 2-6. The patient's 3-D images are obtained by kilo-voltage CT (kVCT), MRI or PET scanners and the images are used for delineating the PTV and Organs (Regions) at Risk (OARs or RARs) by radiation oncologists. The volume delineation is performed on a third-party Treatment Planning System (TPS), such as Eclipse (Varian Medical, Palo Alto, CA) or Helax (Nucletron, Veenendaal, Netherlands).

The patient kVCT datasets are then transferred via DICOM to the Hi-Art II system and the following tasks are performed on it: an inverse treatment plan is generated, which is to say beamlet weights (intensity modulation levels) are determined that satisfy the user defined dose distribution goals. In the inverse treatment planning method, the dose distribution criteria (treatment goals or constraints) are defined by a set of parameters. The parameters for the tumor volume or volumes are based on a dose volume histogram (DVH) point and the prescription dose as well as maximum and minimum dose constraints. The parameters for the OARs are based on what is deemed an acceptable DVH point as a maximum dose constraint. A rough estimate of the optimal dose distribution is calculated using initial beamlet weights. An objective function value is calculated using the differences between the current dose distribution and the treatment

goals. An update factor for each beamlet weight is determined by using this difference and the update factor is used to adjust the beamlet to get a new dose distribution. This optimization is iterated until the objective function value is minimized and the treatment goals are met as closely as they can be. Then, the computer optimized results are evaluated by an oncologist (Shepard et al. 2000). In helical tomotherapy planning, region importance values and PTV or OAR dose violation penalties are specified for iterative optimization. Treatment settings such as field width, pitch and modulation factor need to be specified before optimization. Field width is defined by jaw setting as mentioned previously. Pitch is the ratio of displacement of patient couch travel in one rotation relative to the field width (for example, a pitch of 0.5 and jaw width of 2.5 cm would mean the couch travels 1.25 cm per revolution). The modulation factor is the ratio of the maximum open time for a leaf to the mean open time of all MLC leaves that are open in a projection. (Kron et al., 2004).

After the optimized treatment plan is accepted by the oncologist and before it is used on the patient, a patient-specific delivery quality assurance (DQA) is performed to verify the accurate delivery of this mechanically demanding plan. The DQA process uses the treatment MLC control sinogram and couch/gantry settings to deliver the prescribed dose to a solid water phantom instead of the patient. The recalculated dose distribution is compared with an absolute ionization chamber measurement and a relative radiographic film dose distribution measurement. The DQA process has the potential to find setup errors according to the position of fiducial markers, errors made by the planning software, or errors associated with mechanical limitations relating to a specific plan, which may

result in an incorrect absolute dose or relative dose distribution (Mackie et al., 2003; Thomas et al., 2005; Van Dyk, 2007).

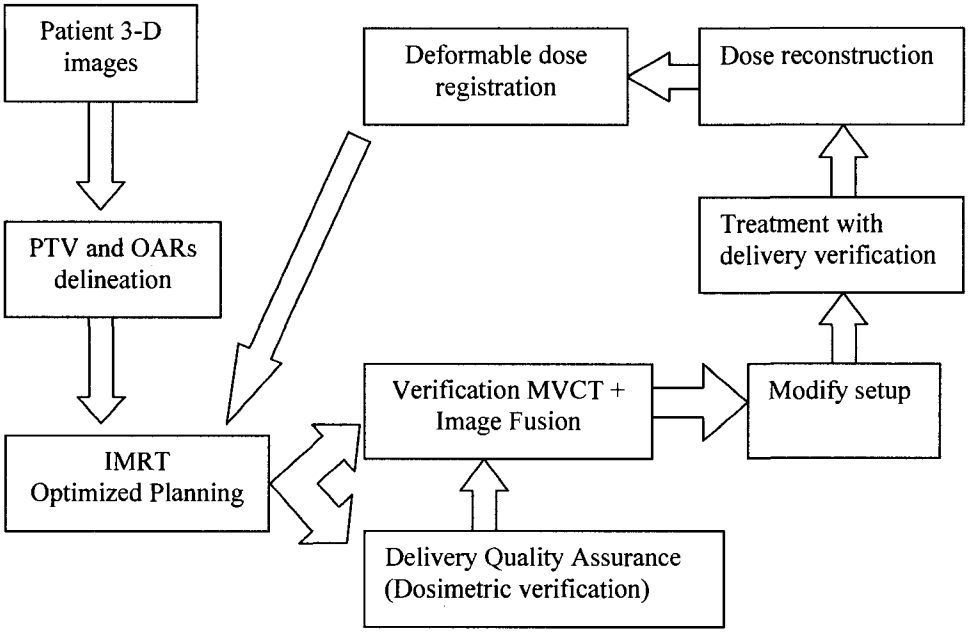

Figure 2-6. *Helical tomotherapy procedures with IMRT and IGAR*

Patient IMRT treatment begins with an MVCT scan on the Hi-Art II unit. An MVCT is performed before the dose delivery in every fraction to provide information as to the patient setup position and organ locations. In each treatment, the patient shift is identified by the fusion of images of the MVCT and the planning kVCT. According to the shift between the images, Hi-Art II can make couch adjustments and initial gantry angle shifts to set up the patient as closely as possible to the planning kVCT position and thereby perform an image guided adaptation for each treatment.

Offline IGAR has been studied by many researchers for helical tomotherapy (Langen et al., 2005; Mackie et al., 2003; Wu et al., 2002). In one approach to dosimetric adaptation, the pre-treatment MVCT images over the first several fractions are assumed

as the actual patient position in the optimized plan. These images are used to reconstruct the delivered dose distribution by projecting the planning sinogram through the MVCT data set. The translated or deformed target and OARs cause differences between the planned and delivered doses. When the dose differences obtained by deformable dose registration accumulate to a certain level, new objectives need to be introduced into the plan. With the new objectives, a new optimized IMRT plan is applied, which would compensate the underdose regions and lessen the overdose regions in the remaining treatment fractions.

2.2.2.3 Hi-Art II TPS optimization and dose calculation algorithms

As mentioned above, helical tomotherapy has the advantage of irradiating from a large number of gantry angles (specified by as 51 delivery projections per rotation in the current Hi-Art II system) in IMRT compared with conventional linac IMRT. In each projection, 64 beamlets are regulated by the binary MLC. The TPS first determines which beamlets pass through the defined PTV. Those are left open, while all other beamlets are closed. Although helical tomotherapy delivers arc beams in treatment, the TPS simplifies it as a fixed angle at that projection. Within a treatment plan having 10-20 rotations, the potential beamlet number could be in the tens of thousands for the optimization, which determines each beamlet weight controlled by the MLC leaf opening time. Both optimization and dose calculation are crucial to the final treatment dose of the patient.

A. Optimization algorithm

The Hi-Art II TPS uses an iterative least-squares minimization approach as described by Olivera et al. (1998) and Shepard et al. (2000). In the optimization, the objective function is defined as:

$$O(\vec{\Psi}) = \sum_{T}\sum_{i\in t} \frac{\alpha_t \beta_{t_i,\max} \beta_{t_i,\min}}{N_t} (D_i^{p_t} - D_i^{d_t})^2 + \sum_{R}\sum_{i\in r} \frac{\alpha_r \beta_{r_i,\max} \beta_{r_i,dvh}}{N_r} (D_i^{p_r} - D_i^{d_r})^2 \qquad [2-6].$$

Here $\vec{\Psi}$ is the vector energy fluence,

$\sum_{T}$ is the summation over all targets *T*,

$\sum_{i\in t}$ is the summation over all voxels *i* that are a member of a target *t*,

α_t is the importance value for a target *t* as entered on the Planning Station,

$\beta_{t_i,\max}$ is the Maximum Dose Penalty for a target *t* (as entered on the Planning Station) if the dose deposited in voxel *i* is greater than the Maximum Dose for that target *t* (as specified on the Planning Station). Otherwise $\beta_{t_i,\max}$ equals 1,

$\beta_{t_i,\min}$ is the Minimum Dose Penalty for a target *t* (as entered on the Planning Station) if the dose deposited in voxel *i* is less than the Minimum Dose for that target *t* (as specified on the Planning Station). Otherwise $\beta_{t_i,\min}$ equals 1,

N_t is the number of voxels in target *t*,

$D_i^{p_t}$ is the dose prescribed to voxel *i* for target *t*,

$D_i^{d_t}$ is the deposited dose in voxel *i* for target *t*,

$\sum_{R}$ is the summation over all regions-at-risk (OAR) *R*,

$\sum_{i\in r}$ is the summation for all voxels *i* that are a member of OAR *r*,

α_r is the Importance value for a OAR *r* as entered on the Planning Station,

$\beta_{r_i,\max}$ is the Maximum Dose Penalty for a OAR *r* (as entered on the Planning Station) if the dose deposited in voxel *i* is greater than the Maximum Dose for that OAR *r* (as specified on the Planning Station). Otherwise $\beta_{r_i,\max}$ equals 1,

$\beta_{r_i,dvh}$ is the DVH Dose Penalty for a OAR r (as entered on the Planning Station) if the dose deposited in voxel i is between the DVH Dose (as specified for that OAR r on the Planning Station: D_{DVH_r}) and D', where D' is the dose at which the DVH line for that OAR r crosses the horizontal line defined at the volume level V_{DVH} (the DVH Volume specified for that OAR r on the Planning Station). If D' is less than or equal to D_{DVH_r}, $\beta_{r_i,dvh}$ equals 1,

N_r is the number of voxels in OAR r,

$D_i^{p_r}$ is the dose prescribed to voxel i for OAR r,

$D_i^{d_r}$ is the deposited dose in voxel i for OAR r.

Then, the fluence update equation is found by solving Equation 6 for its minimum value. This leads to the following, which is used to update the fluence value for each leaf in a given projection:

$$\Psi_j^{[k+1]} = \Psi_j^{[k]} \left[\frac{\sum_T \sum_{i \in t} \frac{\alpha_t \beta_{t_i,\max} \beta_{t_i,\min}}{N_t} d_{ij} D_i^{p_t}}{\sum_T \sum_{i \in t} \frac{\alpha_t \beta_{t_i,\max} \beta_{t_i,\min}}{N_t} d_{ij} D_i^{d_t\,[k]} + \sum_R \sum_{i \in r} \frac{\alpha_r \beta_{r_i,\max} \beta_{r_i,dvh}}{N_r} d_{ij} D_i^{d_r\,[k]}} \right] \qquad [2-7]$$

where $\Psi_j^{[k+1]}$ is the energy fluence for leaf j at iteration $k+1$,

$\Psi_j^{[k]}$ is the energy fluence for leaf j at iteration k,

d_{ij} is the dose contribution to voxel i from leaf j per unit of energy fluence,

$D_i^{d_t\,[k]}$ is the dose deposited in voxel i of target t for the kth iteration,

$D_i^{d_r\,[k]}$ is the dose deposited in voxel i of OAR r for the kth iteration.

The new energy fluence of a beamlet is updated based on the previous iteration by the update factor in Equation 7. This update factor is obtained by querying all of the voxels influenced by the leaf and adding contributions for voxels in the target and OARs

(Shepard et al., 2000). The iterative optimization in the current Hi-Art II TPS is stopped by a user specified iteration number (i.e. 20 iterations) or by a user interactive command when the plan is acceptable, even though, an extreme value of the objective function has not been reached yet.

B. Convolution/ Superposition dose calculation algorithm

The Hi-Art II TPS calculates dose distributions using 3-D density information provided by a planning kVCT image set. The Picker PQ 5000 kVCT scanner has a 48.0 cm FOV with 512×512 resolution. By default, the Hi-Art II downsamples the CT images to 256×256 for planning. The TPS provides three dose calculation grid options: Coarse, Normal and Fine, and these settings use respectively, multiples of 4, 2 and 1 of the downsampled planning CT pixel size. Hence, the dose calculation grid can be 64×64, 128×128 and 256×256. The slice thickness is typically 2-3 mm. Thereby, the voxel size in dose calculation could be 7.5×7.5×2-3 mm^3, 3.75×3.75×2-3 mm^3 or 1.875×1.875×2-3 mm^3.

The TPS has three calculation algorithms with different calculation speeds and accuracies for treatment plan optimization. In the faster calculation, the calculation accuracy will be compromised. Total Energy Released per unit MAss (TERMA) algorithm is the fastest and the least accurate algorithm. The absorbed dose is approximated by TERMA from the primary beam, which is the product of the mass attenuation coefficient and the primary beam energy fluence at a given point. The Full Scatter algorithm considers scattered dose and gives better accuracy than the TERMA method. It spends several minutes to calculate dose for each iteration. TERMA and Full Scatter algorithms would only used in the initial optimization in the first several iterations,

but are not typically used in practice. The Beamlet method for optimization uses a collapsed-cone convolution/superposition algorithm to calculate the dose distribution resulting from each open beamlet. Several hours are needed for the pre-calculation of all possible beamlets that would contribute to the dose distribution in one plan. After the beamlet doses are calculated, the software spends several minutes to optimize the weight of each open beamlet (each iteration taking approximately 15 seconds, and iterating for about 20 iterations). After the optimization, the final dose is obtained by summing all beamlet doses calculated by the collapsed-cone convolution/superposition algorithm.

Convolution/Superposition is a kernel-based algorithm where the dose deposition is viewed as a superposition of appropriately weighted responses (kernels) to point irradiations (TERMA). Convolution can be applied to efficiently calculate the superposition assuming the kernels are spatially invariant. The TERMA and kernel calculations are two parts of the algorithm. The deposited dose at point $\vec{r}$, $D(\vec{r},h\nu)$ for a mono-energetic photon beam in a homogeneous medium can be calculated as Equation 8.

$$D(\vec{r},h\nu)=\int T(\vec{r}',h\nu)A(\vec{r}-\vec{r}',h\nu)d\vec{r}' \qquad [2-8]$$

where $A(\vec{r}-\vec{r}',h\nu)$ is the convolution kernel for photons with energy $h\nu$. The kernel represents the relative energy deposited by electrons set in motion by primary photon interactions per unit of volume. The kernels used by the TPS were calculated for a photon beam in a water medium and were generated by Mackie et al. (1988) with the EGS4 Monte Carlo code. The TERMA $T(\vec{r}',h\nu)$ can be computed from the mass attenuation coefficient $\frac{\mu}{\rho}(h\nu)$ and the primary photon energy fluence $\Psi(\vec{r}',h\nu)$ at point $\vec{r}'$ as shown in Equation 9: (Mackie and Reckwerdt, 2001)

$$T(\vec{r}', hv) = \frac{\mu}{\rho}(hv)\Psi(\vec{r}', hv) \qquad [2-9]$$

The algorithm needs 3-D convolution over every voxel and this can become computationally intensive. To reduce the burden of computation, collapsed-cone convolution/superposition is used in the TPS dose calculation. In the collapsed cone approximation, all energy released into coaxial cones of equal solid angle, from volume elements on the cone axis, is rectilinearly transported, attenuated and deposited in elements on the axis. Then the 3-D kernel is simplified as a 1-D model with the number of collapsed cone directions (Ahnesjö, 1989).

Convolution/superposition needs to deal with the density inhomogeneities in patients. With variable electron density between voxels, the TERMA is corrected by using the radiological path length, which is the physical path length times the density along the path, (instead of physical path length), in its calculation. The kernels are then modified by scaling them according to the electron range in water with a density given by the local medium. Then, Equitation 8 is formulated as Equation 10:

$$D(\vec{r}, hv) = \int T(\rho_{\vec{r}'} \cdot \vec{r}', hv) A(\rho_{\vec{r}-\vec{r}'} \cdot (\vec{r} - \vec{r}'), hv) d\vec{r}' \qquad [2-10]$$

In the Hi-Art II TPS dose kernel heterogeneity density scaling and TERMA correction, the mass density instead of the electron density is used. The assumption for this approximation is that the electron density is approximately proportional to the mass density for the materials concerned in radiotherapy (Lu et al., 2005).

The convolution/superposition algorithm used in the TomoTherapy TPS for a poly-energetic photon beam is:

$$D(\vec{r}, MV) = \int T(\rho_{\vec{r}'} \bullet \vec{r}', MV) K(\rho_{\vec{r}-\vec{r}'} \bullet (\vec{r} - \vec{r}'), MV) d\vec{r}' \qquad [2-11]$$

Where

$$T(\rho_{\vec{r}'} \bullet \vec{r}', MV) = \int \frac{\mu}{\rho}(hv) \frac{d\Psi(\rho_{\vec{r}'} \bullet \vec{r}', hv)}{dhv} dhv \qquad [2-12]$$

and

$$K(\rho_{\vec{r}-\vec{r}'} \bullet (\vec{r} - \vec{r}'), MV) = \frac{\int \frac{\mu}{\rho}(hv) \frac{d\Psi(\rho_{\vec{r}'} \bullet \vec{r}', hv)}{dhv} A(\rho_{\vec{r}-\vec{r}'} \bullet (\vec{r} - \vec{r}'), hv) dhv}{\int \frac{\mu}{\rho}(hv) \frac{d\Psi(\rho_{\vec{r}'} \bullet \vec{r}', hv)}{dhv} dhv} \qquad [2-13]$$

The Hi-Art II has a characteristic beam energy spectrum studied by Jeraj et al. (2004) using the Monte Carlo method. The kernel, $K(\rho_{\vec{r}-\vec{r}'} \bullet (\vec{r} - \vec{r}'), MV)$ and TERMA, $T(\rho_{\vec{r}'} \bullet \vec{r}', MV)$ were composed for the spectrum by weighting each kernel and the TERMA for each energy by its contribution to the spectrum.

The density scaling method of Mackie et al.'s photon beam kernels was evaluated for air/water inhomogeneities by Woo and Cunningham (1990). Convolution/superposition with the kernel gave better agreement with Monte Carlo results than the previous generation of correction-based algorithms. But discrepancies were seen at the air/water interface, and the discrepancies increased with a larger air gap, smaller beam radius and higher photon energy. In general, the convolution/superposition algorithm provides a relatively accurate and fast means of calculating dose in the majority of clinical scenarios. However, comparisons with MC calculations and measurements have shown that it can introduce significant errors when its CPE assumptions are not valid. The MC method is still the preferred choice when considering accuracy in the presence of heterogeneity (Woo and Cunningham, 1990).

Bibliography:

Ahnesjö, A. (1989): Collapsed cone convolution of radiant energy for photon dose calculation in heterogeneous media. *Med. Phys.* **16**, 577–92.

American Cancer Society (2006): Cancer Facts and Figures, American Cancer Society, Atlanta.

Balog, J. P., Lucas, D., DeSouza, C., and Crilly, R. (2005): Helical tomotherapy radiation leakage and shielding considerations. *Med. Phys.* **32**, 710-9.

Balog, J. P., Mackie, T. R., Wenman, D. L., Glass, M., Fang, G., and Pearson, D. (1999): Multileaf collimator interleaf transmission. *Med. Phys.* **26**, 176-86.

Bortfeld, T. (2006): IMRT: a review and preview. *Phys. Med. Biol.* **51**, R363-R379.

Boyer, A. L., Desobry, G. E., and Wells, N. H. (1991): Potential and limitations of invariant kernel conformal therapy. *Med. Phys.* **18**, 703–12.

Brahme, A. (1988): Optimization of stationary and moving beam radiation therapy techniques. *Radiother.Oncol.* **12**, 129-40.

Brahme, A., Roos, J. E., and Lax, I. (1982): Solution of an integral equation encountered in rotation therapy. *Phys. Med. Biol.* **27**, 1221-9.

Fallone, B. G., Carlone, M., Murray, B., Rathee, S., Stanescu, T., Steciw, S., Wachowicz, K., and Kirkby, C. (2007): Development of a linac-MRI system for real-time ART. AAPM Minneapolis 49th Annual Meeting.

Hall, E. J. (2006): Intensity-modulated radiation therapy, protons, and the risk of second cancers. *Int. J. Radiation Oncology Biol. Phys.* **65**, 1-7.

Hall, E. J., and Giaccia, A. J. (2006): Radiobiology for the radiologist, Lippincott Williams & Wilkins, Philadelphia.

ICRU-50 (1993): Prescribing, recording and reporting photon beam therapy ICRU Report 50

ICRU-62 (1999): Prescribing, recording and reporting photon beam therapy (Supplement to ICRU report 50) ICRU Report 62.

Jeraj, R., Mackie, T. R., Balog, J., Olivera, G., Pearson, D., Kapatoes, J., Ruchala, K., and Reckwerdt, P. (2004): Radiation characteristics of helical tomotherapy. *Med. Phys.* **31**, 396-403.

Johns, H. E., and Cunningham, J. R. (1983): *The physics of radiology*. Charles C. Thomas. Springfield, Ill., U.S.A.

Khan, F. M. (2003): *The physics of radiation therapy*. Lippincott Williams & Wilkins. Philadelphia.

Kron, T., Grigorov, G., Yu, E., Yartsev, S., Chen, J. Z., Wong, E., Rodrigues, G., Trenka, K., Coad, T., Bauman, G., and Van Dyk , J. (2004): Planning evaluation of radiotherapy for complex lung cancer cases using helical tomotherapy. *Phys. Med. Biol.* **49**, 3675-90.

Lagendijk, J. J., Raaymakers, B. W., Raaijmakers, A. J., Overweg, J., Brown, K. J., Kerkhof, E. M., van der Put, R. W., Hardemark, B., van Vulpen, M., and van der Heide, U. A. (2008): MRI/linac integration. *Radiother Oncol* **86**, 25-9.

Langen, K. M., Meeks, S. L., Poole, D. O., Warner, T. H., Willoughby, T. R., Kupelian, P. A., Ruchala, K. J., Haimerl, J., and Olivera, G. H. (2005): The usage of megavoltage CT (MVCT) images for dose recomputations. *Phys. Med. Biol.* **50**, 4259-76.

Lu, W., Olivera, G. H., Chen, M., Reckwerdt, P., and Mackie, T. R. (2005): Accurate convolution/superposition for multi-resolution dose calculation using cumulative tabulated kernels. *Phys. Med. Biol.* **50**, 655-80.

Mackie, T., A., Bielajew, A. F., Rogers, D. W. O., and Battista, J. J. (1988): Generation of photon energy deposition kernels using the EGS Monte Carlo code. *Phys. Med. Biol.* **33**, 1-20.

Mackie, T. R. (2006): History of tomotherapy. *Phys. Med. Biol.* **51**, R427–R453.

Mackie, T. R., Holmes, T., Swerdloff, S., Reckwerdt, P., Deasy, J. O., Yang, J., Paliwal, B., and Kinsella, T. (1993): Tomotherapy: a new concept for the delivery of dynamic conformal radiotherapy. *Med. Phys.* **20**, 1709-19.

Mackie, T. R., Kapatoes, J., Ruchala, K., Lu, W., Wu, C., Olivera, G., Forrest, L., Tome, W., Welsh, J., Jeraj, R., Harari, P., Reckwerdt, P., Paliwal, B., Ritter, M., Keller, H., Fowler, J., and Mehta, M. (2003): Image guidance for precise conformal radiotherapy. *Int. J. Radiation Oncology Biol. Phys.* **56**, 89–105.

Mackie, T. R., and Reckwerdt, P. J. (2001): The convolution algorithm in IMRT. 3-D Conformal and Intensity Modulated Radiation Therapy, pp. 179-90. In J. Purdy, W. G. III, J. Palta, B. Butler, and C. Perez. (Eds), Advanced Medical Publishing Inc, Madison, WI.

Mell, K. L., Pawlicki, T., Jiang, S. B., and Mundt, A. J. (2008): Image-Guided Radiation Therapy. In E. C. Halperin, C. A. Perez, and L. W. Brady (Eds): *Perez and Brady's principles and practice of radiation oncology*, Lippincott Williams & Wilkins, Philadelphia.

Olivera, G. H., Shepard, D. M., Reckwerdt, P. J., Ruchala, K., Zachman, J., Fitchard, E. E., and Mackie, T. R. (1998): Maximum likelihood as a common computational framework in tomotherapy. *Phys. Med. Biol.* **43**, 3277-94.

Ruchala, K. J., Olivera, G. H., Kapatoes, J. M., Schloesser, E. A., Reckwerdt, P. J., and Mackie, T. R. (2000): Megavoltage CT image reconstruction during tomotherapy treatments. *Phys. Med. Biol.* **45**, 3545-62.

Shepard, D. M., Olivera, G. H., Reckwerdt, P. J., and Mackie, T. R. (2000): Iterative approaches to dose optimization in tomotherapy. *Phys. Med. Biol.* **45**, 69-90.

Svensson, R., Kallman, P., and Brahme, A. (1994): An analytical solution for the dynamic control of multileaf collimators *Phys. Med. Biol.* **39**, 37-61

Thomas, S. D., Mackenzie, M., Field, G. C., Syme, A. M., and Fallone, B. G. (2005): Patient specific treatment verifications for helical tomotherapy treatment plans. *Med. Phys.* **32**, 3793-3800.

TomoTherapy-Inc. (2005): Hi-Art system physics guide. *TomoTherapy Inc.,T-USR-HB0013G-0905.*

Van Dyk, J. (2007): Quality Assurance. In F. M. Khan (Ed.): *Treatment planning in radiation oncology*, Lippincott Williams & Wilkins, Philadelphia.

Viewray_Inc.: www.viewray.com.

WHO (2007): *The World Health Organization's fight against cancer: strategies that prevent, cure and care*. ISBN 978 92 4 159543 8 (NLM classification: QZ 200).

Woo, M. K., and Cunningham, J. R. (1990): The validity of the density scaling method in primary electron transport for photon and electron beams. *Med. Phys.* **17**, 187-94

Wu, C., Jeraj, R., Olivera, G. H., and Mackie, T. R. (2002): Re-optimization in adaptive radiotherapy. *Phys. Med. Biol.* **47**, 3181-95

Yartsev, S., Kron, T., and Van Dyk, J. (2007): Tomotherapy as a tool in image-guided radiation therapy (IGRT): theoretical and technological aspects. *Biomed Imaging Interv. J.* **3**, e17.

Chapter 3 : Introduction to Monte Carlo in external photon beam radiotherapy

3.1 The Monte Carlo Method

The Monte Carlo (MC) method uses random sampling of known probability distributions to numerically solve a mathematical or physical problem. It is suitable for solving radiotherapy questions, in which charged or uncharged particles interact with medium and set charged particles in motion to deposit energy along their trajectories through the medium (Bielajew, 2001).

MC is widely applied to photon and electron radiotherapy problems in modern radiation therapy and is becoming popular with proton therapy as well. Although the photon and electron interaction processes are well understood, the problems involving radiation transport in the geometries of an accelerator or a patient are often too complex to be solved analytically without resorting to gross approximations. MC generally breaks down the transport process to an event-by-event problem from which the macroscopic behavior of a given system can be extracted on a statistical basis. The major photon interaction processes relevant to radiotherapy problems include: Compton scattering (incoherent scattering) from atomic electrons, the photoelectric effect, pair production and Rayleigh scattering (coherent scattering). The major electron or positron interaction processes include: Möller scattering for electrons from atomic electrons, Bhabha scattering for positrons from atomic electrons, bremsstrahlung photon creation in the nuclear field, positron annihilation with atomic electrons, elastic scattering of electrons and positrons from nuclei and excitation of atoms and molecules by electrons and

positrons. These interactions are more thoroughly discussed in such texts as Johns and Cunningham (1983) and Attix (1986).

3.1.1 Processes of Monte Carlo

The MC process in radiation therapy can be illustrated by a simplified example of tracking a 1.0 MeV photon traveling through an infinite slab of water (Siebers et al., 2005). The photon interaction probability is related to the total cross section, $\sum_{total}$, which is simply a sum of Compton and photoelectric cross sections. Note that at this energy and in this medium, Rayleigh scattering and pair production can be ignored (Johns and Cunningham, 1983), so $\sum_{total} = \sum_{Compton} + \sum_{PhotoEffect}$. Given the known cross section and a random number η uniformly distributed between 0 and 1, the distance x that the photon travels before an interaction occurs is $x = -\ln(\eta) / \sum_{total}$, due to the exponential attenuation. The type of interaction that occurs at x can be determined by the fractional probability of each interaction. A new random number η is generated. If $\eta \leq \sum_{Compton} / \sum_{total}$, then a Compton scattering event is presumed to occur; otherwise a photoelectric event occurs. Then, energy and angular distributions of the scattered photon or electrons are determined in the same manner using new random numbers and corresponding probability distributions. All subsequent events including those from secondary and higher order offspring particles make up the history of the primary particle. The simulation continues until these particles escape the defined geometry or their energies become lower than a preset threshold at which time they are considered stopped at the point of interaction (Siebers et al., 2005).

3.1.2 Advantages of Monte Carlo

The principal advantage of the MC algorithm is the ability to accurately compute radiation dose for arbitrarily complex fluence patterns in arbitrarily complex geometric media. It provides an accurate means of making dosimetry predictions in situations that are difficult or even impossible to measure. Additionally, it can provide shorter times to solution as compared to analytic methods in solving highly complex problems (Bielajew, 2001; Siebers et al., 2005).

3.1.2.1 Accuracy

The MC algorithm is considered to be the method which should potentially give the most accurate dose distribution predictions in radiation therapy (Mohan, 1997). As described above in the MC process, the accuracy of the MC method is due to performing a direct simulation of the microscopic processes of radiation interactions using sampling probability distributions based on the physical laws of nature. Unlike the conventional dose calculation algorithms (non-MC), such as the convolution / superposition algorithm, MC doesn't rely on the assumption of charged particle equilibrium (CPE) to make an accurate calculation. It simulates radiation transport with minimal approximations even in the presence of complex heterogeneous geometries. Thus, MC is able to perform accurate calculations of absorbed dose for a wide variety of materials, devices, modalities and anatomic geometries (Siebers et al., 2005).

Experiment has shown that agreement better than 1% can be achieved between MC linac simulations/dose calculations and measurements in the same situation by fine tuning the parameters used in accelerator simulations (Ma and Jiang, 1999; Sheikh-Bagheri et al.,

2000). High-precision measurements with ion chamber in phantom can be predicted to within 0.3% by MC simulations (Ma et al., 1997).

3.1.2.2 Direct simulation

Almost every part of an external beam radiation treatment can be directly simulated using the MC method. Simulations in the detailed geometries and real materials of a radiation treatment system such as Hi-Art II can provide output fluence and beam characteristic information (Jeraj et al., 2004). Radiation beams produced at a target can be transported through the beam modifying components of an accelerator head including a flattening filter, monitor chambers, jaws and MLC, with all primary and scattered components of the beam accurately modeled. The dosimetric effects caused by all the primary and scattered particles are automatically accounted for. In some conventional dose calculation algorithms, the scattered photon or contaminant electrons are added in separately or ignored (Van Esch et al., 2006).

The direct simulation of a radiation source with the MC method allows a virtual machine models to be built and allows one to study design characteristics and dosimetric effects without any physical investment (e.g. Kirkby et al., 2008).

3.1.2.3 Simulation of difficult to measure situations

Dose verification and knowledge of beam characteristics are critical to performing accurate dose calculations in treatment planning. Current radiation detecting instruments often either can not physically access the points of interest (in a patient or phantom) or will disturb of the actual particle fluence in the region. Patient *in vivo* dose measurement, for instance, is extremely limited, although it is highly desirable in clinical practice. The dose deposition kernels used in convolution / superposition are difficult to measure. The

energy fluence spectra from radiation beams are also needed for convolution / superposition-based dose calculations within various treatment planning systems. All these difficulties can be solved by MC simulations with the capability of tracing the interactions, positions, directions, energies and final deposition of each particle in arbitrary materials and arbitrary geometries (Jeraj et al., 2004; Mackie et al., 1988).

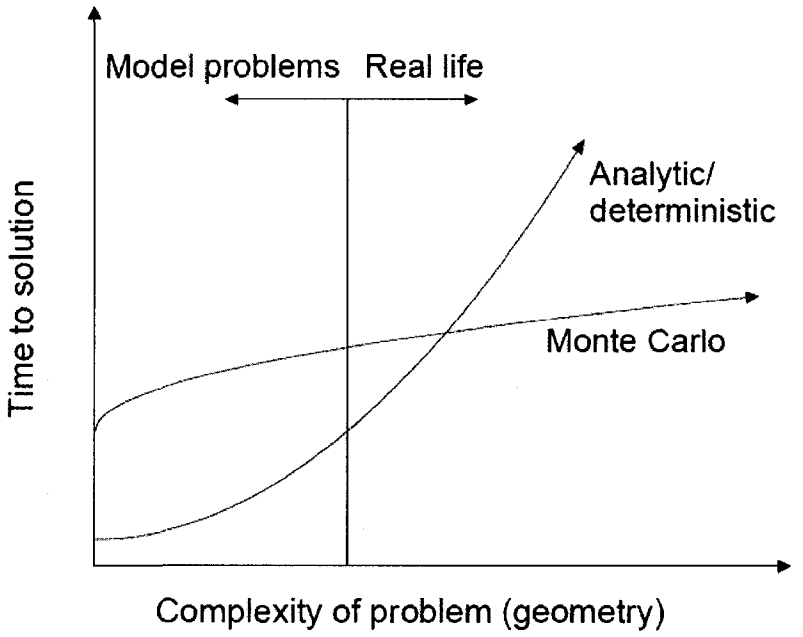

Figure 3-1. *Comparison of MC and analytic problem solution times with different complexity (Bielajew . 2001)*

3.1.2.4 Simulation advantage for complex problems

To solve a general problem, Bielajew (2001) gave a mathematical proof that analytic/deterministic methods solve the problem with time exponentially increasing with the complexity of geometric dimensions and spatial resolution, but the MC method calculation time is almost linear to the complexity of the problem. The trends are illustrated in Figure 3-1 reprinted here from his book. Therefore, MC methods can be

expected to have a time advantage in real life situations, such as radiation transport in complex geometry and multi dimensional problems, while having a time disadvantage in problems which can be modeled or simplified for analytic methods (Bielajew, 2001).

3.1.3 Issues for consideration in Monte Carlo

In radiation transport simulations, the final quantities produced such as absorbed dose or particle fluence result from an average over a large number of randomly seeded particle histories subject to the initial conditions of the problem in question. The final reported quantities are therefore subject to inherent statistical uncertainty (Sempau and Bielajew, 2000). The uncertainty decreases with increasing simulation history numbers. This statistical uncertainty leads to two related issues in MC in practical applications. The first is that the MC results should be interpreted with a statistical uncertainty or noise and this uncertainty level should ideally be made smaller than some acceptable level. The second is that more histories are needed to reduce the uncertainty to a smaller level. Because calculation time is directly proportional to the number of histories simulated, calculation time is anywhere from hours to days (Reynaert *et al.*, 2007). Hence, the calculation time becomes an issue for consideration.

3.1.3.1 MC statistical uncertainty

Sempau and Bielajew (2000) gave an estimated variation of the MC dose result:

$$\sigma^2(\bar{D}) = \frac{D}{N\Delta V}\frac{\langle \epsilon^2 \rangle}{\rho \langle \epsilon \rangle} \qquad [3-1]$$

Here, D is the dose in a voxel, ΔV is the voxel volume, ρ is the average density, N is the number of simulation histories, and $\langle \epsilon \rangle$ and $\langle \epsilon^2 \rangle$ are the average energy and

average energy squared deposited by a single particle that hits this voxel. Then, statistical uncertainty is more commonly expressed as the coefficient of variation:

$$C_v = \frac{\sigma}{D} \times 100\% = \sqrt{\frac{1}{N \cdot D \cdot \Delta V}} \sqrt{\frac{\langle \epsilon^2 \rangle}{\rho \langle \epsilon \rangle}} \qquad [3-2]$$

The statistical uncertainty is proportional to $\sqrt{1/N}$, $\sqrt{1/\Delta V}$ and $\sqrt{1/D}$ in dose calculations (Sempau and Bielajew, 2000).

To evaluate the effect of inherent statistical uncertainty on MC results, Keall et al. (2000) reported a study of uncertainty level which is clinically acceptable in a lung treatment plan. They recommended that a 2% or less statistical uncertainty at the maximum dose point should be used for evaluating a treatment plan. This uncertainty level does not significantly affect isodose lines, DVHs or biological indices (Keall et al., 2000). This criterion is widely used in MC calculations by many research groups (Gordon et al., 2007; Pawlicki and Ma, 2001; Sheikh-Bagheri et al., 2000).

3.1.3.2 Efficiency of MC codes

As mentioned above, statistical uncertainty is proportional to the square root of simulation history numbers. Ma et al. (1997) reported that to achieve a 1% statistical uncertainty in the dose distribution in a water phantom consisting of 1 cm^3 cubic voxels, about 10^4 phase-space electrons were needed for every 1 cm^2 area within the field. Typically, 10^8–10^{10} photons are needed for treatment planning dose calculation (Ma and Jiang, 1999; Verhaegen and Seuntjens, 2003). The total CPU (central processing unit) time required to simulate all the photon energy (nominal energy/linac) and electron energy (nominal energy/applicator) combinations would be hours or days using a desktop computer (Ma and Jiang, 1999; Rassiah-Szegedi et al., 2007; Verhaegen and Seuntjens,

2003). Consequently the calculation time of MC method is therefore the major drawback of the algorithm. Therefore, efficiency is another major concern of its application in radiotherapy. The efficiency has been much improved with computing hardware upgrades and MC codes developments over the years.

MC calculation efficiency ε is defined as:

$$\varepsilon = \frac{1}{\sigma^2 T} \qquad [3-3]$$

by Sheikh-Bagheri et al. (2006), where T is the CPU time for the calculation to achieve the variance σ^2. The goal in improving the efficiency is to reduce the uncertainty of a result calculated within a certain CPU time period or to reduce calculation time to achieve an acceptable variance. Research on modifying MC codes to simulate radiation transport with approximations to make the process more efficient are being intensively studied (Kawrakow, 2001; Kawrakow et al., 1996; Ma et al., 2000; Sempau et al., 2000). This efficiency improving trend was accelerated by the hardware developments predicted by Moore's law, which predicts the computer calculation power will increase exponentially based on the complexity of integrated circuits doubling roughly every two years without a cost increase. The methods used to increase the efficiency vary for different MC implementations and are introduced along with different MC codes in the following part of this chapter. On the other hand, there are several de-noising methods that have been used by different groups including: 3D wavelet threshold denoising (3D-WTD), content adaptive mean–median-hybrid (CAMH) filtering, locally adaptive Savitzky–Golay curve-fitting (LASG), anisotropic diffusion (AD) and an iterative reduction of noise (IRON). These methods were compared and reviewed by El Naqa *et al.* (2005). They found these methods can improve the mean-square-error by a factor of 2-4

for head and neck IMRT treatment plans and LASG improved the phantom calculations by a factor up to 16. 3D-WTD method performed the best in the IMRT treatment plans and it is the fastest method in calculation.

3.2 MC in external photon beam radiotherapy

Megavoltage photon beams and electron beams from linacs are two major radiation sources in modern external beam radiotherapy. 6MV photon beams are widely used in IMRT with different modalities. Extensive studies have been performed on external photon beams with the MC method for various medical accelerators.

3.2.1 MC model of Linac head

With the development of MC codes in radiotherapy, most types of current conventional clinical linac have been modeled in detail by various research groups (Lee, 1997; Petti et al., 1983; Sixel and Faddegon, 1995).

3.2.1.1 Input parameters for linac head simulations

A schematic drawing of linac components modeled in a typical Monte Carlo simulation of a clinical photon beam is shown in Figure 3-2 (Ma and Sheikh-Bagheri, 2006). This is an example of how a linac is simulated using MC methods: the geometries and compositions are based on the actual physical characteristics of the linac as supplied by the manufacturer. Information used for the simulation includes a detailed approximation of the incident electron beam spectrum and distribution, as well as every component of the linac head. A typical linac head is illustrated in Figure 3-2 with the electron beam passing through the exit window of the accelerator and then hitting the target, composed of a high atomic number material to produce a beam of bremsstrahlung

photons. This beam is restricted to a desired shape initially by the primary collimator. The beam is differentially attenuated by the conically shaped flattening filter to smooth out the relative energy fluence in the plane normal to the beam incidence (i.e. to overcome the natural bremsstrahlung distribution). Also in the field are the monitor ionization chambers and a thin Mylar field mirror. The photon beam fluence may be further modulated by collimating jaws, an MLC and/or other beam modifying devices such as physical wedges before it reaches the patient for treatment.

As mentioned above, many types of medical linacs have been simulated. Faddegon et al. simulated a commercial Siemens accelerator, and showed that the key parameters are: 1) the mean energy and focal spot size of the electron beam incident on the target; 2) the material composition and thickness profile of the target; 3) flattening filter composition and shape and 4) primary collimator geometry and composition, as well as its position relative to the target (Faddegon et al., 1999). Sheikh-Bagheri et al. (2000) showed the geometries of the jaw edges are important factors, because a 0.05 cm lateral position uncertainty of the back of the upstream jaw can change the ionization in the penumbral region by up to 8% of maximum ionization. While the composition of jaws varied from pure tungsten to a tungsten alloy, the difference is not observable and the primary transmission through the bulk of each jaw is negligible for 10 cm tungsten.

MLC leaf end shape and tongue-and-groove geometries are the key parameters in the MLC simulations. Ma C.-M. et al., (2002) has shown that for a single field sequence the underdosing due to the tongue-and-groove effect can amount to 10% to 15%.

The material compositions and geometries of components are usually obtained from the manufacturers or by direct measurement. The parameters from manufacturers are

mean specifications for batches of the same type of linacs. These parameters will deviate slightly from the mean values in any given individual unit as a result of variations in manufacturing. Validations obtained by comparing the measurement of the sensitive quantities of the linac output to MC simulations are therefore necessary. This validation will be discussed in detail in the following section. The electron beam energy, shape and size are tuned in a similar fashion to the validation procedure of geometric parameters.

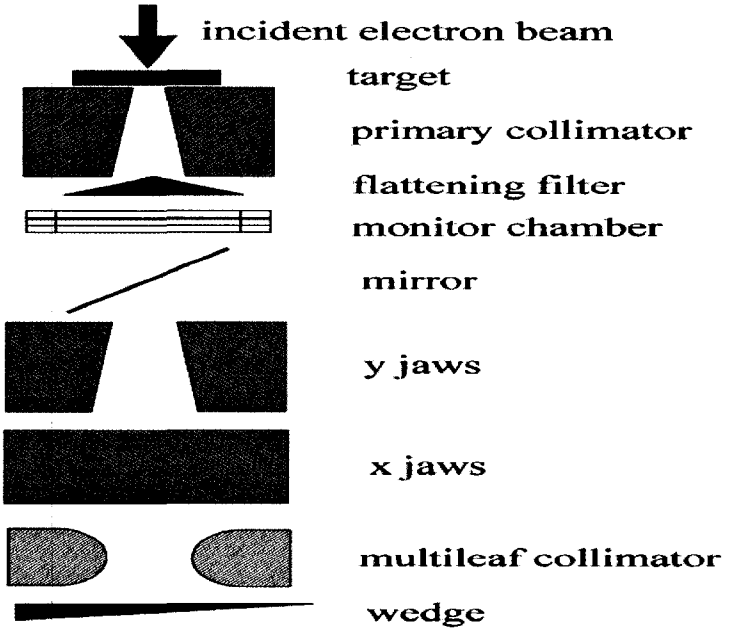

Figure 3-2 *Example schematic drawing of linac components modeled in Monte Carlo simulations of a clinical photon beam. Different linac manufacturers may have different components (Ma and Sheikh-Bagheri, 2006)*

3.2.1.2 Output information from MC simulation

From the MC linac head model simulations, computer files which record the type, position, direction, energy, charge, and weight of particles from the simulation, called phase-space files, can be obtained at one or more specified planes. The phase space file

contains information of the radiation source particles. It can subsequently be used as a source to simulate dose deposition by the linac beam in arbitrary geometry and media. Characteristics of photon and electron beams of different clinical energy and field sizes can be studied using the phase space file.

3.2.1.3 Validations of the MC model

As mentioned above, the accuracy of the linac source model need to be validated. The accuracy of these phase space files can be determined by comparing their output dose with experimental measurements. Dosimetric validations can verify the geometry and energy inputs, and validate the MC model for further dose calculations in other situations (Libby et al., 1999). Dosimetric quantities, such as percentage depth dose, are commonly used for validating the photon beam produced by the linac, and profiles in the phantom at different depths are used to verify the shape and size of the electron pencil beam incident on the target. The jaw settings and MLC geometries can also be validated by comparison of simulated profiles with measured profiles (Libby et al., 1999). The parameters should be tuned according to the differences between the simulation and the measurements. With this fine tuned and validated MC model, further dose calculations in patient or phantom can be performed.

3.2.2 MC model for patient dose calculation

Patient dose calculation can be performed with the source model mentioned above. Due to the advantages of the MC method over the non-MC methods mentioned previously, MC is an ideal tool for IMRT treatment simulation, which often involves large intensity gradients and multiple small MLC field segments.

The MC method can simulate particle transport in detailed MLC geometries and incorporate MLC tongue-and-groove effects (Webb *et al.*, 1997). Therefore, it can detect not only heterogeneity correction errors, but also the fluence approximation errors from the conventional dose calculation methods (Ma et al., 2002). Currently, MC methods are still not fast enough to do the routine calculations for inverse treatment planning in the clinic, but TPS verification, IMRT QA and patient specific plan verifications are being studied by different research groups (Ma et al., 2003; Mihaylov et al., 2007; Siebers and Mohan, 2003; Yang et al., 2005).

3.3 Monte Carlo codes

3.3.1 General Monte Carlo codes

Several general-purpose MC codes developed in the 1980's and 1990's were widely used in radiation beam modeling and dose distribution calculations. The four of the most frequently used codes in radiotherapy are EGS4/EGSnrc (Kawrakow, 2000; Nelson et al., 1985), ETRAN/ITS/MCNP (Briesmeister, 2000), PENELOPE (Sempau et al., 1997) and GEANT4 (2003). EGS4 is the earlier version of EGSnrc and MCNP uses the same electron transport algorithms as ETRAN/ITS. The algorithms used in these MC codes have been reviewed by Verhaegen and Seuntjens (2003). Both EGSnrc and PENELOPE simulate the coupled transport of photons and electrons (and positrons) only, while other particles such as neutrons or protons are not taken into account. These codes were written in the FORTRAN programming language, with the exception of GEANT4, which is written in C++ (Verhaegen and Seuntjens, 2003). Generally, the four systems use virtually identical photon transport algorithms in the energy range of radiotherapy, although different cross section data are used (Reynaert et al., 2007). The accuracy and

speed differences of these systems are due to the different electron transport algorithms. Sheikh-Bagheri et al. (2006) reviewed these codes and generalized that EGSnrc and ITS/ETRAN are roughly of the same efficiency for calculation when no efficiency improving techniques are used, whereas the other systems (PENELOPE, GEANT4, MCNP) tend to be considerably slower. Different efficiency improving techniques are used in these code systems for special-purpose applications.

3.3.2 Efficiency improving techniques

To make the MC method applicable to clinical radiotherapy, code efficiency, $\varepsilon = \frac{1}{\sigma^2 T}$ as mentioned above, is an important issue for consideration. Efficiency improving techniques in MC play an important role to reduce the calculation time to a reasonable level with clinically acceptable uncertainties. The most frequently used efficiency improving techniques are briefly introduced here.

3.3.2.1 Condensed History Technique

An electron or positron within the range of typical radiotherapy energy (~1 MeV) undergoes on the order of 10^6 elastic and inelastic collisions until it is locally absorbed in a medium (Reft *et al.* 2003). An analog simulation would be to calculate each physical interaction individully, as mentioned in the introduction (Bielajew, 2006). Such an analog simulation with 10^6 calculations for one electron or positron history would be prohibitively long for typical treatment planning calculations. The condensed history technique (CHT) is introduced to solve this problem. Because most of the electron interactions result in extremely small changes in energy and /or direction, the CHT method condenses many interactions into a single "step" that accounts for the aggregate

effects of scattering along the path of the electron. The electron-step algorithm for transport mechanics and boundary-crossing algorithms are two major approximations that influence the simulation speed and accuracy. CHT is used in every MC code system for radiation transport. Kawrakow and Bielajew (1998) gave a detailed theoretical comparison between different electron-step algorithms, and Kawrakow (2000) investigated the various details of a CHT implementation and its influence on accuracy. His CHT algorithm was adopted in the MC code of EGSnrc and it is widely used in the radiation simulations.

3.3.2.2 Range rejection and transport cutoffs

The introduction of range rejection and transport cutoffs are approximation methods that improve the simulation efficiency. In range rejection, a particle's history is terminated whenever its residual range is too low to escape from the current region or reach another region of interest. Similarly, if a particle's energy drops below a cutoff energy threshold (called PCUT or ECUT for photon and electrons, respectively), its history is stopped and the energy is considered deposited locally. The simulation time is shortened by omitting the simulation of the low energy track ends, which in most cases provide little additional information in the final analysis. By ignoring low energy particle transport, however, bremsstrahlung or annihilation photons produced by the electron/positron slowing down are omitted, but this is less of a concern as energy drops, or if effective atomic number of the medium is low. The range rejection or the cutoff energies shouldn't be too large, therefore, to keep the results accurate. Sheikh-Bagheri et al. (2000) investigated photon fluence differences for linac simulations arising from range rejection and cutoff energy in the BEAM code. A 1.5MeV electron cutoff energy for a

6MV beam will only underestimate photon fluence by 0.2%, while increasing the efficiency by a factor of about 3. The approximation is reasonable in linac simulation and patient dose calculation.

3.3.2.3 Photon Splitting and Russian Roulette

Photon Splitting and Russian Roulette are two methods used by most of the MC codes mentioned above. One particular place where these techniques offer an improvement to simulation efficiency is in the production of bremsstrahlung photons in the target of the linac head. Because of the low efficiency of the bremsstrahlung process, many electron tracks need to be simulated in order for a bremsstrahlung photon to be produced. In the splitting algorithm, for each electron bremsstrahlung interaction, a large number (N_{split}) of secondary photons with lower weights ($1/N_{split}$) are set in motion, rather than a single photon. In *directional* splitting, the splitting number can be set to depend on the angle of emission, favouring a field of interest. By employing the splitting method in this situation, one electron track can produce more bremsstrahlung photons and a large amount of time tracking electrons in the target is therefore saved (Rogers et al., 1995). Naturally, some photons not moving in the direction of interest *ie.* upward out of the linac head, are of little use to the overall goal of the simulations. Russian Roulette is used in these situations to reduce the time spent on the simulation of these photons. They are subjected to a Russian Roulette game with a survival probability $p=1/N_{split}$. The weight of the surviving secondary photon is changed back to 1 and it is simulated the same way as the primary photon, while N_{split}-1 photons are represented by this surviving photon. An efficiency improvement factor of ~500 has been reported by Kawrakow et al. (2004)

using this combination of techniques in the simulation of the output from a linac head (Kawrakow et al., 2004).

In patient geometry calculations, N_{split} photon interaction sites are sampled for each incident photon using a single pass through the geometry. The Russian Roulette is applied as described above. Kawrakow and Walters (2006) reported that an efficiency improvment factor of 5 to 6.5 can be achieved by combining photon splitting method combined with Russian Roulette in the dose calculations of 6MV and 18MV photon beams. In contrast to the range rejection and transport cutoff approximations for one history, these techniques improve the efficiency by changing the variance for a given number of histories while not biasing the result, and hence are called variance reduction techniques.

3.3.2.4 Other efficiency improving methods

There are other variance reduction and efficiency improving techniques which collectively have allowed substantial increases in the speed of a calculation. These methods include the reuse of particle tracks (history repetition) for different positions and directions with heterogeneity scaling (Kawrakow et al., 1996), or other adaptations of particle track reuse, such as the simultaneous transport of particle sets (STOPS) approach of Kawrakow (2001), which calculate material-independent quantities such as mean free paths, azimuthal scattering angles and cross sections for a set of particles with the same energy and charge but different position and directions. These methods also include algorithms allowing particle (either photon or electron/positron) transport with a long step-size without stopping at boundaries, such as Woodcock tracing for photons

(Hartmann Siantar et al., 2001; Sempau et al., 2000) and the random hinge algorithm for electrons (Sempau et al., 2000).

Kawrakow et al. (Kawrakow, 2005) and Ma et al. (2002) provide more comprehensive reviews of variance reduction and efficiency improving techniques in radiotherapy.

3.3.3 Faster Monte Carlo codes

3.3.3.1 Faster MC codes

Dose distribution calculations are the major application of interest for MC in treatment planning and patient treatment plan verification. The general purpose MC codes are considered not fast enough for routine clinical application. Faster MC codes based on the general purposes codes with different efficiency improving techniques to calculate patient dose have been and are still being intensively studied for both research and clinical applications. Among these faster codes, the most well known are Dose Planning Method (DPM) (Sempau et al., 2000), voxel Monte Carlo++ (VMC++) (Kawrakow, 2001), MCDOSE (Ma et al., 2000), Monte Carlo Vista (MCV) (Siebers et al., 2000), Monte Carlo N-particle, (MCNP) (DeMarco et al., 1998), Macro Monte Carlo (MMC) (Neuenschwander et al., 1995) and PEREGRINE (Hartmann Siantar et al., 2001). They use many of the different efficiency improving techniques or variance reduction technique as described previously. In the efficiency improving techniques, there are methods which make additional approximations to reduce the calculation time. These approximations might potentially compromise accuracy or there might be bugs in the implementation. There should therefore be a benchmark to compare these developing faster codes.

3.3.3.2 ICCR benchmark for MC engine in radiation treatment planning

To quantify the speed and accuracy of the various faster MC codes being used for research and/or clinical planning purposes, Rogers and Mohan (2000) proposed a series of benchmarks at the 2000 International Conference on the use of Computers in Radiation therapy (ICCR), to be known as the ICCR benchmark. DOSXYZ (Walters et al., 2005) with the PRESTA electron transport algorithm (Bielajew and Rogers, 1987) is based on the EGS4 system and geometrically set up for patient/phantom dose calculation on a Cartesian grid. It is used as the benchmark for comparison with all other codes, due to its accuracy and wide acceptance. The benchmarks are calculated in various phantom situations. The tests and geometries for the ICCR benchmark comparisons are as follows: (a) Speed test: phantom of dimensions $30.5\times30.5\times30$ cm^3 with $(5mm)^3$ voxels filled either randomly with one of 4 materials (water, aluminium, lung, and graphite) or with water alone, 6 MV photon spectrum from a point source at 100 cm SSD and collimated to 10×10 cm^2 at the phantom surface, (b) accuracy test: heterogeneous phantom as defined in (a) with $5\times5\times2$ mm^3 voxels (2 mm along the depth axis), 18 MV photon spectrum from a point source at 100 cm SSD and collimated to 1.5×1.5 cm^2 at the phantom surface. Statistical uncertainties were to be reported as the relative uncertainty in the dose for voxels with a dose greater than some arbitrary lower limit, such as 50% of the maximum dose.

Most of the faster MC codes have been evaluated by the ICCR benchmark. Chetty et al. (2007) summarized the comparison results in Table 3-I (reprinted here from their paper). Most of these codes have a calculation accuracy within ±1% of DOSXYZ results. VMC++, MCDOSE and RT_DPM are the top three fastest codes in this benchmark

comparison. They have calculation efficiency improvements about 6 to 50 fold greater than the DOSXYZ code.

Table 3-I. Summary of timing and accuracy results from the ICCR benchmark (Chetty et al., 2007).

Monte Carlo code	Time estimate (minutes)	% max. diff. relative to ESG4/PRESTA/DOSXYZ
ESG4/PRESTA/DOSXYZ	42.9	0, benchmark calculation
VMC++	0.9	± 1
MCDOSE (modified ESG4/PRESTA)	1.6	± 1
MCV (modified ESG4/PRESTA)	21.8	± 1
RT_DPM (modified DPM)	7.3	± 1
MCNPX	60.0	max. diff. of 8% at Al/lung interface (on average ± 1% agreement)
Nomos (PEREGRINE)	43.3*	± 1*
GEANT 4 (4.6.1)	193.3**	± 1 for homogeneous water and water/air interfaces**

*Note that the timing for the PEREGRINE code also includes the sampling from a correlated-histogram source model and transport through the field-defining collimators.

3.3.4 Monte Carlo codes used in this project

BEAMnrc (Rogers et al., 1995) and DOSXYZnrc (Walters et al., 2005) are codes optimized for specific applications and based on the EGSnrc system. BEAMnrc and DOSXYZnrc are optimized for detailed radiotherapy accelerator modeling and voxelized dose deposition calculations, respectively. These two code systems are used in this project to study the helical tomotherapy unit. There are three major advantages of these systems. Firstly, BEAMnrc provides different possible geometries, called component modules, which correspond to the geometries of items typically found in medical linear

accelerators such as a target, monitor chamber, jaws, MLC and so on. This function of supplying component modules is to simplify the modeling of accelerator geometries. Moreover, DOSXYZnrc can use different sources including the phase-space files from BEAMnrc simulations to perform absorbed dose calculations within a Cartesian volume with voxels representing different materials of interest; this arbitrary voxelized calculation space is sometimes termed a 'phantom'. Each of the voxels in the phantom has a material and density specified by the user or converted from a CT data set. Both systems are based on the EGSnrc MC code which has the ability to simulate photon and electron transport with energies ranging from 10 keV to 50 MeV in a wide variety of media (Kawrakow and Rogers, 2000). The second major advantage is that the BEAMnrc/DOSXYZnrc systems are based on the optimized EGSnrc code, which is considered a robust MC code in radiotherapy simulation. The EGSnrc code system has been extensively used and benchmarked against experimental measurements. Some major benchmarking results were listed on the website of Ionizing Radiation Standards Group (IRS) of the National Research Council of Canada (NRCC, http://www.irs.inms.nrc.ca/papers/irs_www/irs_www.html). Any potential defects of the algorithms used in this systems are usually spotted and corrected quickly by the authors or other researchers (Walters and Kawrakow, 2007). The system is also used to benchmark other MC codes while evaluating their accuracies and efficiencies (Chetty et al., 2007). We can use this model as a benchmark for further clinical application. The third and final major advantage we mention here is that the code system is free and easily obtained from IRS on the NRCC website (NRCC http://www.irs.inms.nrc.ca/irs.html) and it is well supported with a large group of users.

Bibliography:

Attix, F. H. (1986): *Introduction to radiological physics and radiation dosimetry*. Wiley. New York.

Bielajew, A. F. (2001): Monte Carlo and Numerical Quadrature. In A. F. Bielajew (Ed.): *Fundamentals of the Monte Carlo method for neutral and charged particle transport*, The University of Michigan.

Bielajew, A. F. (2006): The Monte Carlo Simulation of Radiation Transport: *AAPM 2006 Summer school.*

Bielajew, A. F., and Rogers, D. W. O. (1987): PRESTA: The parameter reduced electron-step transport algorithm for electron Monte Carlo transport. *Nucl Instrum Methods Phys Res B* **18**, 165-81.

Briesmeister, J. F. (2000): MCNP-A general Monte Carlo N-particle transport code, Version 4C. Technical Report No. LA-13709-M.

Chetty, I. J., Curran, B., Cygler, J. E., Ezzell, J. J. D. G., Faddegon, B. A., Kawrakow, I., Keall, P. J., Liu, H., Ma, C.-M. C., Rogers, D. W. O., Seuntjens, J., Sheikh-Bagheri, D., and Siebers, J. V. (2007): Report of the AAPM Task Group No. 105: Issues associated with clinical implementation of Monte Carlo-based photon and electron external beam treatment planning. *Med. Phys.* **34**, 4818-4853.

DeMarco, J. J., Solberg, T. D., and Smathers, J. B. (1998): A CT-based Monte Carlo simulation tool for dosimetry planning and analysis. *Med. Phys.* **25**, 1–11

El Naqa, I., Kawrakow, I., Fippel, M., Siebers, J. V., Lindsay, P. E., Wickerhauser, M. V., Vicic, M., Zakarian, K., Kauffmann, N., and Deasy, J. O. (2005): A comparison of Monte Carlo dose calculation denoising techniques. *Phys Med Biol* **50**, 909-22.

Faddegon, B. A., O'Brien, P., and Mason, D. L. (1999): The flatness of Siemens linear accelerator x-ray fields. *Med. Phys.* **26**, 220–228.

GEANT4 (2003): http://geant4.web.cern.ch/geant4/.

Gordon, J. J., Crimaldi, A. J., Hagan, M., Moore, J., and Siebers, J. V. (2007): Evaluation of clinical margins via simulation of patient setup errors in prostate IMRT treatment plans. *Med Phys* **34**, 202-14.

Hartmann Siantar, C. L., Walling, R. S., Daly, T. P., Faddegon, B., Albright, N., Bergstrom, P., Bielajew, A. F., Chiang, C., Garnet, D., House, R. K., Knapp, D., Wieczorek, D. J., and Verhey, L. J. (2001): Description and dosimetric verification of the PEREGRINE Monte

Carlo dose calculation system for photon beams incident on a water phantom. *Med. Phys.* **28**, 1322-37.

Jeraj, R., Mackie, T. R., Balog, J., Olivera, G., Pearson, D., Kapatoes, J., Ruchala, K., and Reckwerdt, P. (2004): Radiation characteristics of helical tomotherapy. *Med. Phys.* **31**, 396-403.

Johns, H. E., and Cunningham, J. R. (1983): *The physics of radiology*. Charles C. Thomas. Springfield, Ill., U.S.A.

Kawrakow, I. (2000): Accurate condensed history Monte Carlo simulation of electron transport I. EGSnrc, the new EGS4 version. *Med. Phys.* **27**, 485-98.

Kawrakow, I. (2001): VMC++ , electron and photon Monte Carlo calculations optimized for radiation treatment planning in "Advanced Monte Carlo for Radiation Physics, Particle Transport Simulation and Applications", pp. 229–236. In F. B. A. Kling, M. Nakagawa, L. Tavora, and P. Vaz (Ed.): *Proceedings of the Monte Carlo 2000 Meeting Lisbon*, Springer, Berlin.

Kawrakow, I. (2005): On the efficiency of photon beam treatment head simulations. *Med. Phys.* **32**, 2320-26.

Kawrakow, I., and Bielajew, A. F. (1998): On the condensed history technique for electron transport. *Nucl Instrum Methods Phys Res B* **142**, 253-80.

Kawrakow, I., Fippel, M., and Friedrich, K. (1996): 3D electron dose calculation using a Voxel based Monte Carlo algorithm (VMC). *Med. Phys.* **23**, 445-57.

Kawrakow, I., and Rogers, D. W. O. (2000): The EGSnrc Code System: Monte Carlo simulation of electron and photon transport. *NRCC Report*.

Kawrakow, I., Rogers, D. W. O., and Walters, B. (2004): Large efficiency improvements in BEAMnrc using directional Bremsstrahlung splitting. *Med. Phys.* **31**, 2883-98

Kawrakow, I., and Walters, B. R. B. (2006): Efficient photon beam dose calculations using DOSXYZnrc with BEAMnrc. *Med. Phys.* **33**, 3046-56.

Keall, P. J., Siebers, J. V., Jeraj, R., and Mohan, R. (2000): The effect of dose calculation uncertainty on the evaluation of radiotherapy plans. *Med Phys* **27**, 478-84.

Kirkby, C., Stanescu, T., Rathee, S., Carlone, M., Murray, B., and Fallone, B. G. (2008): Patient dosimetry for hybrid MRI-radiotherapy systems. *Med. Phys.* **35**, 1019-27.

Lee, P. C. (1997): Monte Carlo simulations of the differential beam hardening effect of a flattening filter on a therapeutic x-ray beam. *Med. Phys.* **24**, 1485-89.

Libby, B., Siebers, J., and Mohan, R. (1999): Validation of Monte Carlo generated phase-space descriptions of medical linear accelerators. *Med. Phys.* **26**, 1476-83.

Ma, C.-M., Faddegon, B. A., Rogers, D. W., and Mackie, T. R. (1997): Accurate characterization of Monte Carlo calculated electron beams for radiotherapy. *Med. Phys.* **24**, 401-16.

Ma, C.-M., and Jiang, S. B. (1999): Monte Carlo modelling of electron beams from medical accelerators. *Phys. Med. Biol.* **44**, R157-89.

Ma, C.-M., Jiang, S. B., Pawlicki, T., Chen, Y., Li, J. S., Deng, J., and Boyer, A. L. (2003): A quality assurance phantom for IMRT dose verification. *Phys. Med. Biol.* **48**, 561-72.

Ma, C.-M., Li, J. S., Pawlicki, T., Jiang, S. B., and Deng, J. (2000): MCDOSE-A Monte Carlo dose calculation tool for radiation therapy treatment planning, pp. 411-13. In T. B. a. W. Schlegel (Ed.): *Proceedings of the 13th ICCR*, Springer-Verlag,, Heidelberg.

Ma, C.-M., Li, J. S., Pawlicki, T., Jiang, S. B., Deng, J., Lee, M. C., Koumrian, T., Luxton, M., and Brain, S. (2002): A Monte Carlo dose calculation tool for radiotherapy treatment planning. *Phys. Med. Biol.* **47**, 1671-89.

Ma, C.-M. C., and Sheikh-Bagheri, D. (2006): Monte Carlo Methods for Accelerator Simulation and Photon Beam Modeling: *AAPM 2006 Summer school.*

Mackie, T., A., Bielajew, A. F., Rogers, D. W. O., and Battista, J. J. (1988): Generation of photon energy deposition kernels using the EGS Monte Carlo code. *Phys. Med. Biol.* **33**, 1-20.

Mihaylov, I. B., Lerma, F. A., Fatyga, M., and Siebers, J. V. (2007): Quantification of the impact of MLC modeling and tissue heterogeneities on dynamic IMRT dose calculations. *Med. Phys.* **34**, 1244-52.

Mohan, R. (1997): Why Monte Carlo?, pp. 16-8. In D. D. Leavitt, and G. Starkschall (Eds): *In Proceeding XII International Conference on the Use of Computers in Radiation Therapy*, Medical Phsyics Publishing Madison,WI.

Nelson, W. R., Hirayama, H., and Rogers, D. W. O. (1985): The EGS4 code system, Report SLAC-265: *Stanford Linear Accelerator*, Stanford, CA.

Neuenschwander, H., Mackie, T. R., and Reckwerdt, P. J. (1995): MMC-A high performance Monte Carlo code for electron beam treatment planning. *Phys. Med. Biol.* **40**, 543-74.

NRCC http://www.irs.inms.nrc.ca/irs.html.

Pawlicki, T., and Ma, C. M. (2001): Monte Carlo simulation for MLC-based intensity-modulated radiotherapy. *Med Dosim* **26**, 157-68.

Petti, P. L., Goodman, M. S., Babriel, T. A., and Mohan., R. (1983): Investigation of buildup dose from electron contamination of clinical photon beams. *Med. Phys.* **10**, 18-24

Rassiah-Szegedi, P., Fuss, M., Sheikh-Bagheri, D., Szegedi, M., Stathakis, S., Lancaster, J., Papanikolaou, N., and Salter, B. (2007): Dosimetric evaluation of a Monte Carlo IMRT treatment planning system incorporating the MIMiC. *Phys Med Biol* **52**, 6931-41.

Reft, C., Alecu, R., Das, I. J., Gerbi, B. J., Keall, P., Lief, E., Mijnheer, B. J., Papanikolaou, N., Sibata, C., and Van Dyk, J. (2003): Dosimetric considerations for patients with HIP prostheses undergoing pelvic irradiation. Report of the AAPM Radiation Therapy Committee Task Group 63. *Med Phys* **30**, 1162-82.

Reynaert, N., Marck, v. d., Schaart, W., Zee, V. d., Vliet-Vroegindeweij, C. V., Tomsej, M., Jansen, J., Heijmen, B., Coghe, M., and Wagter, C. D. (2007): Monte Carlo treatment planning for photon and electron beams. *Radiation Physics and Chemistry* **76**, 643–686.

Rogers, D. W. O., Faddegon, B. A., Ding, G. X., Ma, C.-M., Wei, J., and Mackie, T. R. (1995): BEAM: A Monte Carlo code to simulate radiotherapy treatment units. *Med. Phys.* **22**, 503-24.

Rogers, D. W. O., and Mohan, R. (2000): Questions for comparisons of clinical Monte Carlo codes. the 13th ICCR, pp. 120-22.

Sempau, J., Acosta, E., Baro, J., Fernandez-Varea, J. M., and Salvat, F. (1997): An algorithm for Monte Carlo simulation of coupled electron–photon transport. *Nucl. Instrum. Methods B* **132**, 377-90.

Sempau, J., and Bielajew, A. F. (2000): Towards the elimination of Monte Carlo statistical fluctuations from dose volume histograms for radiotherapy treatment planning. *Phys. Med. Biol.* **45**, 131-57.

Sempau, J., Wilderman, S. J., and Bielajew, A. F. (2000): DPM, a fast, accurate Monte Carlo code optimized for photon and electron radiotherapy treatment planning dose calculations. *Phys. Med. Biol.* **45**, 2263-91.

Sheikh-Bagheri, D., Kawrakow, I., Walters, B., and Rogers, D. W. O. (2006): Monte Carlo simulations: efficiency improvement techniques and statistical considerations: *AAPM 2006 Summer school.*

Sheikh-Bagheri, D., Rogers, D. W. O., Ross, C. K., and Seuntjens, J. P. (2000): Comparison of measured and Monte Carlo calculated dose distributions from the NRC linac. *Med. Phys.* **27**, 2256-66.

Siebers, J., and Mohan, R. (2003): Monte Carlo and IMRT, pp. 531-60. In T. R. Mackie, and J. R. Palta (Eds): *Intensity-Modulated Radiation Therapy: The State of the Art*, Medical Physics Publishing, Madison, WI.

Siebers, J. V., Keall, P. J., and Kawrakow, I. (2005): Monte Carlo dose calculations for external beam radiation therapy. In J. Van Dyk (Ed.): *The modern technology of radiation oncology*, Medical Physics Publishing, Madison,WI.

Siebers, J. V., Keall, P. J., Kim, J., and Mohan, R. (2000): Performance benchmarks of the MCV Monte Carlo System. the 13th ICCR, pp. 129-31.

Sixel, K. E., and Faddegon, B. A. (1995): Calculation of x-ray spectra for radiosurgical beams. *Med. Phys.* **22**, 1657-61.

Van Esch, A., Tillikainen, L., Pyykkonen, J., Tenhunen, M., Helminen, H., Siljamäki, S., Alakuijala, J., Paiusco, M., Iori, M., and Huyskens, D. P. (2006): Testing of the analytical anisotropic algorithm for photon dose calculation. *Med. Phys.* **33**, 4130-48.

Verhaegen, F., and Seuntjens, J. (2003): Monte Carlo modeling of external radiotherapy photon beams. *Phys. Med. Biol.* **48**, R107-R164.

Walters, B. R. B., and Kawrakow, I. (2007): Overprediction of dose with default PRESTA-I boundary crossing in DOSXYZnrc and BEAMnrc. *Med. Phys.* **34**, 647-50.

Walters, B. R. B., Kawrakow, I., and Rogers, D. W. O. (2005): DOSXYZnrc Users Manual, NRC Report PIRS 794(rev. B).

Webb, S., Bortfeld, T., Stein, J., and Convery, D. (1997): The effect of stair-step leaf transmission on the 'tongue-and-groove problem' in dynamic radiotherapy with a multileaf collimator. *Phys Med Biol* **42**, 595-602.

Yang, J., Li, J., Chen, L., Price, R., McNeeley, S., Qin, L., Wang, L., Xiong, W., and Ma, C.-M. (2005): Dosimetric verification of IMRT treatment planning using Monte Carlo simulations for prostate cancer. *Phys. Med. Biol.* **50**, 869-78.

Chapter 4 : Monte Carlo calculation of helical tomotherapy dose delivery

4.1 Introduction

Helical tomotherapy is an external radiotherapy unit that delivers intensity modulated radiation therapy (IMRT) (Mackie, 2006; Mackie et al., 1993). Helical tomotherapy uses an intensity modulated, narrow photon fan beam that moves in a helical pattern to deliver a conformal radiation dose distribution to a planning target volume (PTV) while avoiding nearby organs at risk (OAR). Its unique design makes helical tomotherapy capable of delivering complex modulated coplanar beam arrangements from more angles than typically found in conventional linac IMRT. This approach allows for increased homogeneity of the dose distribution within a PTV and the same or better normal tissue sparing compared to conventional three dimensional conformal radiotherapy (3D-CRT) and some linac IMRT deliveries (Han et al., 2007; Kron et al., 2004; Zeidan et al., 2007).

Like other IMRT systems, the accurate calculation of the dose distribution in the patient by the treatment planning system (TPS) is necessary for an effective patient treatment. Helical tomotherapy TPS uses a relatively accurate convolution/superposition algorithm for the dose calculation (McNutt et al., 1997), and as with other non-Monte Carlo (MC) algorithms, charged particle equilibrium (CPE) is assumed in the dose calculation. We can reasonably expect the TPS will have difficulties in predicting the dose in certain situations, such as with significant inhomogeneities in the patient geometry where this assumption is not satisfied. These situations are encountered in the

build-up regions behind air cavities such as those found in a head and neck or a lung treatment (Davidson et al., 2007; Jones and Das, 2005; Vanderstraeten et al., 2006) MC dose calculations can be used to validate the TPS predicted dose in such cases(Vanderstraeten et al., 2006). As well, the dose in and around inhomogeneities of high atomic number (Z) is not likely to be well modeled by a convolution/superposition algorithm and MC is considered to be well suited to this application (Reft et al., 2003).

In a routine delivery quality assurance (DQA), the TPS predicted dose is verified against measurements in a solid water phantom (called the 'Cheese Phantom') (Thomas et al., 2005a), which, because of its homogeneous construction, does not necessarily validate the patient dose (Vanderstraeten et al., 2006). Moreover, the verification with the standard DQA phantom may only be performed at, at most, a few points with ion chambers and one plane with a film measurement per DQA procedure, rather than the whole irradiated volume.

In general, a method for performing MC dose calculations in the patient geometry is desirable for several reasons: 1) it provides a more accurate method to calculate the dose distribution of a helical tomotherapy treatment, 2) it would provide, in addition to the film and ion chamber dosimetry, further validation for the complex treatments delivered by the helical tomotherapy unit, 3) it would allow the validation of the performance of the helical tomotherapy treatment planning software on a 3D, point-by-point basis, and 4) it would allow for the simulation and investigation of the dosimetric consequences of new delivery techniques with helical tomotherapy before they are enabled (e.g. running start with the jaws). The calculation of MC doses for the helical tomotherapy system is made far more complicated than for 3D-CRT or even 'conventional' multi field IMRT by the

potentially very large number of beam directions and leaf opening configurations for the complex modulated fields employed in the delivery; the number of 'beamlets' may be well into the tens of thousands. We report here on the development of a method for performing explicit MC simulation of helical tomotherapy deliveries, without the need to resort to approximations for the tongue and groove effect or the need to render the net leaf openings into an approximate effect single field. Although these approximations are not issues causing large calculation error, this approximation-free method can be used as a good benchmarking method to validate the TPS calculation.

4.2 Methods and materials

4.2.1 The helical tomotherapy unit

A helical tomotherapy unit Hi-ART II schematic diagram is shown in Figure 4-1 with the major parts labeled. The waveguide, collimators and Multileaf Collimator (MLC) are mounted on a CT scanner like gantry, which allows them to operate as they continuously rotate around the central axis of the bore, while a patient travels along a perpendicular axis.

4.2.1.1 Photon beam source

A nominal 6MV photon beam produced by the linac is delivered to a patient with Source to Axis Distance (SAD) of 85 cm on the helical tomotherapy unit, which is different from conventional linacs which typically use SAD=100 cm. The radiation source has two characteristics different from conventional linacs. The first is the absence of a flattening filter. The second is the fan shape of the radiation field, which has a narrow variable dimension (in plane; the couch motion direction) from 0.5 cm up to 5 cm. The fan beam width is defined by the secondary jaws, while the maximum lateral

dimension (cross plane) of 40 cm is defined by the MLC leaves. All the dimensions here are defined at the isocenter plane (Mackie, 2006).

4.2.1.2 Beam intensity modulation

The helical tomotherapy MLC is operated in a binary fashion, with each of its 64 leaves either open or closed to modulate the beam. Each leaf is controlled separately and is moved very quickly, by a pneumatic system, in and out of the beam with a typical transition time under 20 ms. The MLC leaves modulate a beamlet with an average width of 6.25 mm at a given gantry angle and for a given amount of time, according to the computer optimized treatment plan. The MLC leaves are 10 cm thick tungsten with a tongue and grove structure that keeps the interleaf leakage to about 0.43% (Balog et al., 2005) and the intraleaf leakage to 0.05% (Balog et al., 1999).

4.2.1.3 Helical dose delivery

Helical tomotherapy dose delivery is performed in a manner that is somewhat analogous to helical CT scanning. During a treatment procedure, the fan beam source is rotating with a fixed period between 15 and 60 seconds while the couch is concurrently moving at a fixed speed through the gantry. The distance the couch moves per rotation is defined by a treatment plan parameter, *pitch*. The same as helical CT, the *pitch* is defined as the ratio of the distance of couch translation in one rotation relative to the radiation field width (T_{slice}) at the isocenter. The modulated beams irradiate from multiple angles during rotations and form a helical trajectory covering the patient target region in three dimensions.

While the helical tomotherapy unit typically delivers radiation continuously over a full rotation, for the purpose of treatment planning calculations, the helical tomotherapy

TPS approximates each rotation as 51 equally spaced and discrete gantry angles. Each beam is modeled as being delivered at one of these discrete gantry angles. Analogously with CT scanning, we call a beam delivered from one of these discrete angles a projection. The MLC configurations are optimized through inverse planning for different projections to give a conformal dose to the targets after multiple rotations, consisting of 51 projections per rotation and hundreds to thousands of projections in total. In the actual delivery, the helical tomotherapy source irradiates continuously with an arc motion through the helical trajectory.

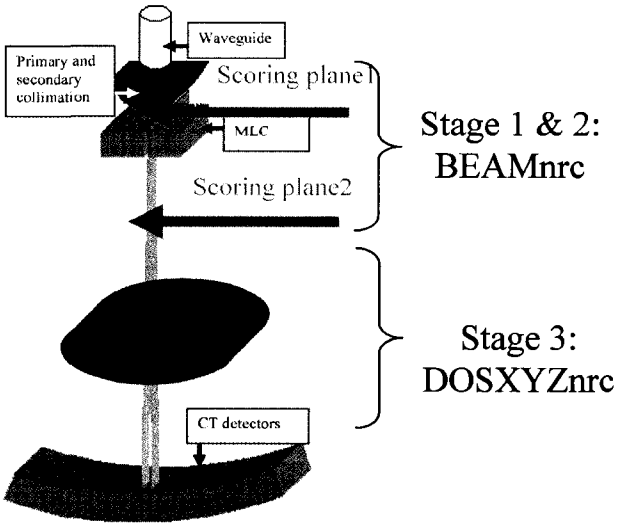

Figure 4-1. *Schematic diagram of helical tomotherapy unit. Major parts including the radiation source, the primary and secondary collimators and MLC are simulated in the full MC model. The CT detectors are not included in the simulation. Beam production and modulation are both simulated with BEAMnrc. The 'production' phase space plane is generated once for each of the possible jaw settings and scored above the MLC, and the modulated fields are simulated and summed into a phase space plane below the MLC. Dose calculation is performed in the third stage, using DOSXYZnrc.*

4.2.2 Monte Carlo model of helical tomotherapy

We used the BEAMnrc/DOSXYZnrc (Rogers et al., 1995; Walters et al., 2005) MC codes for the source modeling and the dose calculation. Our schematic model of the helical tomotherapy unit is shown in Figure 4-1. Three separate stages were used to model the helical tomotherapy system. The first was a full MC model of the helical tomotherapy source along with the primary collimator and collimating jaws. The second was the beam modulation by the MLC. Both the first and second stages were simulated using BEAMnrc. Output from this second stage was stored as a series of phase space files. The third stage used DOSXYZnrc to calculate the dose delivered to the patient geometry or phantom model using the output from stage 2 as a source. For this work the MC calculations were performed on a Linux cluster with 18 AMD Opteron64 CPUs operating at 2.0 GHz (AMD, Sunnyvale, CA) and managed by ROCKSv3.3 (Rocks Cluster Group, San Diego Supercomputer Center, UC San Diego, USA).

4.2.2.1 Helical tomotherapy photon source and MLC simulation

Each of the two BEAMnrc stages generated its own phase space scoring plane. The first scoring plane was located immediately above the MLC, where we generated Phase-Space-File 1 (PSF1). The second scoring plane (which scored Phase-Space-File 2 (PSF2)) was located below the MLC and outside the boundary of the dose scoring phantom. The total distance to the second scoring plane from the MLC depends on the dimensions of the DOSXYZnrc calculation volume. The distance will be 85 - (calculation dimension / 2) in cm, since the delivery isocenter will be in the middle of the calculation space and the isocenter is 85 cm from the source.

The simulation is broken up in this manner because the components above the MLC remain fixed throughout treatment for any patient or phantom and therefore need only be scored once, while the MLC's dynamic modulation of the beam over different projections demands PSF2 be generated hundreds to thousands of times according to the given MLC configuration. The two-plane model saved significant computation time at the first scoring plane. The typical jaw settings in patient treatments are T_{slice} =2.5 cm or T_{slice} =5.0 cm. We simulated them individually and generated PSF1 with 10^8 particles for each jaw setting. Specific material and geometry input parameters incorporated into our model were defined according to information provided by TomoTherapy Inc. The helical tomotherapy source MC simulation without MLC modulation was studied previously and verified by our group (Thomas et al., 2005b). This source model was verified in this previous work by comparing simulated and measured Percent Depth Dose (PDD) in a water tank and profiles simulated and measured in a solid water phantom for 5.0×40.0 and 5.0×10.0 cm^2 fields.

The MLC was simulated with the BEAMnrc component module (CM), VARMLC. The parameters were taken mostly from data supplied by TomoTherapy Inc. and partly from a published helical tomotherapy prototype MLC design (Balog et al., 1999). The MLC leaves were modeled as 10 cm of tungsten (height in the beam direction), with the thickness of each leaf forming a beamlet average 0.625 cm at the isocenter plane. The tongue and groove (T&G) width and overlap width, as well as the source to MLC distance are taken from published values and supplied data, respectively. The binary MLC end is shielded under the primary and the secondary jaws and the opening and closing time is considered negligible. Therefore, the shape of the end of the MLC should

not affect the simulation of modulation. We arbitrarily assigned the leaf end a 10 cm diameter round shape.

The MLC configuration changes for different *projections*. In the second scoring plane of our model, we simulated each *projection* separately and archived a PSF2 for that projection. Each PSF2 then acted as a source for the third stage of the simulations.

When and where an MLC is opened and how long it remains open is controlled by a file which we shall call the sinogram file. This file contains an array which takes its *projection* number and MLC number as two coordinates with the array values containing the relative opening time of the MLC at that *projection*. This 2-D array is called a leaf control *sinogram*. To simulate the dynamic modulation of the helical tomotherapy MLC during each projection we used the Static-Component-Simulation (SCS) method (Liu et al., 2001) with the BEAMnrc code. In this method, each *projection* is decomposed into several static components of MLC openings (each called a *configuration*). In each component the MLC configuration is fixed and each leaf is either open or closed for the same period of time. Unlike a conventional IMRT linac, the helical tomotherapy unit delivers its radiation with an unservoed but relatively constant dose rate in its treatment mode. The dose delivery is controlled by the beam on time, which is calculated using a known machine dose rate which is established at the time of machine commissioning. The beam on time rather than the cumulative Monitor Units (MU) controls the beamlet weights and the MLC leaf beam on time is not a function of changing dose rates. As well, since the MU chambers are used only to monitor beam intensity and create an interlock in the event of loss of beam, but do not affect delivery time, any slight variation in the back scattering dose from different configurations of the jaws and MLC to the monitor ion

chambers as may be seen with conventional IMRT linacs would not impact delivery for a helical tomotherapy unit. Therefore, each *configuration* can be simulated by BEAMnrc with the number of histories proportional to the leaf opening time. Finally, one *projection* can be simulated by adding up all of the PSF2s for each *configuration* that makes it up. This method can be compared to the segmental MLC method (Liu et al., 2001), in which, a beam intensity map is formed by several MU weighted static segmental fields.

An in-house program written for Matlab (version R2006a, the MathWorks Inc., Natick, MA) reads the sinogram file of a treatment plan and automatically writes BEAMnrc input files for MC simulation and controls the MC calculation process as well.

4.2.2.2 Helical tomotherapy dose calculation with DOSXYZnrc

For dose calculation in phantoms with PSF2 files as sources, simple geometry phantoms were manually created in DOSXYZnrc by specifying grid dimensions, materials and densities. All simulations were performed with the electron cutoff energy ECUT = 0.7 MeV and photon cutoff energy PCUT = 0.01 MeV. To shorten the simulation time, the surround padding method (Walters et al., 2005) and variance reduction techniques such as range rejection with electron cutoff energy ESAVE=1.5 MeV and 10× photon splitting were used. These values are generally conservative and any deviations they may introduce should be less than the overall statistical uncertainty reported.

Patients and phantoms with complex geometry were modeled by converting CT data to 3D phantoms with voxels having a material and a density converted from the CT number. The TomoTherapy TPS CT data format is not supported by the CTcreate tool in DOSXYZnrc. Moreover, for a treatment planning dose calculation, the diagnostic CT

couch needed to be replaced by the pre-saved helical tomotherapy couch images to perform the calculation in the real helical tomotherapy dose delivery situations. Therefore, we wrote an in-house program with Matlab to convert the TPS CT data set to a DOSXYZnrc CT phantom file. In converting CT data to a DOSXYZnrc phantom, a ramp table with materials, densities and their calibrated CT numbers for our CT scanner was used. Our in-house code assigned material and density information for each voxel based on measured CT values for calibration plugs of known density, and using linear interpolation.

In the DOSXYZnrc coordinate system, the PSF2 source geometry is shown in Figure 4-2. The beam's central axis passes through the isocenter at (X_{iso}, Y_{iso}, Z_{iso}). At the isocenter (Iso.), a polar coordinate system is used to define the beam position. An azimuthal angle of beam incidence, φ, and the polar angle, θ, define the beam incidence direction. The phase space file plane to the isocenter distance is specified as well as the collimator angle φ_{col}.

Helical tomotherapy employs an IEC 61217 coordinate system (TomoTherapy-Inc., 2005). In this coordinate system, the Y_{IEC}-axis points towards the gantry, the X_{IEC}-axis points to the right when facing the gantry, and the Z_{IEC}-axis points upwards. In our model, the DOSXYZnrc coordinate system is oriented as in Figure 4-2 relative to the IEC 61217 coordinate system, in which, the X-axis is in the same direction as X_{IEC} and Y-axis is the same as Z_{IEC} and the Z-axis is the same as $-Y_{IEC}$. The CT phantom is constructed using the DOSXYZnrc coordinates with slice numbers increasing in the +Z direction. If the patient CT is acquired in a supine orientation with the head in first, the patient left hand is

in the +X direction and looks up in the +Y direction, and the +Z direction is from the patient's head to the feet.

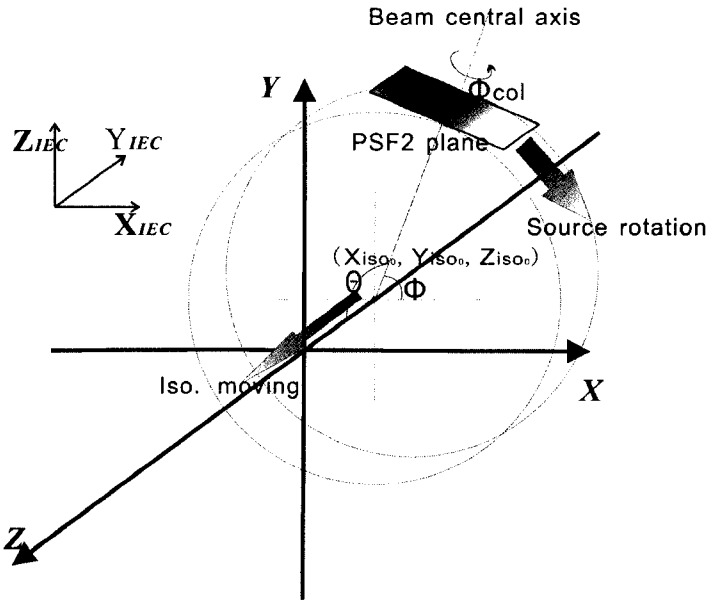

Figure 4-2. *A schematic view of the helical tomotherapy dose delivery simulation using the DOSXYZnrc coordinate system. PSF2 is used as the source in the DOSXYZnrc calculation in which incident isocenter (X_{iso}, Y_{iso}, Z_{iso}), angles θ and Φ, distance from PSF to the isocenter and the collimator angle Φ_{col} are used to specify the geometry for a given projection. The helical dose delivery is simulated by varying the Z_{iso} and the angle Φ between each projection.*

In our simulations θ is 90° for all projections, which are restricted to the source rotating in the X-Y plane (the CT transverse plane). The patient/phantom translation along the Z direction is simulated by the isocenter moving along the Z direction and the Z_{iso} is described as Equation 1. The source rotation with the gantry is determined by the angle φ. The relationship of φ with the *projection* number, N_{proj} is shown in Equation 2(a,b). Here, T_{slice}, the field width, and *pitch* are defined as previously. The Z_{iso0} is the Z coordinate of the first *projection* isocenter. Because helical tomotherapy always starts the

first *projection* at the couch position where the first slice of CT scanning started, the Z_{iso0} is always the first slice position. The expression mod(N_{proj}-1, 51) is a modulus function used to determine the *projection* position in the rotation, the value of the mod function being an integer between 0 and 50. The helical tomotherapy TPS sets the CT phantom center at X_{iso}=0, Y_{iso}=0, which corresponds to the radiation isocenter. Then, the PSF2 planes are specified with a constant distance from the isocenter resulting in a consistent SAD = 85 cm. The collimator angle is 0° for all projections.

$$Ziso = Ziso_0 + \left(\frac{N_{proj}-1}{51}\right)\times pitch\times T_{slice} \qquad [4\text{-}1]$$

$$\varphi = 270° - \left(\frac{\mathrm{mod}((N_{proj}-1),51)}{51}\right)\times 360° \quad \text{if } 0 \le \left(\frac{\mathrm{mod}((N_{proj}-1,51)}{51}\right) \le \frac{3}{4} \qquad [4-2a]$$

(2a)

$$\varphi = 270° - \left(\frac{\mathrm{mod}((N_{proj}-1,51)}{51} - 1\right)\times 360° \quad \text{if } \frac{3}{4} < \left(\frac{\mathrm{mod}((N_{proj}-1,51)}{51}\right) \qquad [4-2b]$$

4.2.3 Measurements for the MC model validation and commissioning

All measurement validations were performed on the TomoTherapy Hi-Art II system (Tomotherapy Inc., Madison, WI). To commission our model, we measured a series of characteristic beams with T_{slice} =2.5 cm and T_{slice} =5.0 cm field widths using a calibration procedure and the treatment beam. All calibrated dose measurements in this work were taken with an Exradin A1SL ion chamber (Standard Imaging, Middleton, WI). The A1SL ion chamber has a 4.05 mm inner diameter and a 4.4 mm cavity length with an active volume of 0.056 cm^3. This small volume ion chamber can minimize the volume averaging effect in large dose gradient regions for the PDD and profile measurements. Its thin wall thickness, small volume and waterproof design make it suitable for point dose

measurements in most of our validation and commissioning tasks in a water tank or solid water phantoms. Dose distribution measurements were performed with Kodak EDR2 Ready Pack film (Eastman Kodak Company, Rochester, NY). The EDR2 film was scanned with a VIDAR VXR film digitizer (VIDAR Systems Corporation, Herndon, VA) which was studied and calibrated as per a published method (Thomas et al., 2005a) and is routinely used for clinical QA tests. The film calibration curve was constructed using an MLC step previously calibrated with an ion chamber. Fourteen data points were used to define the H&D curve with doses between 0 and 387 cGy (Thomas et al., 2005a).

PDD curves for 2.5×40.0 cm^2 and 5.0×40.0 cm^2 fields were attained using a TomoElectrometer 8-channel electrometer with a calibrated A1SL ion chamber in a TomoScanner water tank (Standard Imaging, Middleton, WI) at SSD=85. The TomoScanner has software that can automatically record readings from each of the 8 channels at a specified sampling rate. The tank's robotic arm can move two dimensionally with either a continuous motion or arbitrary step size in the horizontal and vertical directions; we employed a 1 mm step size. We scanned various stationary fields where the central MLC leaves defined 2.5, 5.0, 10.0 and 20.0 cm field widths (transverse direction) and the collimator jaws defined T_{slice} = 2.5 and 5.0 cm field openings in the axial direction. They were measured with the A1SL ion chamber as well. All test fields were delivered with a stationary gantry angle of 0° and with a stationary couch. MC results for the PDD employed a dose grid size of 0.5x0.5x0.2 cm^3 and were calculated with $7x10^8$ histories to keep the calculation uncertainty below 1%.

Overall field profiles for field sizes of 5.0×40.0 cm^2 and 2.5×40.0 cm^2 with all 64 MLC leaves open were measured in the X_{IEC} (lateral) and Y_{IEC} (longitudinal) directions

again using the A1SL ion chamber in the TomoScanner water tank with SSD=85cm. The MC simulation used $0.2 \times 0.5 \times 0.2$ cm^3 grid size and calculation uncertainty was kept below 1% for dose points greater than 50% D_{max}.

A picket-fence pattern MLC field with the even numbered MLC leaves open and the odd numbered MLC leaves closed across a 5.0 cm field width was used to deliver a 36 second dose to a large EDR2 film (35 cm$\times$43 cm) at 1.5 cm depth in a $15 \times 55 \times 5.5$ cm^3 solid water phantom. The film was placed at the isocenter plane with SAD = 85 cm.

The MLC leakage was measured using the same set up as the picket-fence pattern film measurement. All leaves were closed during the 2000 second beam delivery. Then, all leaves were opened to give a 5.0×40.0 cm^2 field with 30 second delivery as a reference field. The leakage lateral profile was divided by the reference lateral profile to get the percent leakage. The time factor of $\frac{2000}{30}$ was used in this calculation (Sarkar et al., 2007).

Finally, a complex MLC dynamic modulation was simulated and measured in order to verify our SCS simulation of the intensity modulation. We simulated our film calibration procedure for the tomotherapy DQA, which was reported in our previous work (Thomas et al., 2005a). In this procedure, a highly modulated beam with a 5.0 cm field width in a 44-second irradiation time was delivered to a film on the treatment couch, 4 seconds with all leaves closed and 40 seconds of modulated beam delivery. Using a set up like that for the picket-fence pattern and the MLC leakage, 13 levels of dose from approximately 0.25 to 4.5 Gy was delivered to a series of EDR2 films. These 13 dose levels were also measured by the A1SL ion chamber in the water tank with the same SAD and depth. The MLC pattern for this delivery involved the 52 central leaves from

number 7 to number 58. They were divided into 13 groups with different opening durations. Moreover, in an attempt to correct for the non flat beam profile, each one of the four leaves in a group had a slight difference in the opening duration. To simulate this pattern, we needed 50 different static components. This gives us a rigid test of SCS.

4.2.4 CT data phantom measurement

For a CT phantom calculation, we used the CT data sets of a Cheese Phantom. The CT images were obtained with a Picker PQ 5000 CT scanner (Philips Medical Systems, Cleveland, OH). The Cheese Phantom CT data set had dimensions of 256×256×110 with a voxel size of 1.875×1.875×2.000 mm^3. The Cheese Phantom is a solid water cylinder that is 30 cm in diameter and 18 cm long. With this phantom, we created a preliminary treatment delivery plan with one PTV having a 5.2 cm diameter and a 3 cm length located at the center of the phantom and two OARs of the same size on each side of the PTV. We used the TPS to generate a 2.61 rotation (133 projections) plan with a typical 5.0 cm field size and a pitch of 0.86. The beam delivery time was 125.2 seconds. The plan had the constraints that 95% of the PTV volume was to receive at least 30.0 Gy and less than 50% of the volume of each OAR was to receive a dose higher than 15.0 Gy. The whole plan was designed to be delivered in 10 fractions, i.e. 3 Gy to the PTV and median OAR dose of less than 1.5 Gy per delivery. A point dose measurement with the A1SL ion chamber was obtained for a point near the center of the Cheese Phantom. An EDR2 film measurement at the central coronal plane was also obtained to compare with the MC and the TPS calculations. This test is the same as that for a DQA treatment plan (Thomas et al., 2005a). All calculation results were compared with a film measurement using the

gamma index defined by Low et al. (Low et al., 1998). Two acceptance criteria, 2%/2mm and 5%/3mm, were used (Thomas et al., 2005a). The Gamma index is defined as:

$$\gamma(r_c) = \min\{\Gamma(r_c, r_m)\} \forall \{r_m\}, \qquad [4-3]$$

where

$$\Gamma(r_m, r_c) = \sqrt{r^2(r_m, r_c)/\Delta d_M^2 + \delta^2(r_m, r_c)/\Delta D_M^2}, \qquad [4-4]$$

$$r(r_m, r_c) = |r_m - r_c|, \qquad [4-5]$$

and

$$\delta(r_m, r_c) = \frac{(D(r_m) - D(r_c))}{D_p} \times 100\%. \qquad [4-6]$$

r_c is the position of the calculated dose pixel and r_m is the position of the measured dose pixel. $D(r_c)$ is the calculated dose at position r_c and $D(r_m)$ is the measured dose at position r_m. Δd_M is the distance to agreement criteria and ΔD_M is the dose difference criteria. D_p is the prescription dose (Thomas et al., 2005a).

4.3 Results

4.3.1 The radiation source validation

4.3.1.1 Percent Depth Dose

The measured results compared with the MC simulations of PDDs for the 5.0 cm width field are shown in Figure 4-3(a) and the PDDs for the 2.5 cm width fields are shown in Figure 4-3(b). MC simulation placed d_{max} at 1.3 cm for all fields. Measurement results showed d_{max} varied from 1.2-1.4 cm. Comparing the measured results and the MC results point by point, 94-96% points of a MC PDD curve agree with the measurement results using 1%/1mm acceptance criteria. The discrepancies appear at the buildup region

from 0 to 6 mm at the surface. This is likely due in large part to the ion chamber volume averaging effect.

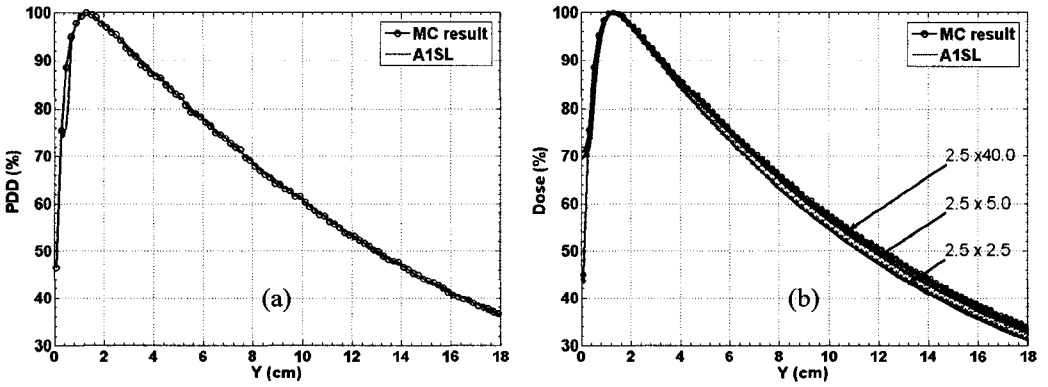

Figure 4-3. ***(a)*** *The MC simulated and A1SL measured PDDs of 5.0× 40.0 cm² helical tomotherapy fields along the central axis.* ***(b).*** *MC simulated and A1SL measured PDDs of 2.5 × 40.0, 2.5 × 5.0 and 2.5 × 2.5 cm2 helical tomotherapy fields along the central axis. The PDDs of 2.5 × 20.0, 2.5× 10.0 cm² are similar to 2.5× 40.0 cm² and are not shown here.*

4.3.1.2 Profiles

The overall profiles of fields 5.0×40.0 and 2.5×40.0 cm² are shown in Figure 4-4(a) and 4-4(b). The lateral profiles are compared with MC results at depths of 1.5 cm, 5 cm and 10 cm. The longitudinal profiles are compared at depths of 1.5 cm, 5.0 cm, 10.0 cm, 15.0 cm and 20.0 cm. The FWHM of all the profiles of both fields agree with the measurements to within 1mm. This indicates the jaws and the MLC have correctly defined geometries. The cone shape of the lateral profiles is different from that of a conventional linac due to the absence of a flattening filter. The MC simulations correctly reproduce this shape. For both fields, the MC dose values agree with the measurement to within 2%/1mm for both lateral and longitudinal profiles.

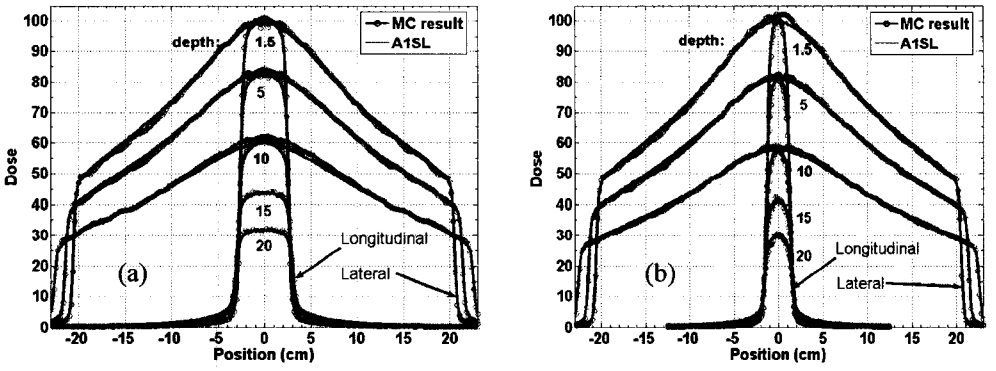

Figure 4-4. *(a) MC simulated and A1SL measured lateral and longitudinal profiles of 5.0× 40.0 cm² helical tomotherapy fields.* ***(b).*** *MC simulated and A1SL measured lateral and longitudinal profiles of 2.5 × 40.0 cm² helical tomotherapy fields.*

4.3.2 Static MLC validation

4.3.2.1 MLC picket-fence pattern validation

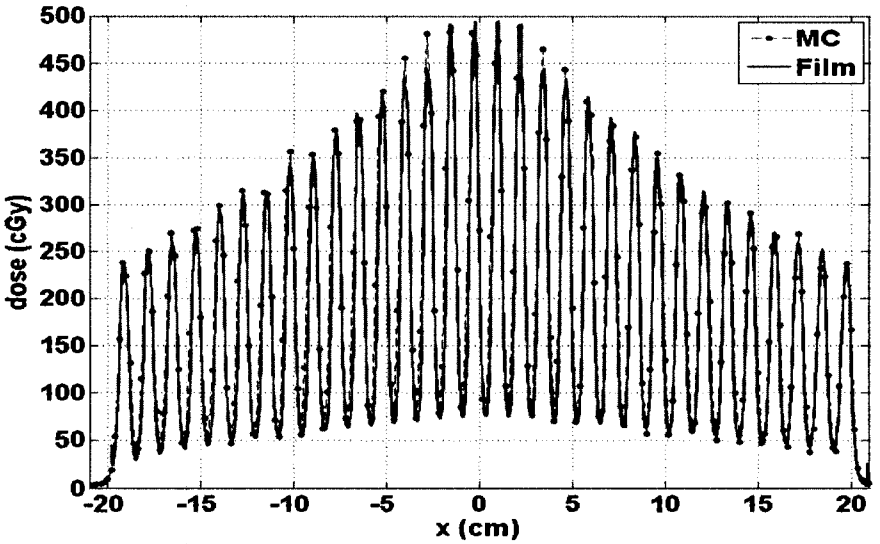

Figure 4-5. *The MC simulated and the film measured picket-fence pattern of a 5.0× 40.0 cm² helical tomotherapy field.*

The MLC simulation was verified by a picket-fence pattern and the MLC leakage measurements. The picket-fence results are shown in Figure 4-5. The simulation has

97.3% of points (244 of 251 points) in agreement with film measurement using a 2%/1mm acceptance criteria. Only 2.7% of the points (7 points) have dose differences larger than 2%. Agreement with film measurement indicates the MLC geometry is correctly modeled and the T&G effect is adequately reproduced.

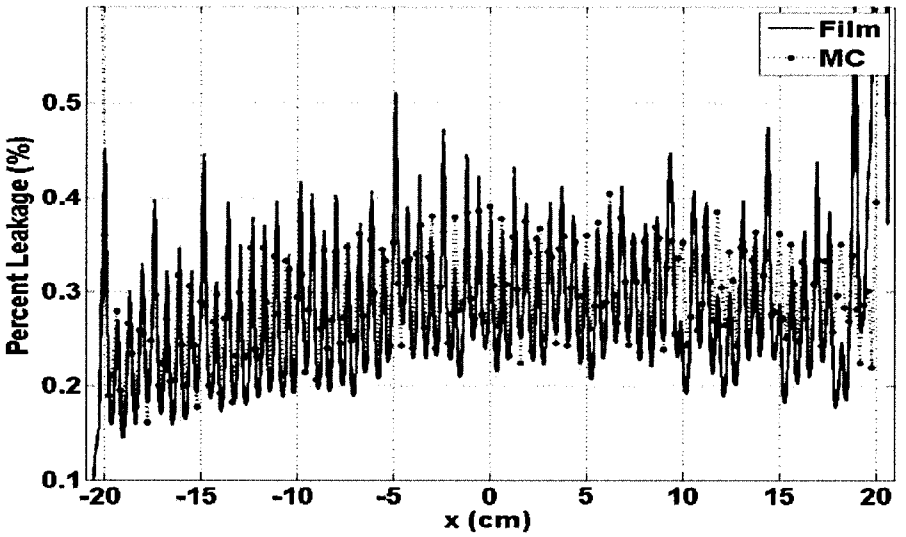

Figure 4-6. *MC simulated and film measured MLC percent leakage in lateral direction of the 5.0× 40.0 cm^2 helical tomotherapy field.*

4.3.2.2 MLC leakage validation

The MLC leakage results are shown in Figure 4-6. The film results indicate the average interleaf leakage is 0.28% with a maximum leakage of 0.51%. This agrees with Balog et al's report (2005). In our simulation results, the average interleaf leakage is 0.29% with a maximum leakage 0.41%. The agreement of the simulation results compared with the film measurements indicates not only correct MLC geometry, but also that the T&G and the overlap of T&G are correctly modeled.

4.3.3 Dynamic MLC validation

The complex modulated DQA film calibration procedure was simulated to verify our SCS MC model. The results compared with EDR2 film and the A1SL results are shown in Figure 4-7. The MC results agree with 10 of the total 13 points of the AlSL ion chamber measurements within 1%. The MC simulation at one of the three discrepant points agrees with the film result. The MC results agree with all 13 A1SL ion chamber measurements within 2%. Compared with the film results, MC simulation has 93.2% (234 of 251 points) in agreement with the film measurement using 2%/1mm criteria. Of the 17 points which do not agree with the film, 10 of these points agree with A1SL measurements within 2%/1mm. It should be noted that this level of field modulation is much greater than what is typically encountered for any one projection in even a heavily modulated clinical tomotherapy treatment plan.

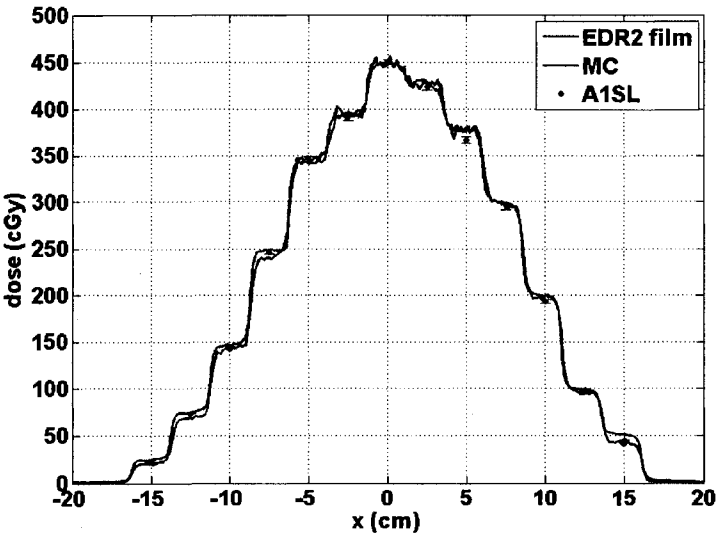

Figure 4-7. *The DQA film calibration procedure simulation, film, A1SL measurement and MC simulation results.*

4.3.4 Dynamic helical tomotherapy delivery simulations in the Cheese phantom

With respect to the helical dose delivery calculations performed on the Cheese Phantom, the point dose measurement in the PTV was 333.3 cGy, the TPS prediction was

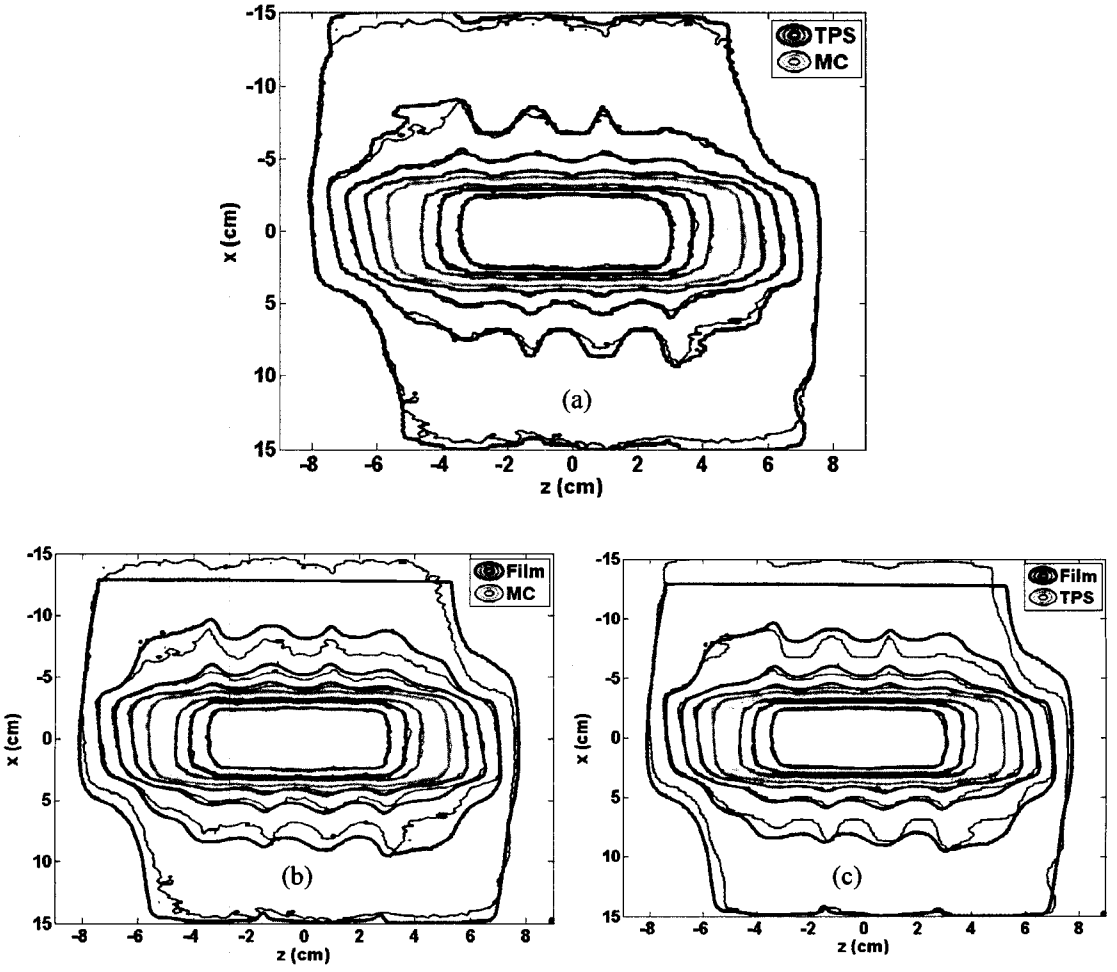

Figure 4-8. ***(a).*** *The isodose lines of the Cheese Phantom MC and TPS calculations.* ***(b).*** *MC calculation result compared with the film measurement.* ***(c).*** *TPS calculation result compared with the film measurement. The isodose lines, 90%, 80%, 70%, 60%, 50%, 40%, 30%, 20% and 10% Dmax are depicted in all of the three figures.*

335.0 cGy and MC predicted a dose of 335.8 cGy. The MC to dose calibration procedure was performed by comparing a measured one minute 5x40 cm^2 field output with the MC

simulation of the same field. The measurement was 856.5 ± 1.7 cGy/min and the MC result yielded 2.21e-16 ± 1% Gy/particle. The calibration factor is therefore 6.45e14 particle/sec ± 1%. Based on this number we can obtain a calibrated dose for the MC simulations. The TPS and MC calculations have 0.5% and 0.75% percent discrepancies respectively with the ion chamber measurement.

The dose distributions compared with the film measurement are shown in Figure 4-8. The MC simulation has dose calculation uncertainties below 1.5% within the PTV and the OARs have uncertainties below 5%. The TPS and MC calculated dose levels from 90% to 10% D_{max} are compared with the film measurement. The TPS result agrees with the MC simulation very well for these dose levels in Figure 4-8(a). Good agreements of 30% to 90% isodose lines between calculations and film measurements are found for both the TPS and MC results in Figure 4-8(b) and 4-8(c). These isodose lines satisfy a 2 mm distance-to-agreement.

Gamma maps are shown in Figure 4-9(a) and 4-9(b). The gamma values with 2%/2mm criteria for TPS and MC are below or equal 1 in the regions with dose higher than 30% D_{max}. The larger discrepancies from the film measurement for both TPS and MC calculations are found in the regions with dose lower than 30% D_{max}. The large discrepancies in low dose regions were reported in other researchers' MC/film comparisons (Seco et al., 2005) and our previous TPS vs. ion chamber measurements (Thomas et al., 2005a). The out-of-plane dose gradient, which will cause a large dose difference for small positioning errors perpendicular to the measurement plane, is probably the most important reason for these differences. Moreover, these discrepancies appear at the dose range 0.4-0.6 Gy, where the EDR2 film's response is non-linear and

may not be as well calibrated. Analyses with gamma value histograms having 2%/2mm and 5%/3mm criteria of calculations compared to film measurements in the PTV and OARs are shown in Figure 4-10(a) and 4-10(b). For the strict 2%/2mm criteria, in the PTV, the MC result shows 99.8% voxels passing the 2%/2mm test and 100% TPS voxels passing the test. In OARa, 87.0% of the MC voxels pass the 2%/2mm test and 95.2% of the TPS voxels pass the test. In OARb, 66.2% of the MC voxels pass the test and 72.9% of the TPS voxels pass the test. Even though the MC results have a higher gamma value than the TPS results, this can be attributed to the intrinsic calculation uncertainty, which increases with decreasing dose. For the 5%/3mm criteria, all regions pass the gamma value test for both the MC simulation and the TPS calculation compared with the film measurements. There is no significant system error (bias) in the MC result. Overall, both

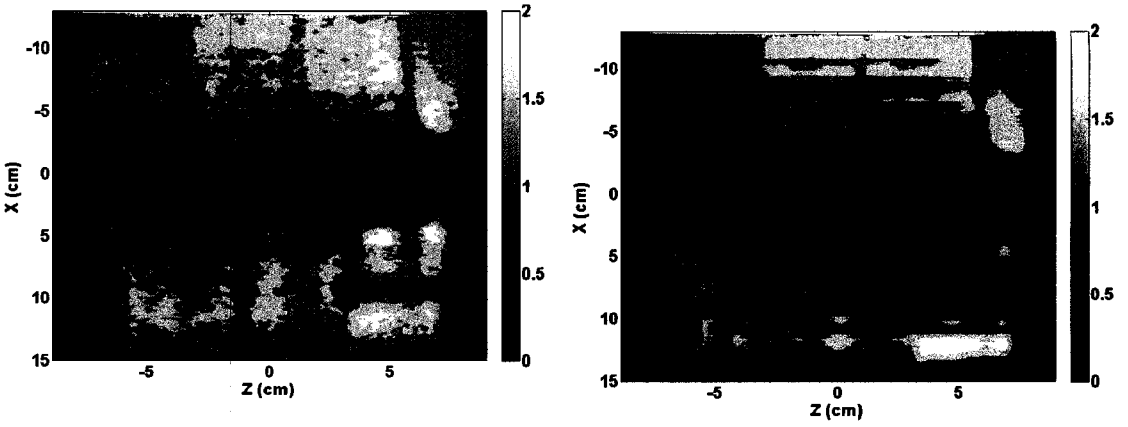

Figure 4-9. *Two gamma maps calculated with 2%/2mm criteria. **(a).** The gamma map of MC result is compared with film measurement. **(b).** The gamma map of TPS result is compared with film measurement. (Gamma index is defined as Low et al.(1998))*

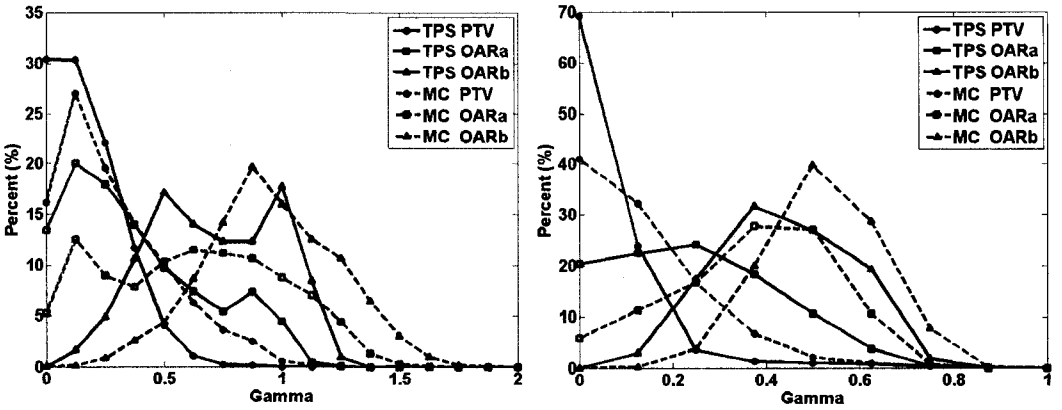

Figure 4-10. ***(a)*** *Gamma values distribution histogram with 2%/2mm criteria of TPS/film comparison and MC/film comparison in different regions.* ***(b).*** *Gamma values distribution histogram with 5%/3mm criteria of TPS/film comparison and MC/film comparison in different regions.*

methods predict the dose distribution in a homogeneous phantom correctly. The MC results have an uncertainty below 2% within the PTV, which should be adequate for a TPS validation.

4.4 Discussion and Conclusions

The full MC dose calculation of helical tomotherapy includes the linac source simulation, the MLC modeling, the dynamic intensity modulation and the helical delivery simulation. The simulation has been thoroughly verified at each step. The PDDs and the profile simulations agree with ion chamber measurements within 1% for PDDs and 2%/1mm for the lateral and longitudinal profiles for the 5.0×40.0 and 2.5×40.0 cm^2 open fields at different depths. The simulation of the MLC picket-fence pattern agrees to 2%/1mm with the film measurement. The MLC leakage simulation agrees with the film measurement, previous theory estimation and other reports (Balog et al., 2005; 1999).

These validations show our model correctly simulates the MLC geometry with the T&G effect, interleaf leakage, and penumbra with a high degree of accuracy.

The highly complex DQA film calibration procedure provided a means of testing the simulation of dynamic intensity modulation. Our results agree with the ion chamber and the film measurements to within 2%/1mm. This test demonstrates the SCS model correctly reproduces the beam fluence seen in a helical tomotherapy delivery.

A preliminary clinical treatment plan delivered to a Cheese Phantom was simulated. This plan integrated the whole model of the helical delivery. Our method of simulating the helical delivery agrees with the film measurement, with the voxels meeting a 2%/2mm acceptance criteria in regions where the statistical uncertainty is such that this criteria would apply. This method simulates multiple-field-incidence in the same manner as the helical tomotherapy TPS. The TPS results agree with the film measurement as well. The TPS calculation in the homogeneous water-like Cheese Phantom gives a result which is comparable in accuracy with the MC calculation. Ultimately we have shown that MC simulations using the described methodology can reproduce a known result. Thus, this work establishes a platform by which TPS calculations can be verified by the MC approach in situations where MC is known to provide a more accurate description of dose distributions (e.g. in the presence of large low or very high density inhomogeneities or dose in buildup regions).

The computation time for our method should be mentioned while considering possible applications. As simulated, the Cheese Phantom simulation required approximately 3.5 hours (real time) to generate the PSF2 files and an additional 50 hours to calculate the final dose distribution. Clinical treatment plans could take 4~5 times as

long. This computation time is acceptable for research purposes, for evaluating the TPS calculation accuracy in difficult situations. However, it is too long for patient plan verification under current conditions. Future work focusing on the reduction of computation time, application of faster codes, and inevitable improvements in processing speed are expected to address this problem.

Bibliography:

Balog, J. P., Lucas, D., DeSouza, C., and Crilly, R. (2005): Helical tomotherapy radiation leakage and shielding considerations. *Med. Phys.* **32**, 710-9.

Balog, J. P., Mackie, T. R., Wenman, D. L., Glass, M., Fang, G., and Pearson, D. (1999): Multileaf collimator interleaf transmission. *Med. Phys.* **26**, 176-86.

Davidson, S. E., Ibbott, G. S., Prado, K. l. L., Dong, L., Liao, Z., and Followill, D. S. (2007): Accuracy of two heterogeneity dose calculation algorithms for IMRT in treatment plans designed using an anthropomorphic thorax phantom. *Med. Phys.* **34**, 1850-57.

Han, C., Chen, Y. J., Liu, A., Schultheiss, T. E., and Wong, J. Y. (2007): Dosimetric study and in-vivo dose verification for conformal avoidance treatment of anal adenocarcinoma using helical tomotherapy. *Med. Dosim.* **32**, 33-37.

Jones, A. O., and Das, I. J. (2005): Comparison of inhomogeneity correction algorithms in small photon fields. *Med. Phys.* **32**, 766-76

Kron, T., Grigorov, G., Yu, E., Yartsev, S., Chen, J. Z., Wong, E., Rodrigues, G., Trenka, K., Coad, T., Bauman, G., and Van Dyk , J. (2004): Planning evaluation of radiotherapy for complex lung cancer cases using helical tomotherapy. *Phys. Med. Biol.* **49**, 3675-90.

Liu, H. H., Verhaegen, F., and Dong, L. (2001): A method of simulating dynamic multileaf collimators using Monte Carlo techniques for intensity-modulated radiation therapy. *Phys. Med. Biol.* **46**, 2283-98.

Low, D. A., Harms, W. B., Mutic, S., and Purdy, J. A. (1998): A technique for the quantitative evaluation of dose distributions. *Med. Phys.* **25**, 656-61.

Mackie, T. R. (2006): History of tomotherapy. *Phys. Med. Biol.* **51**, R427–R453.

Mackie, T. R., Holmes, T., Swerdloff, S., Reckwerdt, P., Deasy, J. O., Yang J., Paliwal, B., and Kinsella T. (1993): Tomotherapy: a new concept for the delivery of dynamic conformal radiotherapy. *Med. Phys.* **20**, 1709-19.

McNutt, T. R., Mackie, T. R., and Paliwal, B. R. (1997): Analysis and convergence of the iterative convolution/superposition dose reconstruction technique for multiple treatment beams and tomotherapy. *Med. Phys.* **24**, 1465–76

Reft, C., Alecu, R., Das, I. J., Gerbi, B. J., Keall, P., Lief, E., Mijnheer, B. J., Papanikolaou, N., Sibata, C., and Van Dyk, J. (2003): Dosimetric considerations for patients with HIP prostheses undergoing pelvic irradiation. Report of the AAPM Radiation Therapy Committee Task Group 63. *Med. Phys.* **30**, 1162-82.

Rogers, D. W. O., Faddegon, B. A., Ding, G. X., Ma, C.-M., Wei, J., and Mackie, T. R. (1995): BEAM: A Monte Carlo code to simulate radiotherapy treatment units. *Med. Phys.* **22**, 503-24.

Sarkar, V., Lin, L., Shi, C., and Papanikolaou, N. (2007): Quality assurance of the multileaf collimator with helical tomotherapy: Design and implementation. *Med. Phys.* **34**, 2949-56.

Seco, J., Adams, E., Bidmead, M., Partridge, M., and Verhaegen, F. (2005): Head-and-neck IMRT treatments assessed with a Monte Carlo dose calculation engine. *Phys. Med. Biol.*, 817-30.

Thomas, S. D., Mackenzie, M., Field, G. C., Syme, A. M., and Fallone, B. G. (2005a): Patient specific treatment verifications for helical tomotherapy treatment plans. *Med. Phys.* **32**, 3793-3800.

Thomas, S. D., Mackenzie, M., Rogers, D. W. O., and Fallone, B. G. (2005b): A Monte Carlo derived TG-51 equivalent calibration for HT. *Med. Phys.* **32**, 1346–53.

TomoTherapy-Inc. (2005): Hi-Art system physics guide. *TomoTherapy Inc.,T-USR-HB0013G-0905.*

Vanderstraeten, B., Reynaert, N., Paelinck, L., Madani, I., Wagter, C. D., Gersem, W. D., Neve, W. D., and Thierens, H. (2006): Accuracy of patient dose calculation for lung IMRT: A comparison of Monte Carlo, convolution/superposition, and pencil beam computations. *Med. Phys.* **33**, 3149–3158.

Walters, B. R. B., Kawrakow, I., and Rogers, D. W. O. (2005): DOSXYZnrc Users Manual, NRC Report PIRS 794(rev. B).

Zeidan, O. A., Langen, K. M., Meeks, S. L., Manon, R. R., Wagner, T. H., Willoughby, T. R., Jenkins, D. W., and Kupelian, P. A. (2007): Evaluation of image-guidance protocols in the treatment of head and neck cancers. *Int. J. Radiation Oncology Biol. Phys.* **67**, 670-7.

Chapter 5 : Monte Carlo evaluation of a treatment planning system for helical tomotherapy in an anthropomorphic heterogeneous phantom and for clinical treatment plans

5.1. Introduction

Helical tomotherapy is an external radiotherapy process that delivers intensity modulated radiation therapy (IMRT), as well performing image guided adaptive radiotherapy (IGAR) (2006; Mackie et al., 1993). It features an onboard megavoltage computed tomography system (MVCT) through which it accomplishes image guidance. It delivers a complex modulated set of beams from significantly more angles than typically found in conventional linac IMRT, which often results in better conformity of radiation dose distribution to the planning target volume (PTV) and avoidance of nearby organs at risk (OAR). This technology can result in better homogeneity of the dose distribution within a PTV, while maintaining the same or better sparing of normal tissue compared to conventional three dimensional conformal radiotherapy (3D-CRT) and some linac IMRT deliveries (Han et al., 2007; Kron et al., 2004; Zeidan et al., 2007).

The current commercially available helical tomotherapy unit is the Hi-ART II (TomoTherapy Inc. Madison, WI, USA). The system utilizes its own dedicated treatment planning system (TPS). This TPS uses a convolution/superposition algorithm for the dose calculation (McNutt et al., 1997), which inherently assumes the condition of charged particle equilibrium (CPE) throughout the calculation volume. We can reasonably expect

the TPS will have difficulties in accurately predicting the dose in certain situations, such as when significant inhomogeneities exist in the patient geometry, or when treatment consists of small fields or highly modulated beamlets, in which cases this assumption is not satisfied. In the build-up regions behind air cavities, such as those found in a head and neck or a lung treatment, 5%~7% (of maximum dose) deviations can be found (Davidson et al., 2007; Seco et al., 2005; Vanderstraeten et al., 2006). MC dose calculations can be used to validate the TPS predicted dose in such cases (Seco et al., 2005; Vanderstraeten et al., 2006).

We have developed a full MC dose calculation method for helical tomotherapy, as described in the previous chapter (Zhao et al., 2008). Here we apply this system to a heterogeneous phantom with a simulated patient treatment plan. The phantom allowed for experimental validation of both MC and TPS results. We then consider the doses calculated from both systems for a clinical head-and-neck cancer treatment.

5.2 Methods and materials

5.2.1 Monte Carlo calculation of helical tomotherapy

As already mentioned, the MC model of the Hi-ART II Helical Tomotherapy unit was established and commissioned, which has been described in the proceeding chapter as well as in the literature (Zhao et al., 2008). Our MC system uses the BEAMnrc/DOSXYZnrc software packages to perform a full MC simulation of a helical tomotherapy dose delivery. The model was verified at three levels: the source simulation, MLC modeling/dynamic intensity modulation and finally dose distribution of the helical delivery. The MC model was commissioned to two typical jaw settings, T_{slice}=2.5 cm and T_{slice}=5.0 cm. These define the radiation field width in the couch movement

direction at the isocenter. The MC calculation was calibrated by comparing a measured one minute 5x40 cm^2 field output with the MC simulation of the same field. The measurement was 856.5 ± 1.7 Gy/min and the MC result yielded 2.21e-16 ± 1% Gy/particle. The calibration factor is therefore 6.45e14 particle/sec ± 1%. Once planned on the TomoTherapy Hi-ART TPS (version: 2.2.0.259), a patient dose distribution can be re-calculated on our MC platform.

An in-house program written for Matlab (version R2006a, the MathWorks Inc., Natick, MA, USA) reads the selected TomoTherapy TPS archived patient file and automatically writes BEAMnrc and subsequent DOSXYZnrc input files. Additionally it monitors and steers the sequential MC simulation processes to get a final dose distribution of the helical delivery. The program can also read the patient structures delineated by radiation oncologists in the plan and provide analysis of calculation results to give dose volume histogram (DVH) and gamma index (Low et al., 1998) information using these structures.

CT images used in this study were all obtained with a Picker PQ 5000 CT scanner. For a treatment planning dose calculation, the diagnostic CT couch needed to be replaced by the pre-saved Helical Tomotherapy couch CT data set to perform the calculation in the real helical tomotherapy dose delivery situations. The difference between the diagnostic CT couch and helical tomotherapy couch must be account for. This is necessary in helical tomotherapy due to the helical delivery often requiring a portion of the treatment beams to pass through the couch, whereas this may often be avoided in conventional linac based IMRT. The typical CT data set had a voxel size of $1.875 \times 1.875 \times 3.000$ mm^3. Our in-house Matlab program reads the TPS CT data set and converts it to a DOSXYZnrc

phantom file. The phantom grid has the same voxel size and setup for MC calculation as in the TPS calculation. In converting CT data to a DOSXYZnrc phantom, a ramp table with four materials (air, lung, soft tissue and bone), densities and their calibrated CT numbers for our CT scanner was applied and the material and density of each voxel were assigned by linearly interpolating the data in the ramp table. All simulations were performed with the electron cutoff energy ECUT = 0.7 MeV and the photon cutoff energy PCUT = 0.01 MeV. The dose calculation used 10^9 histories (10^8 recycled 10 times) to get the uncertainty below 1% in high dose regions (PTV). The TomoTherapy TPS uses the effective mass attenuation coefficients derived from water and cortical bone to calculate the Total Energy Released per unit of MAss (TERMA) for dose convolution. The dose kernel is calculated by using range scaling by physical density of the Monte Carlo generated kernel in water. Then, the doses reported are dose-to-medium (Mackie and Reckwerdt, 2001). Hence, both the MC and TPS dose results were converted from dose-to-medium to dose-to-water (Siebers et al., 2000) to compare with the measured results in the CIRS phantom in this work. In this conversion, dose-to-bone has the largest difference from dose-to-water, which is above 10%, while soft tissue is approximately 1% (Siebers et al., 2000). There is no dose conversion of either MC or TPS in the evaluation of the head-and-neck treatment plan.

For this work, the MC calculations were performed on a Linux cluster with 18 AMD Opteron64 CPUs operating at 2.0 GHz (AMD, Sunnyvale, CA, USA) and managed by ROCKSv3.3 (Rocks Cluster Group, San Diego Supercomputer Center, UC San Diego, USA).

5.2.2 Measurements and calculations for an anthropomorphic heterogeneous thorax phantom

To assess the TPS with known inhomogeneities in a clinically relevant situation, a treatment plan with the same order of complexity as a clinical plan is mimicked using a heterogeneous CIRS phantom (Model 002LF IMRT Thorax Phantom, Computerized Imaging Reference Systems (CIRS) Inc., VA, USA) as shown in Figure 5-1. This phantom has an elliptical shape and it represents an average human torso in density and structure. It measures 30 cm long×30 cm wide×20 cm thick. The phantom is made of simulated lung (inhale) (ICRP-23, 1975), simulated bone (average density, the major part of the delineated spinal cord structure) (Woodard and White, 1986) and water equivalent materials. According to the vendor, the tissue equivalent materials mimic the dosimetric properties (mass and electron density) of water, bone, and lung within 1%. The phantom contains tissue equivalent interchangeable rod inserts which can be replaced by an ionization chamber to allow point dose measurements at different locations in the phantom. One half of the phantom is divided into 6 sections, each 2 cm thick, to support radiographic film measurements in axial planes.

5.2.2.1 CIRS thorax phantom treatment plan

We created a PTV with an irregular shape with approximate dimensions of 10x15x17 cm^3 in the CIRS phantom. The PTV is larger than the typical clinical situation. This larger PTV was chosen to contain water/tissue and a part of the right lung. It surrounded a cylindrical Organ-At-Risk (OAR1), shown in Figure 5-1. This arrangement increases the complexity of the beam modulation and radiation delivery. The plan was constrained to deliver 50 Gy to 95% of the PTV and limit the dose to 50% of the volume of the two OARs to get less than 40 Gy and the spinal cord to a maximum of 40 Gy. The

TPS generated a plan with 16.1 active gantry rotations (823 projections, assuming 51 projections in gantry angle per rotation) using T_{slice}=2.5 cm field width, a pitch value of 0.46 (the ratio of the couch translation in one rotation to the field width), and an effective modulation factor (MF) of 1.984 (a measure of modulation complexity, the maximum leaf open time compared to the average for open leaves). The plan was calculated on the TPS with a 'fine' grid setting, which used calculation grid voxel sizes of $1.875 \times 1.875 \times 3.000$ mm^3.

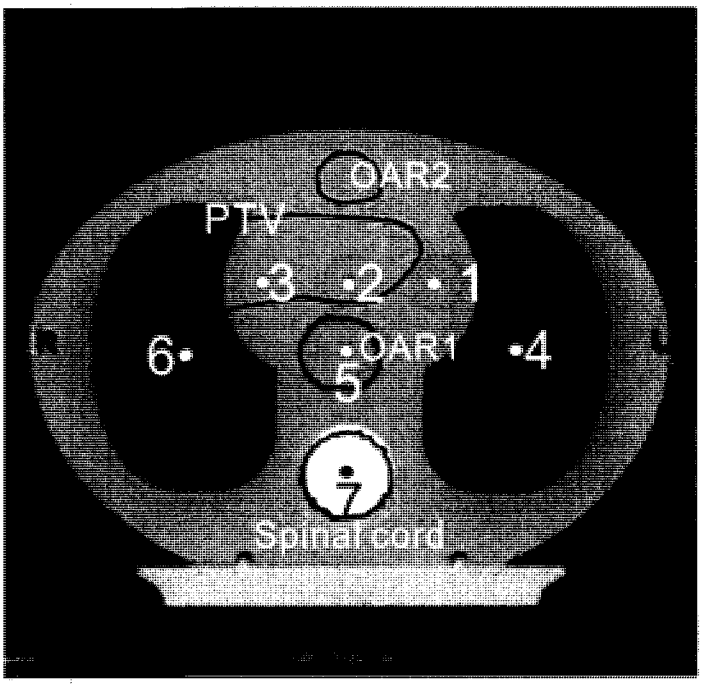

Figure 5-1. *One CT transverse slice of the CIRS anthropomorphic heterogeneous thorax phantom. The dots with numbers from 1 to 7 are the points of ion chamber measurement in the phantom. Points 4 and 6 are located in lung equivalent material and Point 7 is in bone equivalent material. Point 4 is in the left simulated lung and Point 6 is in the right simulated lung. The simulated bone region was delineated as 'spinal cord' in the treatment plan. Points 2, 3 and 6 were located in the PTV and Point 5 was designated OAR1. The circle above the PTV without measuring point was designated OAR2.*

5.2.2.2 Absolute dose measurements with A1SL ion chambers

Absolute point dose measurements were taken with an Exradin A1SL ion chamber (Standard Imaging, Middleton, WI) in the CIRS phantom at points 1 through 7 (see Figure 5-1). The A1SL ion chamber has an active volume of 0.056 cm^3. Three calibrated A1SL ion chambers were used with a TomoElectrometer 8-channel electrometer. All ion chamber measured values were converted to dose to water using an AAPM TG-51 equivalent protocol (Thomas et al., 2005b). The seven points in the CIRS phantom were measured 2-8 times. The measurement results were normalized by the machine monitor dose rate of each delivery to correct for small machine output fluctuations between each measurement.

5.2.2.3 Relative dose measurements with films

Relative dose distributions were measured in the central axial plane of the CIRS phantom with Kodak EDR2 Ready Pack film (size 30 cm × 25 cm, Eastman Kodak Company, Rochester, NY, USA). The film was in the transverse plane, which is parallel to the beam axis rotation plane. The EDR2 film was scanned with a VIDAR VXR film digitizer (VIDAR Systems Corporation, Herndon, VA, USA) which was studied and calibrated in our previous work. Such film measurement procedures are routinely used for clinical QA tests (Thomas et al., 2005a). The same procedure of film measurement was repeated with Gafchromic External Beam Therapy (EBT) film (size 25cm × 20 cm, International Specialty Products, Wayne, NJ).

5.2.3 Head-and-Neck cancer treatment plan

One clinical nasopharynx cancer plan was recalculated by the MC method. The treatment plan was generated by the TPS to deliver 66 Gy and 54 Gy to 90% of the PTVs

while avoiding the brain, the spinal cord, the parotids, and the optic chiasm. Our institution's in house IMRT protocol constraints were applied to these targets and OARs with 90% of PTV66 to receive ≥ 66Gy and 90% of PTV54 to receive ≥ 54Gy, while, 50% of one or both parotids to receive ≤ 30Gy, maximum doses of the cord and the optic chiasm dose were to be ≤ 45Gy and the maximum dose to the brain was to be ≤ 54Gy. The treatment plan used T_{slice}= 2.5 cm, pitch = 0.86 and MF=1.489. The whole plan was designed to be delivered in 30 fractions, i.e. 2.2 Gy to the PTV66 per delivery. The TPS generated the plan with 9.4 active rotations (480 projections) and with a treatment duration of 262 seconds for each fraction.

5.2.4 Dose reporting and evaluations

The gamma index method defined by Low *et al.* (Low et al., 1998) was used to evaluate the MC and TPS calculation results. Three acceptance criteria, a rigid one with ±3% prescription dose or 3mm distance-to-agreement (3%/3mm), 5%/3mm, and the most generous criterion of 7%/7mm suggested by AAPM TG-53 (Fraass et al., 1998) were used to quantify the accuracies of the calculation results. The MC and TPS results for the CIRS phantom plan were compared with the film measurement. The TPS and MC results of the patient plan were also compared.

A Matlab program was written to perform a fast 3D-search of the gamma index for dose calculation results. This algorithm is similar to the method reported by Wendling *et al.* (Wendling et al., 2007)

5.3. Results

5.3.1 Absolute dose in the CIRS phantom

The A1SL ion chamber point dose measurements are shown in Table 5-I. The point doses were measured in PTV, OARs and the region out of the PTV, with a dose range from prescription dose to about 33% the maximum dose (points 1-7 in Figure 5-1). All seven of the MC doses agree with the IC measurements within 1.5% relative difference. The largest difference is 1.49% in bone material. The root mean square (RMS) difference of MC results is 0.81%. The TPS results at these points agree with the IC measurements within 4% relative difference. The largest difference is 4.05%. The RMS of TPS results is 2.33%.

Table 5-I. Calculated and ion chamber measured values of point doses in the CIRS phantom

Point	Measurements		TPS results		MC results	
	Average (Gy)	SD	Average (Gy)	Relative Diff.*	Average (Gy)	Relative Diff.*
1	1.442	0.1%	1.410	-2.21%	1.453	0.77%
2	2.241	2.0%	2.206	-1.58%	2.223	-0.82%
3	2.187	0.1%	2.149	-1.76%	2.188	0.02%
4	0.752	0.8%	0.734	-2.39%	0.747	-0.70%
5	0.882	0.5%	0.846	-4.05%	0.876	-0.73%
6	2.219	0.3%	2.221	0.09%	2.214	-0.23%
7	0.984	0.5%	1.007	2.30%	0.999	1.49%
RMS**				**2.33%**		**0.81%**

* Relative difference, (*RDiff*) is defined as $\left(\frac{IC_i - cal_i}{IC_i}\right)\times 100\%$.

The *cal* is the TPS or MC calculation results.

** RMS: the Root Mean Square difference is defined as $\sqrt{\frac{\sum_i (RDiff_i)^2}{7}}$.

The differences between TPS and point measurements in the centers of the lung and the bone are -2.39% and 2.30%, respectively. The MC results have differences of -0.70% and 1.49%, respectively. Both TPS and MC results were converted from dose-to-medium

to dose-to-water using the same set of stopping power ratios for lung and bone when comparing the results to the measured doses (Siebers et al., 2000). The agreement, which was smaller than 3%, is consistent with the TomoTherapy TPS reporting the dose in the form of dose-to-medium. This is the same as the Varian Eclipse TPS (Esch et al., 2006) and is different from most of the commercially available TPSs such as Pinnacle and Helax (Vanderstraeten et al., 2006).

5.3.2 Relative dose measurements in the CIRS phantom

The EDR2 film measurements in the CIRS phantom with the isodose line comparisons are shown in Figure 5-2(a) and 5-2(b). Isodose lines of 10% to 100% maximum dose are shown in the figures. The isodose lines of the film measurement and the MC results are shown in Figure 5-2(a). The MC results agree with the film measurements in most parts of the phantom plane. Discrepancies were seen in the lung part of the PTV, the boundary of the left lung and a part of the OAR1. The TPS overestimated the lung dose in the PTV by about 6% and underestimated the dose in the edge of the lung, out of the PTV, by more than 3%. These discrepancies can be seen clearly in the gamma maps shown in Figure 5-3. The white color within the outlines of the phantom is the region passing the 3%/3mm prescription dose criterion, the light gray is the region failing the 3%/3mm, but passing the 5%/3mm criterion. The dark gray is the region failing the 5%/3mm but passing the 7%/7mm criterion. Only light gray is seen in the gamma map of MC vs. film (Figure 5-3(a).). The relative percentage of pixels in each volume passing the gamma criteria are shown in Table 5-II. Gamma maps of the TPS vs. film are shown in Figure 5-3(b)., with corresponding passing percentages also listed in Table 5-II. In the TPS results, larger discrepancies were seen in the lung part of

the PTV, the boundary of the left lung and a part of the OAR1. There are larger portions of discrepancy of TPS vs. film as compared to MC vs. film.

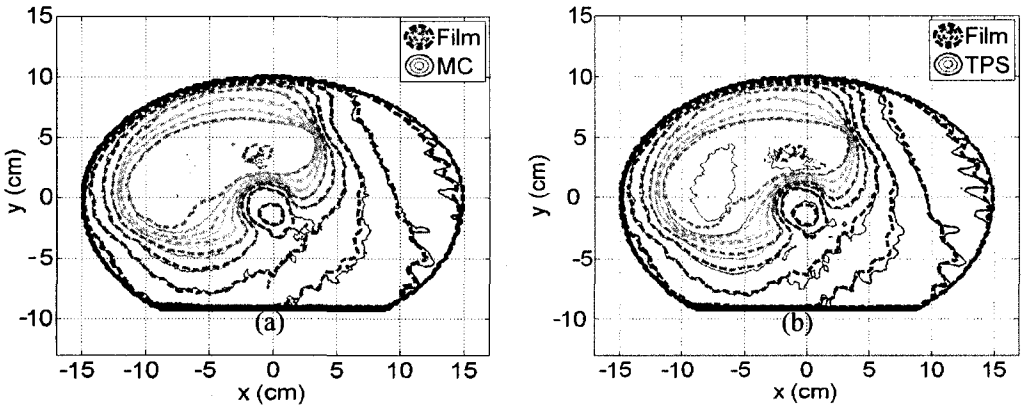

Figure 5-2. *(a).The MC calculation result compared with the film measurement.* ***(b).*** *The TPS calculation result compared with the film measurement. The isodose lines, 100%, 90%, 80%, 70%, 60%, 50%, 40%, 30%, 20% and 10% D_{max} are depicted in all of the two figures.*

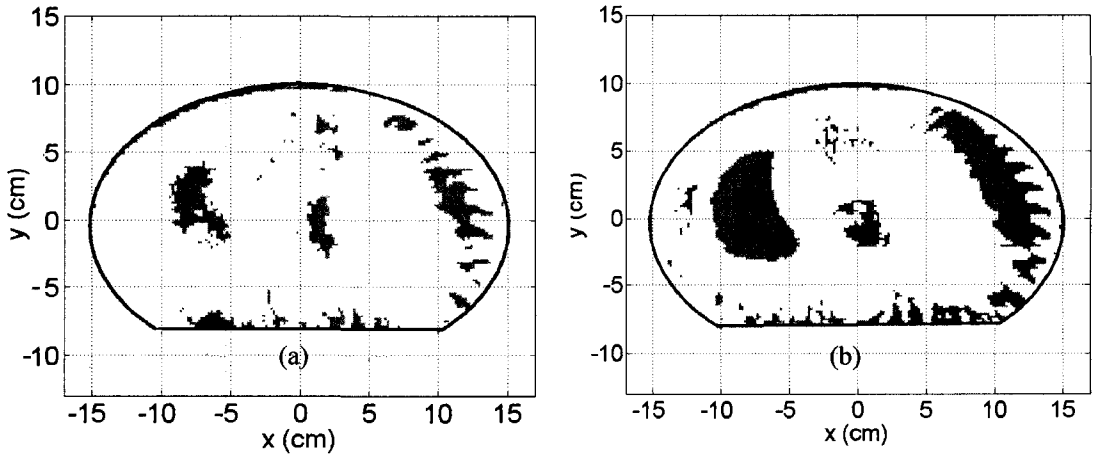

Figure 5-3. *The binary gamma maps of the calculation results compared with the film measurements.* ***(a).*** *The MC vs. the film measurement. 3%/3mm (light gray) was the only criterion not completely met.* ***(b).*** *The TPS calculation vs. the film measurement. Failure regions were seen with both the 3%/3mm and 5%/3mm criteria. The regions that failed 3%/3mm (light gray), 5%/3mm (dark gray) and 7%/7mm (black) criteria are shown in the figures with corresponding color levels.*

Both the MC and TPS calculations meet the 7%/7mm criterion in the film plane in the phantom. The MC result meets the 5%/3mm criterion in all regions and 83-100% of pixels in each volume pass the 3%/3mm criterion. In the right lung, 82.9% of the pixels pass the 3%/3mm criterion. Due to the disagreements in the lung equivalent material, only 82.3 % pass this criterion in the PTV. The TPS results have reduced agreement as shown in Figure 5-3(b) and Table 5-II. The TPS result meets the 5%/3mm criterion in 90.8-100% of pixels in each volume. Further, 53.5-99.8% of pixels in each volume pass the 3%/3mm criterion. Lung and low dose regions with high gradients show large gamma values and fail to meet these criteria.

In the isodose line comparisons, both MC and TPS show differences from the film measurement in the 10% isodose line close to the edge of the phantom. The 10% isodose lines of MC and TPS with ripples were not seen in the film measurement. This could be caused by the approximation of discrete gantry angles for delivery projections for both calculations (MC and TPS), as opposed to the actual continuous arc delivery as measured by the film. The TPS assumes the helical beam delivery was made in 51 equally spaced and discrete fixed gantry angles per rotation rather than the actually continuous arc delivery.

Both EDR2 and EBT films have been reported to have water equivalent radiation properties in a 6MV beam similar to the Hi-ART II (Sankar et al., 2006). Hence, in our film measurements, both MC and TPS doses were converted to dose-to-water to compare with the film measurements. The agreement of the TPS and MC in the bone region is consistent with the TPS reporting dose-to-medium, just as MC does.

The EBT film measurements gave comparable results to the EDR2 film. These results can be used as a validation of the EDR2 film measurements. However, one piece of the EBT film is not large enough to cover the whole transverse plane of the CIRS phantom and we used two films measured separately to get the entire planar dose information. The results are not reported here.

Table 5-II. Summary of relative volumes passing the gamma map tests in the CIRS phantom

ROI	MC			TPS		
	3%/3mm	5%/3mm	7%/7mm	3%/3mm	5%/3mm	7%/7mm
PTV	82.3%	100.0%	100.0%	57.1%	90.8%	100.0%
OAR1	88.3%	100.0%	100.0%	53.0%	97.9%	100.0%
OAR2	94.9%	100.0%	100.0%	97.5%	100.0%	100.0%
cord	95.8%	100.0%	100.0%	99.2%	100.0%	100.0%
bone	100.0%	100.0%	100.0%	99.8%	100.0%	100.0%
right lung	82.9%	100.0%	100.0%	53.5%	91.8%	100.0%
left lung	90.6%	100.0%	100.0%	76.4%	99.2%	100.0%
Average	90.7%	100.0%	100.0%	50.3%	92.9%	100.0%

5.3.3 Head-and-Neck cancer treatment plan results

The head-and-neck cancer treatment plan calculation results are shown in Figure 5-4 to Figure 5-6. Three views of isolines of 30%, 40%, 50%, 60%, 70%, 80%, 90% and 100% Dmax are shown in Figure 5-4(a)., Figure 5-5(a)., and Figure 5-6(a). The transverse, coronal and sagittal planes were at z=0.6 cm, y=3.6 cm and x=-1.3 cm respectively. The three planes were chosen to show the major discrepancies between the TPS and MC results. Gamma maps of the same planes are shown in Figure 5-4(b)., Figure 5-5(b). and Figure 5-6(b). In the gamma maps, 3%/3mm, 5%/3mm and 7%/7mm criteria were again used. Like Figure 5-3, light gray, dark gray and black were used to shown the regions failing the 3%/3mm, 5%/3mm and 7%/7mm criteria respectively. The TPS results agree with the MC results in most regions. Differences are seen in the nasal

cavity, the oral cavity and the thorax. There were no regions that failed to meet the 7%/7mm criterion. The 5%/3mm criterion only failed in a small portion of these regions.

The cumulative DVHs of the plan ROIs are shown in Figure 5-7. The TPS agrees with the MC results well in the PTV66b, the cord, the brain and the optic chiasm. Differences are seen in the PTV66a, the PTV54 and both of the parotids. Summaries of the gamma test for all regions are shown in Table 5-III. The relative volume of the ROIs passing the gamma tests for different criteria are shown in the table. All regions completely passed the 7%/7mm criterion. An average of 98.8% of the volumes passed the 5%/3mm criterion and an average of 92.7% of the volumes passed the 3%/3mm criterion. Good agreements are seen in the regions of the right parotid, the optic chiasm, PTV66b and the cord, where 100% of each volume passed the 3%/3mm criterion. The PTV54 has the worst agreement with 85.4% of the region passing the 3%/3mm criterion and 97.2% of the region passing the 5%/3mm criterion.

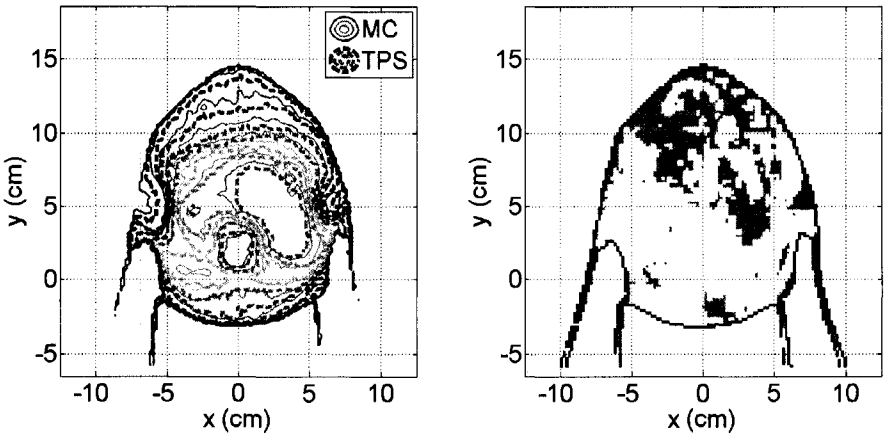

Figure 5-4. *The isodose line comparison and gamma map of the nasopharynx plan in transverse plane.* ***(a).*** *Isodose lines from 30% to 100% D_{max} comparing the MC and TPS results in the transverse plane at z = 0.6 cm.* ***(b).*** *Gamma maps with 3%/3mm, 5%/3mm and 7%/7mm criteria at the corresponding plane, with the same color scheme used in Figure 5-3.*

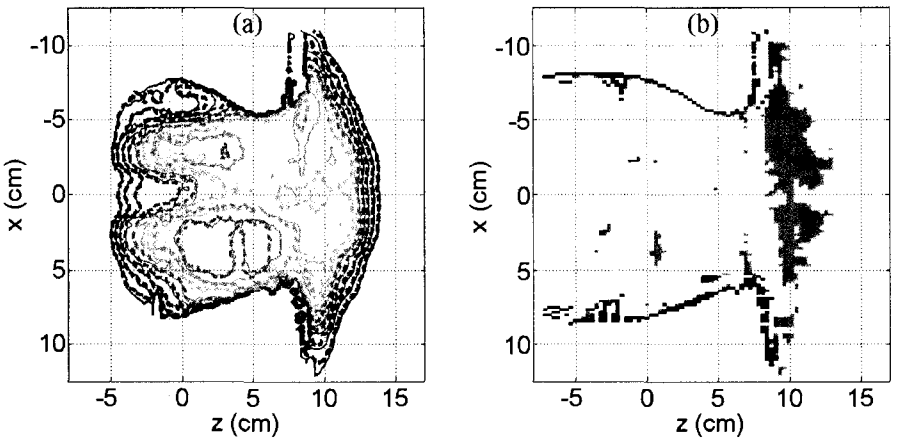

Figure 5-5. *The isodose line comparison and gamma map of the nasopharynx plan in coronal plane.* ***(a).*** *Isodose lines from 30% to 100% D_{max} comparing the MC and TPS results in the coronal plane at y = 3.6 cm.* ***(b).*** *Gamma maps with 3%/3mm, 5%/3mm and 7%/7mm criteria at the corresponding plane, with the same color scheme used in Figure 5-3.*

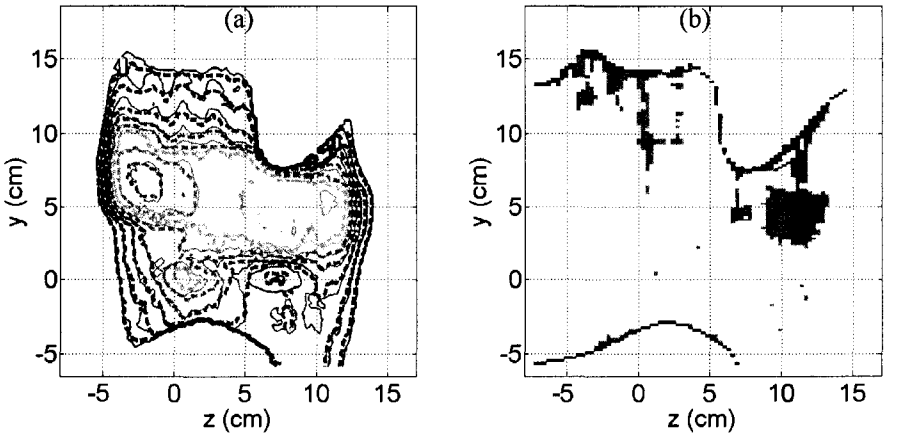

Figure 5-6. *The isodose line comparison and gamma map of the nasopharynx plan in sagittal plane.* ***(a).*** *Isodose lines from 30% to 100% D_{max} comparing the MC and TPS results in the saggital plane at x = -1.3 cm.* ***(b).*** *Gamma maps with 3%/3mm, 5%/3mm and 7%/7mm criteria at the corresponding plane, with the same color scheme used in Figure 5-3.*

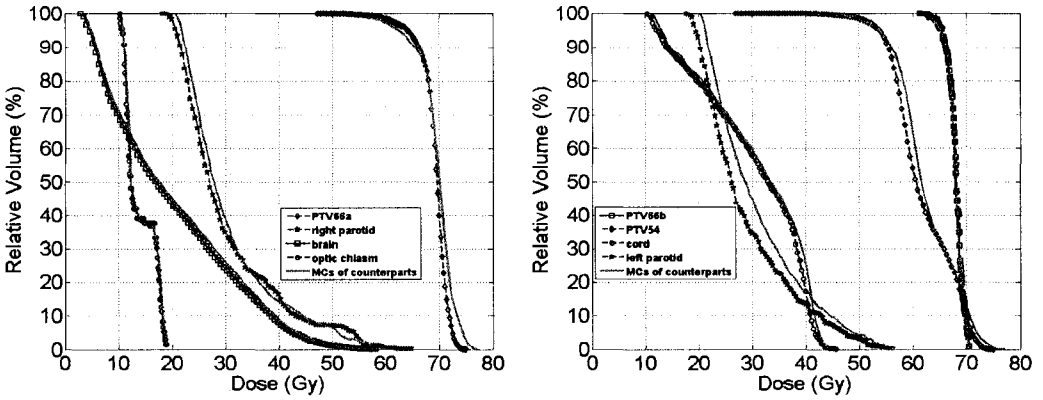

Figure 5-7. *The cumulative dose volume histograms (DVH) comparisons of the MC and TPS in the different PTVs and ROIs of the head-and-neck cancer treatment plan.*

Table 5-III. Relative volume passing the gamma test of the head-and neck cancer

ROI	3%/3mm	5%/3mm	7%/7mm
PTV66a	94.8%	99.0%	100.0%
right parotid	100.0%	100.0%	100.0%
brain	99.7%	100.0%	100.0%
Optic chiasm	100.0%	100.0%	100.0%
PTV66b	100.0%	100.0%	100.0%
PTV54	85.4%	97.2%	100.0%
cord	100.0%	100.0%	100.0%
left parotid	92.7%	99.3%	100.0%
Average	92.7%	98.8%	100.0%

5.4. Discussion and Conclusions

Full MC dose calculations of a helical tomotherapy system were applied to a heterogeneous CIRS phantom plan and a clinical head-and-neck cancer treatment plan. Ion chamber measurements, as well as both EDR2 and Gafchromic EBT radiochromic

film measurements, of a treatment delivery to the CIRS phantom were used to provide a baseline measurement evaluation of both systems.

Compared to ion chamber measurements, our MC calculation for the CIRS phantom agrees with measurement within an average of 0.81% RMS difference, the largest difference being 1.49%. The TPS has average RMS difference of 2.3%, with the largest difference being -4.05%, compared to ion chamber measurements. The larger difference in the low dose OAR was seen in our routine DQA (Delivery Quality Assurance) results (Thomas et al., 2005a). It may be due to the large dose gradients in this region, which makes the measurements particularly sensitive to probe positioning.

The MC results agree with film measurements to a clinically acceptable 5%/3mm criterion level. The more rigid criterion of 3%/3mm indicated the difference between the MC and the film measurements. In the low density region and high dose gradient OAR region, more than 82% of the voxels passed the test, and more than 90% of this volume passed the 3%/3mm test. The TomoTherapy TPS, using a convolution superposition algorithm, failed a 5%/3mm criterion level in some of the low dose regions and high dose gradient regions.

Another discrepancy of both calculation results compared to film results exists in the region at the edge of the phantom. Both MC and TPS calculation results have ripples in the isodose lines in this region. These ripples are smoothed in the film measurements. This is likely due to the difference between the discrete gantry angle projection assumptions used in both calculations and the actual continuous arc beam delivery. The assumption of 51 gantry angles per rotation, inherent in the TPS, simplifies the dose calculation. An arc of about 7° was simplified as a single beam delivered at the middle

point of the arc. This assumption leads to small deviations in source position, which are proportional to the distance from isocenter, for each projection. On the other hand, the helical tomotherapy beam is delivered about the center of the arc and this arrangement reduces this error. Moreover, the dose at one point in the radiation field of helical tomotherapy is contributed by hundreds of subfields from almost 360°. This washes out the source position error in one field. All these facts reduce the calculation errors due to this assumption and make it less serious. However, we still found 3%/3mm difference at the part which is about 13cm from the isocenter in the low dose region, combined with the presence of heterogeneity. This should be considered when a patient PTV is far from the isocenter.

In the patient treatment dose comparison, the MC method provides a tool to verify the TPS 3D-calculation within the same dose grids without positioning error. A 3D-gamma map can be used as a quantitative method to define the calculation error. Consistent with the results for the CIRS phantom, the TPS agrees with the MC calculation within 7%/7mm normalized dose criterion level in the total volume. More than 98.8% of the volume passed the 5%/3mm criterion test and more than 90% volume passed the 3%/3mm test.

In the MC simulations of the CIRS plan and clinical plan, CPU time was spent on two major steps. To calculate phase space files to get fluence information, 50-60 CPU hours were used. To calculate dose distributions in phantom/patient data sets, 450-600 CPU hours were used. On our 18 CPU cluster, about two days are needed for one full calculation. The same calculation repeated on our 40 CPU cluster finished in 24 hours. Likely, our calculation controlling program could be further optimized to reduce the

communication overhead during calculation, and more efficient methods could be employed to improve overall simulation time.

The TomoTherapy TPS provides a reasonably accurate means of dose calculation with clinically acceptable accuracy in most circumstances. However, the MC method shows better agreement with measurement as shown in this study, and therefore presents itself as a feasible means of verifying TPS calculations. Although the 1-2 day calculation time still precludes the MC method as a choice for treatment planning, our method can be used as a periodic method of DQA.

Bibliography:

Davidson, S. E., Ibbott, G. S., Prado, K. l. L., Dong, L., Liao, Z., and Followill, D. S. (2007): Accuracy of two heterogeneity dose calculation algorithms for IMRT in treatment plans designed using an anthropomorphic thorax phantom. *Med. Phys.* **34**, 1850-57.

Esch, A. V., Tillikainen, L., Pyykkonen, J., Tenhunen, M., Helminen, H., Siljamäki, S., Alakuijala, J., Paiusco, M., Iori, M., and Huyskens, D. P. (2006): Testing of the analytical anisotropic algorithm for photon dose calculation. *Med. Phys.* **33**, 4130-48.

Fraass, B., Doppke, K., Hunt, M., Kutcher, G., Starkschall, G., Stern, R., and Van Dyke, J. (1998): American Association of Physicists in Medicine Radiation Therapy Committee Task Group 53: quality assurance for clinical radiotherapy treatment planning. *Med Phys* **25**, 1773-829.

Han, C., Chen, Y. J., Liu, A., Schultheiss, T. E., and Wong, J. Y. (2007): Dosimetric study and in-vivo dose verification for conformal avoidance treatment of anal adenocarcinoma using helical tomotherapy. *Med. Dosim.* **32**, 33-37.

ICRP-23 (1975): Report of the Task Group on Reference Man.

Kron, T., Grigorov, G., Yu, E., Yartsev, S., Chen, J. Z., Wong, E., Rodrigues, G., Trenka, K., Coad, T., Bauman, G., and Van Dyk , J. (2004): Planning evaluation of radiotherapy for complex lung cancer cases using helical tomotherapy. *Phys. Med. Biol.* **49**, 3675-90.

Low, D. A., Harms, W. B., Mutic, S., and Purdy, J. A. (1998): A technique for the quantitative evaluation of dose distributions. *Med. Phys.* **25**, 656-61.

Mackie, T. R. (2006): History of tomotherapy. *Phys. Med. Biol.* **51**, R427–R453.

Mackie, T. R., Holmes, T., Swerdloff, S., Reckwerdt, P., Deasy, J. O., J.Yang, Paliwal, B., and T. Kinsella (1993): Tomotherapy: a new concept for the delivery of dynamic conformal radiotherapy. *Med. Phys.* **20**, 1709-19.

Mackie, T. R., and Reckwerdt, P. J. (2001): The convolution algorithm in IMRT. 3-D Conformal and Intensity Modulated Radiation Therapy, pp. 179-90. In J. Purdy, W. G. III, J. Palta, B. Butler, and C. Perez. (Eds), Advanced Medical Publishing Inc, Madison, WI.

McNutt, T. R., Mackie, T. R., and Paliwal, B. R. (1997): Analysis and convergence of the iterative convolution/superposition dose reconstruction technique for multiple treatment beams and tomotherapy. *Med. Phys.* **24**, 1465–76

Sankar, A., Ayyangar, K. M., Nehru, R. M., Kurup, P. G. G., Murali, V., Enke, C. A., and Velmurugan, J. (2006): Comparison of Kodak EDR2 and Gafchromic EBT film for intensity-modulated radiation therapy dose distribution verification. *Med. Dosim.* **31**, 273-82.

Seco, J., Adams, E., Bidmead, M., Partridge, M., and Verhaegen, F. (2005): Head-and-neck IMRT treatments assessed with a Monte Carlo dose calculation engine. *Phys. Med. Biol.*, 817-30.

Siebers, J. V., Keall, P. J., Nahum, A. E., and Mohan, R. (2000): Converting absorbed dose to medium to absorbed dose to water for Monte Carlo based photon beam dose calculations. *Phys. Med. Biol* **45**, 983-95.

Thomas, S. D., Mackenzie, M., Field, G. C., Syme, A. M., and Fallone, B. G. (2005a): Patient specific treatment verifications for helical tomotherapy treatment plans. *Med. Phys.* **32**, 3793-3800.

Thomas, S. D., Mackenzie, M., Rogers, D. W. O., and Fallone, B. G. (2005b): A Monte Carlo derived TG-51 equivalent calibration for HT. *Med. Phys.* **32**, 1346–53.

Vanderstraeten, B., Reynaert, N., Paelinck, L., Madani, I., Wagter, C. D., Gersem, W. D., Neve, W. D., and Thierens, H. (2006): Accuracy of patient dose calculation for lung IMRT: A comparison of Monte Carlo, convolution/superposition, and pencil beam computations. *Med. Phys.* **33**, 3149–3158.

Wendling, M., Zijp, L. J., McDermott, L. N., Smit, E. J., Sonke, J., Mijnheer, B. J., and Herk, M. v. (2007): A fast algorithm for gamma evaluation in 3D. *Med. Phys.* **34**, 1647–54.

Woodard, H. Q., and White, D. R. (1986): The composition of body tissues. *The British Journal of Radiology* **59**, 1209-19.

Zeidan, O. A., Langen, K. M., Meeks, S. L., Manon, R. R., Wagner, T. H., Willoughby, T. R., Jenkins, D. W., and Kupelian, P. A. (2007): Evaluation of image-guidance protocols in the treatment of head and neck cancers. *Int. J. Radiation Oncology Biol. Phys.* **67**, 670-7.

Zhao, Y. L., Mackenzie, M., Kirkby, C., and Fallone, B. G. (2008): Monte Carlo calculation of helical tomotherapy dose delivery. *Med Phys* **35**, 3491-3500

Chapter 6 : Discussion and Conclusions

MC methods can yield accurate radiation therapy dose calculations. There are a number of potential benefits to applying these techniques to advanced radiation therapy treatment techniques such as helical tomotherapy, which delivers multi-field IMRT to achieve maximum tumor control and minimum normal tissue complication. These benefits include giving accurate dose calculations in patient inhomogeneities; directly simulating radiation delivery with detailed geometries and materials; providing information which is difficult to measure and simulating complex problems without exponentially increasing calculation complexity. The goals of this project are the modeling helical tomotherapy radiation delivery with the MC method and to evaluate the dose calculation algorithm of the helical tomotherapy TPS with this MC model. These two goals are realized and reported in two papers reproduced in the previous two chapters.

The full MC modeling of helical tomotherapy includes linac source simulation, MLC modeling, dynamic intensity modulation and helical delivery simulation. The simulation has been thoroughly verified at each step to validate that the geometry, and that the MC codes and the dosimetry of the MC model yield correct results (i.e. consistent with measured values). The MC model was applied to sample treatment plans in homogeneous and heterogeneous phantoms. A head-and-neck cancer treatment plan was recalculated by this MC model. The accuracy of the TPS dose calculation algorithm was evaluated by comparing the MC and measurement results.

In validating the source simulation, the PDDs and the profile simulations agree with ion chamber measurements within 1% for PDDs and 2%/1mm for the lateral and longitudinal profiles for 5.0×40.0 and 2.5×40.0 cm^2 open fields at different depths. The

simulation of the MLC picket-fence pattern agrees within 2%/1mm of the film measurement. The MLC leakage simulation agrees with the film measurement, previous theory estimation (Balog et al., 1999a) and other reports (Balog et al., 2005; 1999b). These validations show our model correctly simulates the MLC geometry including the T&G effect, interleaf leakage, and penumbra with a high degree of accuracy. The highly complex DQA film calibration procedure provided a means of testing the simulation of dynamic intensity modulation. Our results agree with ion chamber and film measurement to within 2%/1mm. This test demonstrates the SCS model correctly reproduces the beam fluence seen in a helical tomotherapy delivery.

To evaluate the TPS dose calculation algorithm, a preliminary clinical treatment plan delivered to a Cheese Phantom was simulated. This plan integrated the whole model of the helical delivery. Our method of simulating the helical delivery agrees with the film measurement, with the voxels meeting a 2%/2mm acceptance criteria in regions where the statistical uncertainty is such that this criteria would apply. This method simulates multiple-field-incidence in the same manner as the helical tomotherapy TPS. The TPS results agree with the film measurement as well. The TPS calculation in the homogeneous water equivalent Cheese Phantom gives a result which is comparable in accuracy with the MC calculation.

The full MC model of a helical tomotherapy system was applied to a heterogeneous CIRS phantom plan and a clinical head-and-neck cancer treatment plan. Ion chamber measurements, as well as both EDR2 and Gafchromic EBT radiochromic film measurements, of a treatment delivery to the CIRS phantom were used to provide a baseline measurement evaluation of both systems.

Our MC calculation agrees with ion chamber measurements within an average 0.81% RMS difference, the largest RMS difference being 1.49%. The TPS has an average RMS difference of 2.3%, with the largest RMS difference being -4.1%, compared to ion chamber measurements. The larger difference at the low dose OAR was seen in our routine DQA (Delivery Quality Assurance) results (Thomas et al., 2005). It may be due to the large dose gradient in this region, which makes the measurements particularly sensitive to probe positioning.

The MC results agree with film measurements to a clinically acceptable 5%/3mm criterion level. The more rigid criterion of 3%/3mm indicated a difference between the MC and the film measurements. In the low density region and high dose gradient OAR region, more than 82% of the voxels passed the gamma criterion test and more than 90% volume passed the 3%/3mm gamma criterion test. The TomoTherapy TPS, using a convolution superposition algorithm, failed a 5%/3mm criterion level in some of the low dose regions and high dose gradient regions.

Another discrepancy of both calculation results compared to film results exists in the region at the edge of the phantom. Both MC and TPS calculation results have ripples in the isodose lines in this region. These ripples are smoothed in film measurement. This is likely due to the difference between discrete gantry angle projections used in both calculations and the actual continuous arc beam delivery. The assumption of 51 gantry angles per rotation, inherent in the TPS, simplifies the dose calculation. An arc of about 7° was simplified as a single beam delivered at the middle point of the arc. This assumption leads to small deviations in source position, which are proportional to the distance from isocenter, for each projection. On the other hand, the helical tomotherapy

beam is delivered about the center of the arc and this arrangement reduces this error. Moreover, the dose at one point in the radiation field of helical tomotherapy is contributed by hundreds subfields from almost 360°. This washes out the source position error in one field. All these facts reduce the calculation errors due to this assumption. This effect was theoretically studied by Kissick et al. They generalized that the effect is negligible for most clinical situations (Kissick et al., 2007). However, we still found 3%/3mm differences at the part which is about 13 cm from the isocenter in the low dose region, combined with the presence of heterogeneity. This should be considered in the case of a patient with a PTV that is far from the isocenter.

In patient treatment dose comparisons, the MC method provides a tool to verify the TPS 3D-calculation within the same dose grids without positioning error. A 3D-gamma map can be used as a quantitative method to define the calculation error. Consistent with the results in the CIRS phantom, the TPS agrees with the MC calculation within 7%/7mm normalized dose criterion level in the total volume. More than 98.8% of the volume passed the 5%/3mm criterion test and more than 90% volume passed the 3%/3mm test.

In the MC simulations of the CIRS plan and clinical plan, CPU time was spent on two major steps. To calculate phase space files to get fluence information, 50-60 CPU hours were used. To calculate dose distributions in phantom/patient data sets, 450-600 CPU hours were used. On our 18 CPU cluster, about two days are needed for one full calculation. The same calculation repeated on our 40 CPU cluster finished in 24 hours. Likely, our calculation controlling program could be further optimized to reduce the communication overhead during calculation, and more efficient methods could be employed to improve overall simulation time.

Ultimately we have shown that MC simulations using the described methodology can reproduce a known result. Thus, this work establishes a platform by which TomoTherapy TPS calculations can be verified by the MC approach in situations where MC is known to provide a more accurate description of dose distributions (e.g. in the presence of large low or very high density inhomogeneities, or dose in buildup regions). The TomoTherapy TPS provides a reasonably accurate means of dose calculation with clinically acceptable accuracy in most circumstances. However, the MC method shows better agreement with measurement as shown in this study, and therefore presents itself as a feasible means of verifying TPS calculations. Although the 1-2 day calculation time still precludes the MC method as a choice for treatment planning, our method can be used as a periodic method of DQA.

As mentioned previously, we have adopted a "brute force" approach to modeling the MLC position throughout the delivery with the only approximation being that of breaking the continuous delivery into 51 static fields per rotation. Modeling the MLC in this manner allows for direct comparison at the physics level between the TPS and MC systems, which is suitable for the purpose of evaluating TPS calculation algorithm accuracy. However, this approach can lead to discrepancies with measurement in the real helical delivery, which is an arc delivery rather a multi-field static delivery. This effect has been studied on a theoretical level (Kissick et al. 2007) and on the DQA experiment measurement level. Although, this effect is not found to be significant in most of the clinical situations (Thomas et al., 2005), if our MC model can be modified to simulate this real helical delivery, it is still desirable for the purpose of investigation the true dose distribution in the clinical situations. This could be a direction to extend this research.

The Hi-Art II system uses an MVCT of the patient prior to each treatment to verify the setup position of the patient. These MVCT data sets can be used in the dose calculation while reviewing the treatment courses. The patient dose calculated from these MVCT data sets with our MC system can be considered more realistic than the dose distribution calculated from the planning CT. This realistic dose distribution will benefit both the evaluations of the outcomes of the helical tomotherapy and studies of biological models of TCP and NTCP. This could be another direction for future research.

Metallic implants such as titanium or steel hip prostheses, and high Z dental fillings are increasingly present in clinical patients. These high Z materials in the body will cause serious artifacts in the planning kVCT due to the large portion of attenuation contributions from Z-dependent photoelectric effect in this kVCT photon spectrum. This makes the treatment plan difficult and can cause dose calculation errors (Reft et al., 2003). MVCT has the advantage over kVCT in this situation with negligible contribution of photoelectric effect in this spectrum (Ruchala et al., 2000). Hence, MVCT with our MC model could be a useful evaluation tool in these clinical situations.

Bibliography:

Balog, J. P., Lucas, D., DeSouza, C., and Crilly, R. (2005): Helical tomotherapy radiation leakage and shielding considerations. *Med. Phys.* **32**, 710-9.

Balog, J. P., Mackie, T. R., Wenman, D. L., Glass, M., Fang, G., and Pearson, D. (1999a): Multileaf collimator interleaf transmission. *Med Phys* **26**, 176-86.

Balog, J. P., Mackie, T. R., Wenman, D. L., Glass, M., Fang, G., and Pearson, D. (1999b): Multileaf collimator interleaf transmission. *Med. Phys.* **26**, 176-86.

Kissick, M. W., Mackie, T. R., and Jeraj, R. (2007): A delivery transfer function (DTF) analysis for helical tomotherapy. *Phys Med Biol* **52**, 2355-65.

Reft, C., Alecu, R., Das, I. J., Gerbi, B. J., Keall, P., Lief, E., Mijnheer, B. J., Papanikolaou, N., Sibata, C., and Van Dyk, J. (2003): Dosimetric considerations for patients with HIP

prostheses undergoing pelvic irradiation. Report of the AAPM Radiation Therapy Committee Task Group 63. *Med Phys* **30**, 1162-82.

Ruchala, K. J., Olivera, G. H., Kapatoes, J. M., Schloesser, E. A., Reckwerdt, P. J., and Mackie, T. R. (2000): Megavoltage CT image reconstruction during tomotherapy treatments. *Phys. Med. Biol.* **45**, 3545-62.

Thomas, S. D., Mackenzie, M., Field, G. C., Syme, A. M., and Fallone, B. G. (2005): Patient specific treatment verifications for helical tomotherapy treatment plans. *Med. Phys.* **32**, 3793-3800.